

**POLITECNICO DI TORINO**

Department of Mechanical and Aerospace Engineering  
**Master of Science in Mechanical Engineering**

Master Degree Thesis

**Optimization of Inconel 718 Downskin  
Parameters for the Production of Metallic  
Parts Via Laser Powder Bed Fusion**



**Supervisors**

Prof. Federica Bondioli  
Prof. Abdollah Saboori

**Tutor**

Ing. Paolo Calefati  
Ing. John Stavridis

**Candidate**

Vittorio Viale

Academic Year 2019-2020

# Abstract

These days, Additive Manufacturing (AM) technologies are considered as advanced processes in which it is possible to produce complex shape components in a layer by layer manner. It is interesting to notice that in these technologies, it is reported that in the production of the parts with angles higher than  $45^\circ$ , no support is required. Whereas, below this angle, the presence of support that can counterbalance the recoating blade's force and dissipates heat is necessary. In fact, there is a risk of detachments causing piece failure at these angles and increasing heavy dross formation on the downskin surface (high roughness). However, through the optimization of some parameters, it is possible to decrease this angle's value. Therefore, the thesis topic was to find the optimized downskin parameters for IN718 alloy to improve the overhang surfaces' quality in inclined specimens.

The work started with in-depth bibliographic research on downskin parameters. The most critical parameters were found to be overhang angle, laser power, laser speed, hatch distance, and the number of layers processed with the downskin parameters. Based on the knowledge acquired, the parameters' optimization was performed in Prima Industrie SpA using a Print Sharp 250 machine. The experimental procedures consisted of three "design of experiments" (DoE) and a repeatability test for the first one.

The first DoE was made by a  $3^3$  factorial experiment for specimens inclined at  $30^\circ$ ,  $35^\circ$ , and  $40^\circ$ , modifying laser power, laser speed, and hatch distance. The roughness analysis on the downskin surface was used as a key performance indicator. As a result, the best eight sets of parameters (for angles at  $35^\circ$  and  $40^\circ$ ) with a downskin roughness lower than  $21 \mu m$  were found (literature value at  $45^\circ$  for Inconel 718 is  $19 \mu m$ ). To verify the accuracy of the results, a repeatability test was performed by printing and analyzing some specimens using the same parameters. The variability detected was always lower than 5%, confirming the consistency of the results. The second DoE aimed to evaluate the porosity using image analysis in which the specimens were cut, polished and subsequently analyzed using an optical microscope. The densities of the specimens were always higher than 99.2% for the best sets of parameters. For this reason, it is not expected a change in mechanical characteristics in the downskin region. Finally, the third DoE was performed to

evaluate the tensile properties of the specimens printed with the best set of downskin parameters (lowest roughness). The core parameters during the printing phase have not been modified, and so it is expected that the mechanical properties of the specimens did not change.

All in all, in this thesis, the most influencing downskin parameters and their best combination for IN718 samples are found and reported. The outcomes demonstrated that it is possible for the IN718 to print up to  $35^\circ$  without the need for supports, keeping high density, and roughness lower than  $18 \mu m$ . This result allows a decrease in time and costs since support structures are no more needed. Furthermore, are now possible new design optimizations for the IN718, such as new lattice structures, applications with design constraints (rotor with angles lower than  $40^\circ$ ), and internal features (where supports removal is impracticable).

**Keywords:** *Additive Manufacturing, Laser Powder Bed Fusion, Downskin Parameters, Overhang*

# Acknowledgements

Before starting the thesis, I will spend a few words for the people who helped me in the thesis development.

I would like to express my sincere gratitude to my supervisors: Professor Federica Bondioli and Professor Abdollah Saboori of the Politecnico di Torino. Your support and guidance are invaluable to me.

I am incredibly grateful to my tutors and friends Paolo Calefati, John Stavridis, and Guido Barale. Your technical expertise and passion gave me an invaluable insight into the world of additive manufacturing.

Thanks should also go to all the team of Prima Additive. Everyone never wavered in their support during my work there.

My success during these years would not have been possible without my family's support and nurturing, my parents Mariolina and Oscar, my sister Maddalena, and my grandparents Eulalia, Mario, Luisa, and Franco. You are my strength in times of discouragement and those I always share with my times of joy.

Special mention to my girlfriend Silvia, the person with which I spent more time. Thank you for your continuous support, your profound belief in my abilities, and your constructive criticism.

Finally, I want to extend my sincere thanks to my friends that accompanied me during the last years. Especially to Giuseppe, my traveling companion in study and life, with whom I shared good and bad experiences along the way.

Thank you!

# Contents

|   |    |
|---|----|
| <b>Abstract</b>                                       | 2  |
| <b>List of Figures</b>                                | 7  |
| <b>List of Tables</b>                                 | 11 |
| <b>Acronyms</b>                                       | 12 |
| <b>1 Introduction on Additive Manufacturing</b>       | 15 |
| 1.1 Brief history of Additive Manufacturing . . . . . | 18 |
| 1.2 Process sequence . . . . .                        | 19 |
| 1.2.1 Conceptualization of CAD model . . . . .        | 19 |
| 1.2.2 Format . . . . .                                | 20 |
| 1.2.3 Supports generation . . . . .                   | 21 |
| 1.2.4 Slicing and part orientation . . . . .          | 22 |
| 1.2.5 Machine Setup . . . . .                         | 23 |
| 1.2.6 Build removal . . . . .                         | 24 |
| 1.2.7 Post processes and finishing . . . . .          | 24 |
| 1.3 Advantages and disadvantages of AM . . . . .      | 25 |
| 1.3.1 Advantages . . . . .                            | 25 |
| 1.3.2 Disadvantages . . . . .                         | 26 |
| 1.4 Process classification . . . . .                  | 27 |
| 1.5 Metal AM . . . . .                                | 29 |
| 1.5.1 Powder Bed Fusion . . . . .                     | 29 |
| 1.5.2 Directed Energy Deposition . . . . .            | 33 |
| 1.6 Design for metal AM . . . . .                     | 34 |
| 1.6.1 Parameters . . . . .                            | 40 |
| <b>2 Downskin limitations and potentials</b>          | 43 |
| 2.1 Downskin . . . . .                                | 43 |
| 2.2 State of the art on downskin parameters . . . . . | 47 |
| 2.2.1 Overhang angle . . . . .                        | 48 |

|          |  |            |
|----------|--|------------|
| 2.2.2    | Power, speed and vector length . . . . .     | 49         |
| 2.2.3    | Hatching distance . . . . .                  | 52         |
| 2.2.4    | Scanning strategy and aspect ratio . . . . . | 55         |
| 2.2.5    | Number of layers and pre-sintering . . . . . | 57         |
| <b>3</b> | <b>Material and machine</b>                  | <b>63</b>  |
| 3.1      | Machine . . . . .                            | 63         |
| 3.2      | Superalloys and Inconel 718 . . . . .        | 65         |
| 3.2.1    | Inconel 718 . . . . .                        | 68         |
| <b>4</b> | <b>Experimental Procedure</b>                | <b>71</b>  |
| 4.1      | DoE 1-Roughness evaluation . . . . .         | 71         |
| 4.2      | Repeatability test . . . . .                 | 75         |
| 4.3      | DoE 2-Porosity analysis . . . . .            | 76         |
| 4.4      | DoE 3-Mechanical characteristics . . . . .   | 78         |
| <b>5</b> | <b>Results and discussion</b>                | <b>81</b>  |
| 5.1      | DoE 1-Roughness evaluation . . . . .         | 81         |
| 5.2      | Repeatability . . . . .                      | 86         |
| 5.3      | DoE 2-Porosity . . . . .                     | 87         |
| 5.4      | DoE 3-Mechanical characteristics . . . . .   | 90         |
| <b>6</b> | <b>Conclusion</b>                            | <b>91</b>  |
| 6.1      | Results and highlights . . . . .             | 91         |
| 6.2      | Application development . . . . .            | 92         |
| 6.3      | Future works . . . . .                       | 93         |
|          | <b>Bibliography</b>                          | <b>95</b>  |
| <b>A</b> | <b>Print Sharp 250</b>                       | <b>101</b> |
| <b>B</b> | <b>Porosity analysis images</b>              | <b>103</b> |

# List of Figures

|      |  |    |
|------|--|----|
| 1.1  | Additive manufacturing and subtracting manufacturing [1] . . . . .   | 16 |
| 1.2  | Problem related to CNC production [20] . . . . .   | 16 |
| 1.3  | Forecast growth for metal AM [20] . . . . .  | 17 |
| 1.4  | Additive manufacturing process [1] . . . . .   | 19 |
| 1.5  | Transformation from CAD model to *STL file format [1] . . . . .  | 20 |
| 1.6  | Typical support geometries for metal powder bed fusion AM [66] . .   | 22 |
| 1.7  | Slicing: (a) Stair stepping problem depending on part orientation;<br>(b) Comparison between direct and adaptive slicing [1] . . . . .   | 23 |
| 1.8  | Heat treating processes [66]: (a) optimal process for a piece of Inconel<br>625; (b)optimal process for a piece of Inconel 718 . . . . .   | 25 |
| 1.9  | Classification of AM processes [3] . . . . .   | 28 |
| 1.10 | Classification laser processes [24] . . . . .  | 30 |
| 1.11 | Schematic representation of the SLM process [22] . . . . .   | 31 |
| 1.12 | Representation of the laser creating the melt pool [41] . . . . .  | 32 |
| 1.13 | Representation of the laser creating the melt pool [41] . . . . .  | 32 |
| 1.14 | Directed Energy Deposition [1]: (a) Electron beam heat source with<br>wire feeder; (b) Laser heat source with concentric nozzle to spread<br>powder . . . . .  | 34 |
| 1.15 | Powder spread using a blade for different layer thicknesses [66] . . .   | 35 |
| 1.16 | Effects of the Plateau-Rayleigh instability on a single track [33] . .   | 36 |
| 1.17 | Marangoni convection in the melting pool, the flow motion depends<br>on the temperature-surface tension gradient [42]: (a) Negative temperature-<br>surface tension gradient; (b) Positive temperature-surface tension<br>gradient . . . . . | 37 |
| 1.18 | Thermal history of two different scanning strategies in which change<br>the vector length [66] . . . . .   | 38 |
| 1.19 | Relationship between thermal gradient and the scanning vector length<br>[66] . . . . .   | 39 |
| 1.20 | Typical process map for laser melting process. The material is a<br>$Fe - Ni - Cu - Fe_3P$ alloy [35] . . . . .  | 40 |

|      |   |    |
|------|---|----|
| 2.1  | Example of overhanging surfaces [11]: (a) downward sloping face, (b) and (c) downward facing surfaces and (d) downward sloping faces  | 44 |
| 2.2  | The skin angle is the angle that indicates the region in a layer for which are applied the downskin parameters . . . . .  | 45 |
| 2.3  | Dross formation in a downward facing surface [11] . . . . .   | 45 |
| 2.4  | Warping effects:(a) in a downward sloping face [11];(b)Accumulation of warping effect[58] . . . . .   | 46 |
| 2.5  | Overhanging surfaces in a horizontal hole [30] . . . . .  | 46 |
| 2.6  | Parameters that affect quality of an overhanging surface by Wang [58]   | 47 |
| 2.7  | Specimen used in the generalized method [8] . . . . .   | 48 |
| 2.8  | Slicing model of a typical curved surface [58] . . . . .  | 48 |
| 2.9  | Relationship between critical inclined angle and scanning speed at different laser power (scanning space 80 $\mu\text{m}$ and layer thickness 35 $\mu\text{m}$ ). a) P=120 W, b) P=150 W, c) P=180 W [58] . . . . . | 51 |
| 2.10 | Fabricating effect comparison for supported surfaces [58] . . . . .   | 52 |
| 2.11 | Detachment between support and part (left), detachments of the support from the building platform (center), breaking of the support (right) in manufacturing for Inconel 718 [13] . . . . .                         | 53 |
| 2.12 | (a) Interface between support structure and downskin layers; (b) support structure of block type [13] . . . . .   | 54 |
| 2.13 | Experiment: (a) Specimen used, the aspect ratio is a:5, with a= 5, 3.5, 2.5; (b) Linear scan strategy; (c) Alternate scan strategy . . .  | 55 |
| 2.14 | Specimens obtained with different aspect ratios(above) and SEM images(below) . . . . .  | 56 |
| 2.15 | Experiment: (a) Linear scanning strategy; (b) Alternate scanning strategy . . . . .   | 57 |
| 2.16 | Temperature distribution and melt pools [30]: (a) Downskin parameters P=360 W, v=1000 mm/s; (b) Core parameters P=370 W, v=1300 mm/s . . . . .  | 58 |
| 2.17 | Melt pool depth for different parameters. The upper line represents the values obtained for the powder supported layers, while the bottom line identifies the solid supported layers [30] . . . . .                 | 59 |
| 2.18 | SEM images for some specimens in table 2.2: (a) specimen 1 ; (b) specimen 3;(c) specimen 6 . . . . .  | 59 |
| 2.19 | SEM images for some specimens in table 2.3: (a) specimen 1; (b) specimen 2; (c) specimen 3;(d) specimen 4; (e) specimen 5;(f) specimen 6 . . . . .  | 60 |
| 2.20 | Temperature distribution at: (a)P=65 W and v=1000m/s; (b) P=150 W and v=1000mm/s . . . . .  | 61 |
| 2.21 | Temperature distribution for the 4th layer printed with core parameters (360 W, 1000 mm/s) after 3 parameters done using downskin parameters (65 W, 1000 mm/s). . . . .   | 61 |

|      |   |    |
|------|---|----|
| 3.1  | Print Sharp 250 pictures: (a)External picture; (b) Inside view. . . .   | 63 |
| 3.2  | Description of the optical systems used in the Print Sharp 250 . . . .  | 65 |
| 3.3  | Mechanical characteristics and downskin roughness for a piece built by General Electric Additive Manufacturing [2] . . . . .  | 69 |
| 3.4  | Downskin roughness values for different angles at severals levels of power and speed [17] . . . . .   | 70 |
| 4.1  | Representations of the specimens used for the experiments: (a) drawn specimen in SolidWorks; (b) real printed specimen . . . . .  | 72 |
| 4.2  | EPHatch software interface and example: (a) EPHatch software interface with standard parameters; (b) graphic representation of the change in the skin angle. . . . .  | 72 |
| 4.3  | Roughness tester used in Prima Industrie SpA . . . . .  | 74 |
| 4.4  | Operations during DoE 1: (a) print phase for the specimens; (b) printed specimens attached to the plate . . . . .   | 75 |
| 4.5  | Cutting machine used in Prima Industrie SpA . . . . .   | 76 |
| 4.6  | Machine used to polish specimens at Politecnico di Torino: (a) Remet mounting press to put together more specimens, in this way was easier to polish them all together and increase the productivity; (b) polishing machine to obtain mirror polished surfaces for the specimens. . . . . | 77 |
| 4.7  | Specimens polished: (a) conditions of the specimens before the polishing operation; (b) mirror polished specimens, ready to be analyzed with the optical microscope . . . . .   | 78 |
| 4.8  | Analysis of the porosity: (a) optical microscope used in the laboratory; (b) software used for the analysis of the porosity. . . . .  | 79 |
| 4.9  | Standardized flat shape bar for the tensile stress test . . . . .   | 79 |
| 4.10 | Zwich-Roell BT1-FR100 used in Alessandria detachment of Politecnico di Torino . . . . .   | 80 |
| 5.1  | Dependence of roughness on the volumetric energy density for the specimens at 40°. The two lines represent the linear average of the measurements. . . . .  | 83 |
| 5.2  | Dependence of roughness on the volumetric energy density for the specimens at 35°. The two lines represent the linear average of the measurements. . . . .  | 83 |
| 5.3  | Dependence of the roughness with respect to the hatch distance used for the specimens inclined (a) at 40°; (b) at 35° . . . . .   | 84 |
| 5.4  | Dependence of the roughness with respect to the laser speed in the downskin region used for the specimens inclined (a) at 40°; (b) at 35° . . . . .   | 84 |
| 5.5  | Dependence of the roughness with respect to the power speed in the downskin region used for the specimens inclined (a) at 40°; (b) at 35° . . . . .   | 85 |
| 5.6  | Roughness variability obtained in the repeatability test for specimens inclined at (a) 40°; (b) 35° . . . . .   | 86 |

|      |  |     |
|------|--|-----|
| 5.7  | Dependence of the porosity with respect to the volumetric energy density used in the downskin region for the inclined specimens (a) at 40°; (b) at 35° . . . . . | 88  |
| 5.8  | Maximum equivalent diameter for each specimen . . . . .  | 88  |
| 5.9  | Optical microscope images, porosity analysis for the specimens (a) 4 inclined at 35°; (b) 6 inclined at 35° . . . . .  | 89  |
| B.1  | Optical microscope analysis images for the specimen 1 inclined at 40° in six different points of the downskin region. . . . .                                    | 103 |
| B.2  | Optical microscope analysis images for the specimen 2 inclined at 40° in six different points of the downskin region. . . . .                                    | 104 |
| B.3  | Optical microscope analysis images for the specimen 4 inclined at 40° in six different points of the downskin region. . . . .                                    | 104 |
| B.4  | Optical microscope analysis images for the specimen 6 inclined at 40° in six different points of the downskin region. . . . .                                    | 105 |
| B.5  | Optical microscope analysis images for the specimen 11 inclined at 40° in six different points of the downskin region. . . . .                                   | 105 |
| B.6  | Optical microscope analysis images for the specimen 12 inclined at 40° in six different points of the downskin region. . . . .                                   | 106 |
| B.7  | Optical microscope analysis images for the specimen 15 inclined at 40° in six different points of the downskin region. . . . .                                   | 106 |
| B.8  | Optical microscope analysis images for the specimen 20 inclined at 40° in six different points of the downskin region. . . . .                                   | 107 |
| B.9  | Optical microscope analysis images for the specimen 1 inclined at 35° in six different points of the downskin region. . . . .                                    | 107 |
| B.10 | Optical microscope analysis images for the specimen 2 inclined at 35° in six different points of the downskin region. . . . .                                    | 108 |
| B.11 | Optical microscope analysis images for the specimen 4 inclined at 35° in six different points of the downskin region. . . . .                                    | 108 |
| B.12 | Optical microscope analysis images for the specimen 6 inclined at 35° in six different points of the downskin region. . . . .                                    | 109 |
| B.13 | Optical microscope analysis images for the specimen 11 inclined at 35° in six different points of the downskin region. . . . .                                   | 109 |
| B.14 | Optical microscope analysis images for the specimen 12 inclined at 35° in six different points of the downskin region. . . . .                                   | 110 |
| B.15 | Optical microscope analysis images for the specimen 15 inclined at 35° in six different points of the downskin region. . . . .                                   | 110 |
| B.16 | Optical microscope analysis images for the specimen 20 inclined at 35° in six different points of the downskin region. . . . .                                   | 111 |

# List of Tables

|     |   |     |
|-----|---|-----|
| 1.1 | Benchmarks mechanical properties of AM metals specimens produced with SLM process . . . . .                               | 39  |
| 2.1 | Process parameters, volume energy density and linear energy density for down-skin and support . . . . .                   | 53  |
| 2.2 | Parameters used in the first experiment [30] . . . . .  | 58  |
| 2.3 | Parameters used in the second experiment [30] . . . . .   | 60  |
| 3.1 | Powder composition: nominal weight percentage of the elements present in the powder [23] . . . . .                        | 68  |
| 3.2 | Powder dimensions and characteristics [23] . . . . .  | 68  |
| 4.1 | DoE 1: Parameters used to print specimens. The 27 sets of parameters are used for each angle (30°, 35°, and 40°). . . . . | 73  |
| 4.2 | Standardized dimensions (ASTM E8) for the flat shaped bar represented in figure 4.9 . . . . .                             | 80  |
| 5.1 | Downskin roughness of the specimens printed in the DoE 1 . . . . .  | 82  |
| 5.2 | Repeatability test and average downskin roughness . . . . .   | 86  |
| 5.3 | Results from the porosity analysis of the specimens . . . . .   | 87  |
| A.1 | Print Sharp 250 and process specifications [63] . . . . .   | 102 |

# Acronyms

|                 |  |
|-----------------|--|
| <b>AM</b>       | Additive Manufacturing                     |
| <b>AMF</b>      | Additive Manufacturing File                |
| <b>ASTM</b>     | American Society for Testing and Materials |
| <b>BJ</b>       | Binder Jetting                             |
| <b>CAD</b>      | Computer Aided Design                      |
| <b>CNC</b>      | Computer Numerical Control                 |
| <b>CLI</b>      | Command Line Interface                     |
| <b>DED</b>      | Directed Energy Deposition                 |
| <b>DED-L</b>    | Directed Energy Deposition Laser           |
| <b>DED-EB</b>   | Directed Energy Deposition Electron Beam   |
| <b>DoD</b>      | Drop on Demand                             |
| <b>DoE</b>      | Design of Experiment                       |
| <b>DMD</b>      | Directed Metal Deposition                  |
| <b>DMLS</b>     | Directed Metal Laser Sintering             |
| <b>EBM</b>      | Electron Beam Melting                      |
| <b>EBF3</b>     | Electron Beam Free Form Fabrication        |
| <b>EDM</b>      | Electric Discharge Machine                 |
| <b>FDM</b>      | Fusion Deposition Modelling                |
| <b>GD and T</b> | Geometric Dimensional and Tolerances       |
| <b>HIP</b>      | Hot Isostatic Pressure                     |
| <b>KPI</b>      | Key Performance Indicator                  |

**ISO** International Organisation for Standardisation  
**LM** Laser Melting  
**LMD** Laser Metal Deposition  
**LBM** Laser Beam Melting  
**LENS** Laser Engineered Net Shaping  
**LED** Linear Energy Density  
**LS** Laser Sintering  
**LPBF** Laser Powder Bed Fusion  
**PA-DED** Plasma arc Directed Energy Deposition  
**PBF** Powder Bed Fusion  
**PLC** Program Logic Control  
**RP** Rapid Prototyping  
**SED** Superficial Energy Density  
**SEM** Scanning Electron Microscopy  
**SLA** Stereolithography  
**SLM** Selective Laser Melting  
**STL** Standard Triangulation Language  
**SLS** Selective Laser Sintering  
**YS** Yield Strength  
**US** Ultrasonic Consolidation  
**UTS** Ultimate Tensile Strength  
**UV** Ultraviolet  
**VED** Volume Energy Density



# Chapter 1

## Introduction on Additive Manufacturing

Metal additive manufacturing is a group of technologies that are rapidly increasing their importance nowadays and aim to become important in the strategic process of a firm. The key concept is the additive process, opposite to the most common subtracting one (i.e. machining), a revolutionary kind of manufacturing. The final piece will be made by adding material in layers, causing a reduction in terms of waste produced. The differences between the two processes are represented in figure 1.1. It should also be noted that not all the processes are just additive; there are stages in which it is possible to use subtracting processes [20]. Industries are benefiting from this process thanks to the shortening of the design-to-manufacture time. AM can reduce the number of operations needed to produce an end-usable part and transform several processes with a single step process plus a finishing step. Indeed for ASTM standard, "Removal of the support structure and cleaning may be necessary; however, in this context are not considered as a separate process step". [6]).

It is possible to compare the production of a batch of pieces done by AM and by a CNC (Computer Numerical Control) machine. Using a CNC machine it can be needed to position the piece within one machine or in more than one. In AM, a piece can be produced just in a few hours, while a high-quality finishing may take a few days. However, it is possible to produce more pieces in a single AM build (limitations given by the maximum size of the piece and size of the production plate), doing the same with a CNC machine can take weeks. [20].

The piece's complexity is a fundamental aspect for AM: since the process directly obtains the complex shapes, the cost is not dependent on the difficulty, and the gain using AM increases with the complexity. Moreover, there are pieces that were

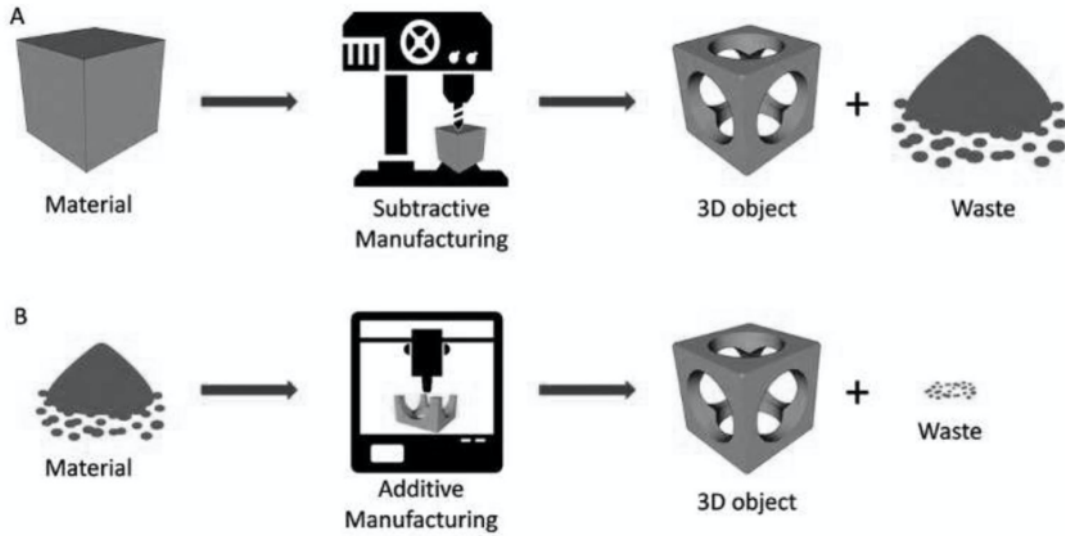


Figure 1.1: Additive manufacturing and subtracting manufacturing [1]

impossible to be created with CNC machines, with AM part of the constraints are avoided, such as lattice structures, undercuts, and interior features (figure 1.2).

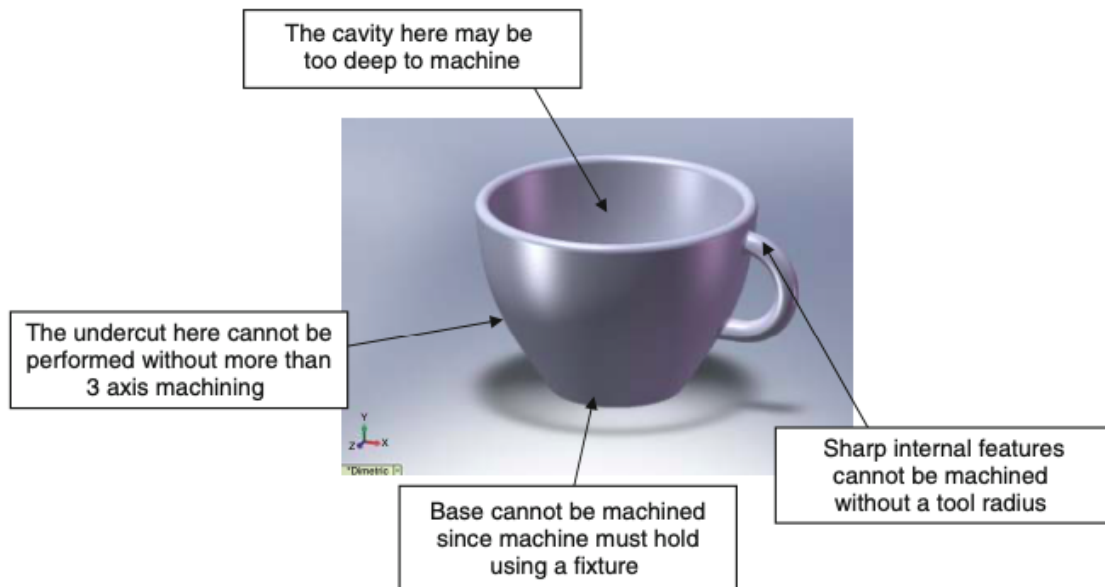


Figure 1.2: Problem related to CNC production [20]

Although additive manufacturing will not replace conventional production methods, can acquire importance in different niche areas such as aerospace (turbines

that must have optimal thermo-mechanical characteristics), medical and dental fields (where the weight and the customization of a single piece is a key factor), automotive pieces and jewelry. One of the new relevance aspect of AM technology is the possibility to produce lattice structures: this possibility allows to reduce the weight and create new structures. In figure 1.3 it is represented the forecast growth for metal AM.



Figure 1.3: Forecast growth for metal AM [20]

## 1.1 Brief history of Additive Manufacturing

The concept of the layer by layer fabrication was already used in Egypt in 2700 B.C. for pyramids. The historical development that brings to the production of end-usable parts (additive manufacturing) started around forty years ago (1980) with the "rapid prototyping". This process could be performed only for plastic materials for conceptual, functional, and technical prototypes. The development of different prototypes represents the evolution of rapid prototyping [1]:

1. conceptual prototype: aim to control the geometry of the part to make assembly tests. It can be used for any material and any fabrication techniques;
2. functional prototype: used for the evaluation of performances through functional tests and optimization of the product for its function. There are no limitations for the fabrication techniques, but the material used should be similar to the final one;
3. technical prototype: used for the evaluation of product performances, processes and the optimization of the fabrication techniques. The material used and the fabrications technique should be both similar to the final ones;
4. pre-series prototype: to do a final evaluation of the product. Here both the material and the fabrication technique must be the final ones.

After twenty years (2000), the technical development brought to new system developments: "rapid tooling", "rapid casting", and "rapid manufacturing". These terms are used respectively for the production of tools, devices for casting applications, and directly the end-usable part (only in plastic materials). Nowadays, the most common terms of "additive manufacturing" or "layered manufacturing" identify a process that can produce end-usable parts also using metals. It is interesting to underline the conceptual difference between additive manufacturing and 3D printing. The first is a term used for production technologies and supply chains. In contrast, the second one is associated with people printing at home or in the community (a cheaper solution that cannot fulfill industrial requirements for pieces). Additive manufacturing is a layer-based automated fabrication process for making 3D physical objects directly from 3D-CAD data (from an \*.stl file) without using part-depending tools.

## 1.2 Process sequence

The process sequence for AM pieces production is:

- conceptualization and CAD model creation;
- conversion into an STL file format;
- generation of the supports and orientation of the piece;
- slicing;
- machine setup;
- printing phase;
- part removal;
- post processing;
- application.

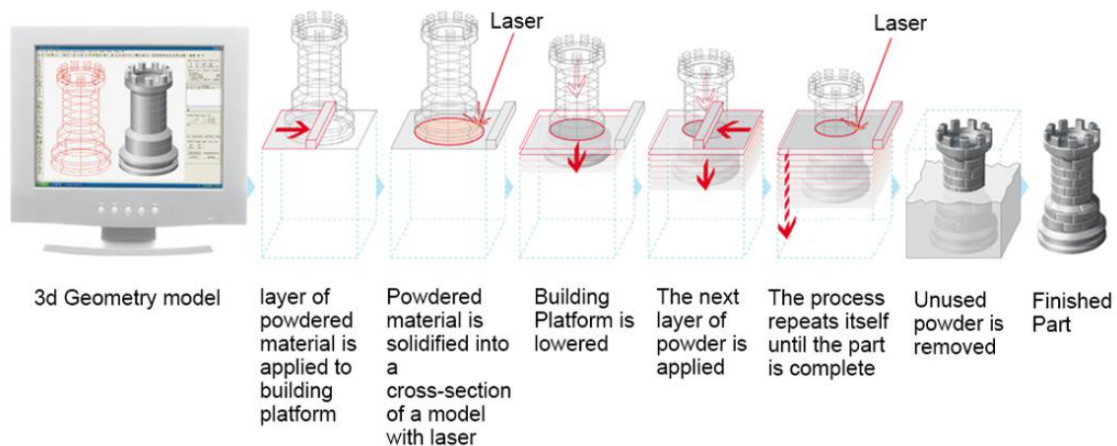


Figure 1.4: Additive manufacturing process [1]

### 1.2.1 Conceptualization of CAD model

The conceptualization is a complex part of the process, considering an industry point of view, it is fundamental consider that the knowledge needed to design an AM piece is different from the one to design pieces with subtractive processes. Different points must be highlighted: some constraints are removed in AM pieces (undercuts and internal features) and others should be considered, for these reasons AM specialists are needed as designers to design computer-aided design (CAD) models. Moreover, specifically speaking for metal powder technologies, the design creation becomes iterative. Indeed, some aspects are difficult to be predicted with

precision: the influence of build orientation, of the thermal history of the piece (causing thermal stresses), and specific characteristics of the metal powder used [66].

### 1.2.2 Format

The STL (Standard Triangle Language) file format is the standard format used in AM. It has been developed by "3D Systems" in the USA, who was the first company to commercialize "stereolithography technology" [41]. This language describes the piece's surfaces using triangles. Each one is done by three points and a normal facet vector indicating the triangle's outward side using a three-dimensional Cartesian coordinate system. Depending on the resolution needed, the triangles can vary their dimensions to follow the piece's profile properly. Several problems are linked to the conversion from CAD model to STL file: gaps between cells, inverted normal vectors, intersection of triangles, and internal walls. Before the building phase, the final step is to correct all the errors generated in the passage from CAD to STL file. There are groups of software that automatically carry out this phase: for the powder bed technology, an example is Materialise Magics. This software corrects the STL file, but it also has other functions like creating the supports and preparing the build file (slicing).

In the STL file, there are no pieces of information about color, texture, or other attributes usually used in CAD models, eliminated in the translation of the format. For these reasons, nowadays, the ASTM/ISO format is the Additive Manufacturing File (AMF) [66]. However, the most common format is always the STL one.



Figure 1.5: Transformation from CAD model to \*STL file format [1]

### 1.2.3 Supports generation

Support generation is not easy, each AM technique has his characteristics, and the support has different relevance depending on it. Generally speaking, the support is necessary for some structures, but it is usually undesired in a contradictory way: it is a waste of material and time. Moreover, the removal of the support structure is not trivial in metal AM, where, for example, the support is made of the same material as the piece, it can sometimes be removed just using an electric wire cutter. While in plastic pieces, some machines allow using the support of different materials. For example, if it is made of a material that can be easily dissolved with chemical substances, it is not a problem for the removal.

In vat photopolymerization, the support is used to counter the shrinkage forces generated by the solidification and increase the piece's quality. In material extrusion, it is used to act against the residual stresses and sustain the piece against gravity. In laser powder bed fusion processes the supports have different aims. It is wrong to think that these are needed to hold surfaces that are "unsupported": there are other two fundamental objectives that are:

1. dissipate heat: the heat conduction of a powder is, in general, one hundred times lower than the one of the bulk material [59], so there is dross formation and a consequent increase of roughness for downward facing surfaces;
2. avoid warpage: during the solidification of a line vector, there is the creation of forces inside the solidified material, the first part of the vector has compressing forces. In contrast, the final part has tensile forces. The supports have the aim to counterbalance these forces and avoid detachment.

A common use of the supports is for the overhanging surfaces; an inclined surface usually should be supported above a certain angle: the critical angle depends on the specific material used and the dimension of the overhang, but it is considered 45° [51].

Usually, in the software used for AM, there are specific algorithms that evaluate the unsupported surfaces and decide where the support is needed. There are different types of geometries (figure1.6) and depending on the attachment strength needed can vary also the contact between support and piece, such as points (weaker), lines (average) or areas (stronger). The stronger the support structure, the more it is challenging the removal.

Part orientation is essential to minimize the support required, but sometimes the orientation that allows to minimize it will increase the time needed to produce the piece. It is more important to consider that the surfaces connected with the support will suffer lower quality due to its removal. It is essential to avoid using the support in the piece's functional surfaces or features (internal channels and holes).

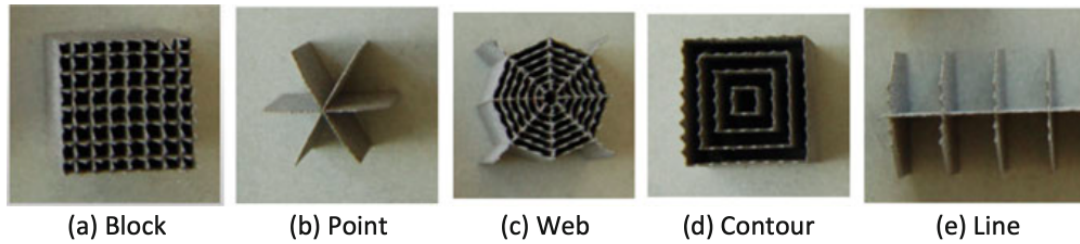


Figure 1.6: Typical support geometries for metal powder bed fusion AM [66]

For these reasons, sometimes, the best orientation for particular geometries is not a vertical or horizontal piece, but an inclined one.

Moreover, specifically speaking for metal AM, given the difference of the piece parameters and support ones, the overlapped region between them is more affected by microstructural defects. In order to decrease the negative effect of the supports, it is becoming common to use cellular structures: structures characterized by geometries with specific porosity generated by the software imposing a relative density. This kind of structure is more comfortable to be removed and need smaller production time, but also the effectiveness and the strength of them are decreased with respect to block support.

### 1.2.4 Slicing and part orientation

The model should be adequately oriented not only to minimize support on functional parts, but also to reduce problems related to the slicing. It is crucial to notice that the part orientation is done by considering both the minimization of the support structure and the slicing problems. Here, the problems are divided into two paragraphs.

The slicing is the subdivision of the part in layers: parallel planes with the normal perpendicular to the x-y building plane. Ideally, in powder bed fusion systems, the layer thickness should be slightly bigger than the powder's mean diameter. In this way, it is possible to maximize the melting of the powder (direct impact of the laser on the single particles to be melted).

The orientation and the thickness of the layers are important to reduce the stair-stepping effect: when an oblique surface is created, it is possible to see a sort of "stairs" since the piece is made of layers (figure1.7(a)). This effect is unavoidable; however, it is possible to minimize the problem by decreasing the layer thickness and changing the piece's orientation.

When the thickness of the layers is decreased, the drawback is an increase in production time. In order to find a trade-off between these two concepts, it is possible

to use an "adaptive slicing system". The thickness of the layers can decrease when printing an oblique surface or a functional portion of the part, while it can increase when the piece is not subjected to the stair-stepping effect. The problem is that changing the layers' thickness will also change the heat transfer that occurs in each layer: it is important to consider that and study the mechanical properties and the possible inhomogeneity in the piece.

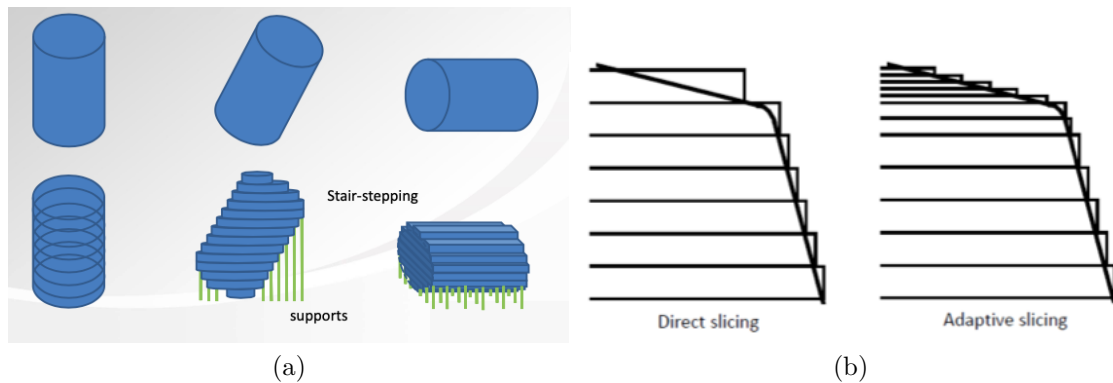


Figure 1.7: Slicing: (a) Stair stepping problem depending on part orientation; (b) Comparison between direct and adaptive slicing [1]

### 1.2.5 Machine Setup

The machine setup is the last step before the building phase, and it is made by the hardware setup and the process control. The hardware setup consists of a check about the build settings and some process controls, plus the building chambers' preparations: cleaning from the powder of the previous piece produced and the loading of new powder. The process control is the sequence of operations that allows choosing the process parameters and interrupting the printing phase if needed. In this phase, the build process parameters are determined: the recoater blade motion, the ventilation processes, and the gas injections. Material and parameters are also selected for the part and, eventually, the support: laser power, laser speed, spot size, and hatch distance. It is essential to know that in the building phase inert gases (nitrogen or argon) are used to maintain low oxygen concentrations. These concentrations should be kept below 1-2%, and it is particularly important for reactive materials in powder bed processes for safety reasons.

During the building phase, there are also some feedback controls. For the melt pool, a diagnostic beam, coaxial to heat source, can monitor the size and radiations emitted from the melt pool. Another type of control can be used on the recoater blade. It is possible to take and analyze an optical image; by checking the reflectivity, it is possible to see if there is a full coating or not. If it is not done, the printing is stopped, and the powder layer is adjusted.

### **1.2.6 Build removal**

Depending on the process used, when the building process is finished, the piece can be removed immediately or require some time to cool the environment. The L-PBF technology allows to remove the piece immediately, while the electron beam one and the powder bed for polymers have the build platform pre-heated. The build removal consists of raising the platform and remove the unused powder. This powder can be mixed with a virgin one and be reused. The removal of the metal piece from the platform can need an electric wire or a cutting tool [66].

### **1.2.7 Post processes and finishing**

The final part of the process considers support removal and, eventually, some stages to improve the quality and mechanical properties of the printed pieces. After the support removal, an abrasive finishing can be done: for example, polishing, sandpapering, or application of coatings. Other applications are draining, rinsing, and heat-treating. The typologies of post-processes depend on the machine used. In the case of powder bed fusion, the minimum post-process required is the support removal from the piece. Depending on the support structure, it can be removed by hand or can need the use of electric wire (EDM) or CNC tools (in the latter, are also needed post processes to achieve a good finishing). However, since there is the creation of melt pools and quick cooling, there are necessary heat treatments (i.e. thermal annealing) to have a stress release or change the microstructure (reduce hardness). Some heat-treating processes are reported in figure 1.8. Another post-process used is the hot isostatic pressure (HIP): the piece undergoes a temperature higher than 50% of the melting point and a pressure higher than 100 MPa. It is used to reduce porosity (density higher than 95%) and change microstructure. [66]. It is also possible to apply finishing processes to improve the surface quality and aspect: permanent surface coloring, painting, plating, vacuum metallization, blasting, and polishing.

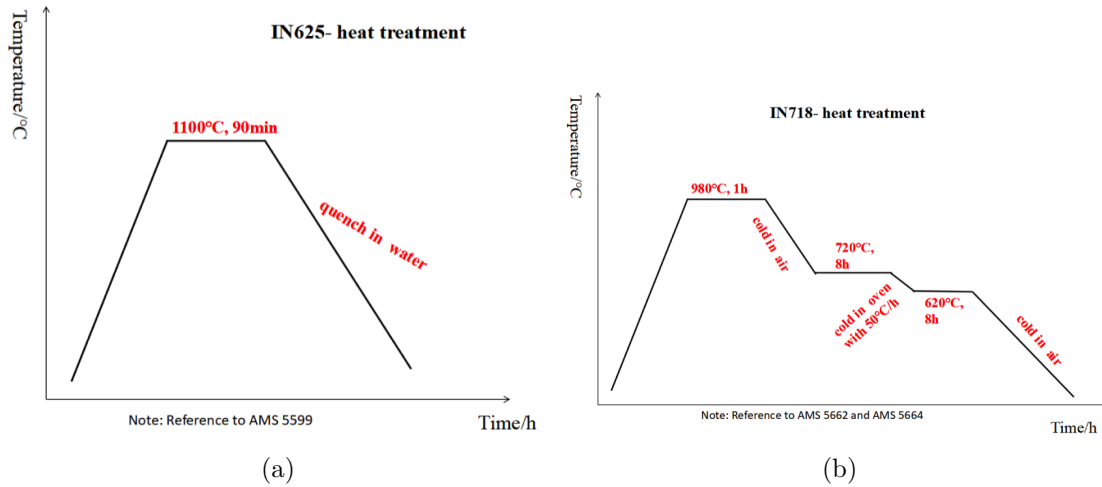


Figure 1.8: Heat treating processes [66]: (a) optimal process for a piece of Inconel 625; (b) optimal process for a piece of Inconel 718

## 1.3 Advantages and disadvantages of AM

### 1.3.1 Advantages

Advantages can be divided between product and process. Product advantages:

- design freedom: there are few geometrical limitations in AM. In metal AM limitations are caused by supports presence, while for plastic materials, theoretically there are zero limitations;
- lightweight structures: thanks to topology optimization, the material is deposited only where it is needed. There is the possibility to build a lattice structure in which it is feasible to decide the relative density;
- integrated design and assemblies: it is achievable to produce components with hinges and movable parts directly. This kind of use is easier in plastic AM, where the supports can be dissolved after the production;
- anatomical personalized: there are no costs to change the mold in the production or the needing of different machines. In AM, it is just needed to modify the initial CAD model, and it is possible to personalize the piece for a specific client. This concept is perfect for biomedical applications: the combination of lightweight structures, bio-compatibility of certain materials printed, and the possibility to personalize pieces allows to enter in the business sector;
- customization individualization: as for the anatomical customization, it is possible to fulfill requests and customize pieces for a client without impacting the process cost.

Process advantages:

- only one machine can create unlimited forms: since there are few limitations in AM, it is possible to create unlimited forms using just the AM machine. The pieces can be used just after the printing, avoiding a mold for the production and of tools for post-processing;
- undercut: since the pieces are produced layer by layer, it is possible to use undercuts in pieces design. The drawback is that it is not possible to apply finishing post-processing, since the undercuts are inside the piece;
- one manufacturing step: AM can reduce the number of operations needed to produce an end-usable part. It transforms several processes with a single step process plus an eventual finishing step;
- reduced operator intervention: during the fabrication, it is not required manual work, while it can be necessary for piece remotion by the building chamber and for supports removal;
- time and cost mainly related to size, not complexity: the cost for a piece in AM (without considering the "plant" cost of the machine) is the sum of the powder's cost and the cost of the production. The last one is subdivided into printing time and setup time (recoating and laser setup), so basically, the size of the piece strongly influence the cost. Simultaneously, the complexity, since the production is done layer by layer, does not affect the cost.

### **1.3.2 Disadvantages**

The drawbacks are also separated into the product one and the machine one. Product:

- overhangs: probably the biggest limitation in AM and the core part of the thesis. There is a reliable angle (angle defined between building surface and downward-facing surface), for which an overhang surface can be produced without supports. Below that angle, supports are usually needed: this will cause an increase in time of the production and costs and it adds a limitation for the topology optimization;
- finishing: often is needed a post-treatment for superficial finishing, increasing the cost of pieces production. It is problematic when it is required a finishing process in complex shapes parts or inner portion. In these situations it is required a change in process parameters in order to get the best finishing possible directly by increasing the time production;
- material cost and variety: since the powder is produced by atomization, its cost is quite higher with respect to the raw material's one. Since it is costly

to test a new powder, there is a limited number of them.

Machines:

- build rates: much research is going on to find an effective way to increase it, avoiding the drop in mechanical properties. For metal AM the speed is linked with the quality of the piece, and it becomes a limitation;
- building size: in particular for metal AM, machines have limited size (on average, the maximum dimension is a cube of edge 400mm). With plastic materials, usually, machines are bigger;

## 1.4 Process classification

The American Society for Testing and Materials International (ASTM International) has created a specific committee for developing standards for AM technologies: "Committee F42". From the ASTM F2792-12a-Standard Terminology for Additive Manufacturing Technologies [26], there are seven groups:

- Binder Jetting (BJ): liquid bonding agent selective deposited to join powder material. It can be used for metals, polymers, and ceramics;
- Directed Energy Deposition (DED): "nozzle mounted on a multi-axis arm, which deposits melted material onto the specified surface, where it solidifies" [53];
- Material Extrusion: the material is dispensed through a nozzle. It is the 3D printing machine that people can buy at home for a small investment. The materials used are always polymers, and the process name is "Fused Deposition Modelling" (FDM);
- Material Jetting (MJ): droplets of photopolymer selectively deposited.
  - Drop on Demand (DoD): high accuracy with the drawback of slowness requires an intermediate milling process.
  - Polyjet;
- Powder Bed Fusion (PBF): thermal energy selectively fuses regions of a powder bed. It is the most important manufacturing processing for metal materials. Materials used are metals, polymers, and ceramics.
  - Selective Laser Melting (SLM): the thermal energy is a laser that melts the powder creating melt pools;
  - Electron Beam Melting (EBM): The thermal energy is an electron beam
  - Selective Laser Sintering (SLS): it is used for polymers and ceramics.

- Sheet Lamination: sheets of material are bonded to form a piece. Nowadays, it is no longer used.
  - Ultrasonic Consolidation (UC): it is an additive-subtractive process, it combines an ultrasonic metal seam welding (using a rolling sonotrode) and a CNC milling. The material used is metal, and the quality level is limited;
  - Laminated Object Manufacture: for ceramic materials.
- Vat Photopolymerization: it is used a liquid photopolymer in a vat, which is accurately activated by an ultraviolet (UV) range of wavelengths;
  - Stereolithography (SLA): for photopolymers;
  - CeraFab, CeramPilot: for ceramic photopolymers;

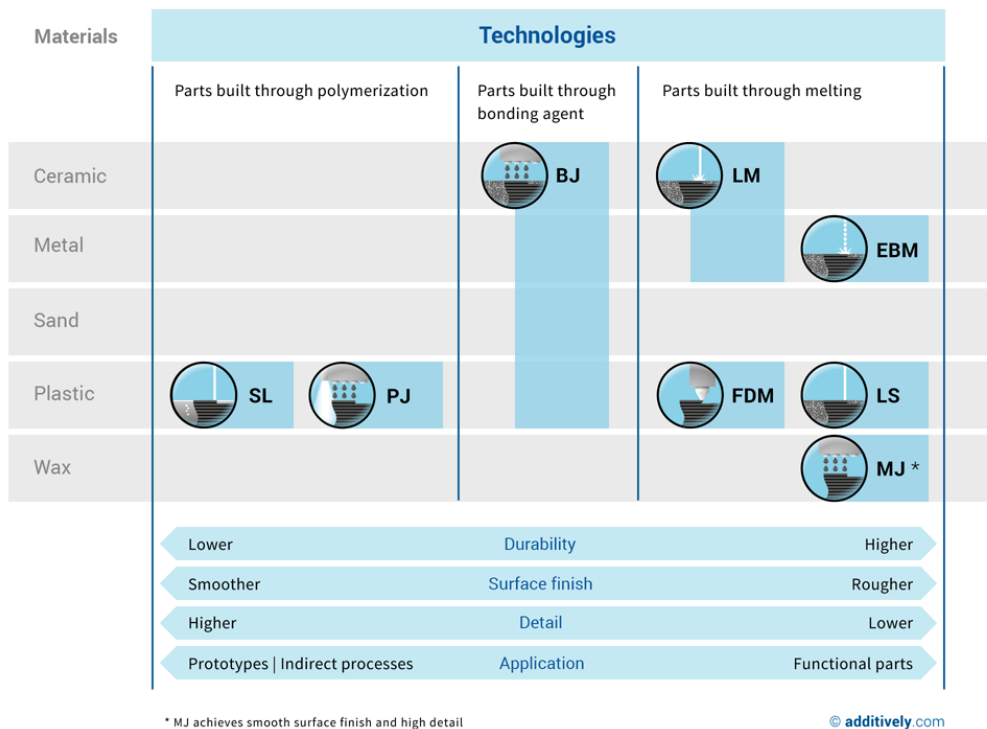


Figure 1.9: Classification of AM processes [3]

In figure 1.9 it is showed the classification of technologies summarized by "additively" [3]. It is possible to see how processes influence the characteristics of durability, surface finishing, details quality, and the functionality level of final pieces. It is important to notice that some acronyms are different from the ones of ASTM: Laser Melting (LM), Laser Sintering (LS), Stereolithography (SL), and Photopolymer Jetting (PJ).

## 1.5 Metal AM

The use of metals in additive manufacturing is becoming attractive in the last years. Thanks to the improvements in the machinery, lasers, and powders, it is possible to achieve high-quality pieces. In this section, the most common categories of machines used for metal AM are analyzed. The system characterization usually is made by the heat source used (laser or electron beam), the type of feedstock used (wire or powder), how the feedstock is delivered, and the dimension and quality of the piece produced. Powder bed fusion (PBF) is one category; for this one, the heat source can be a laser (L-PBF) or an electron beam (PBF-EB or EBM). The other important category is the directed energy deposition (DED), which can also have different heat sources: laser (DED-L), electron beam (DED-EB or EBF3, "Electron Beam Free Form Fabrication"), and plasma arc (PA-DED) [41].

### 1.5.1 Powder Bed Fusion

In the powder bed fusion, the system for which the high energy heat source scans following a prescribed direction to melt the powder and create the right shape is common. When the heat arrives at the powder surface, some of the energy is lost (reflected by the surface or radiated away as heat), while the absorbed one creates a molten pool. After the layer's scan, the powder bed will move downward for a distance equal to the layer thickness, and the recoating blade equally spread the powder on the bed. This sequence is repeated until the piece is completely created.

#### Laser Powder Bed Fusion

Several names are used to indicate the same process, apart from L-PBF: "direct metal laser sintering" (DMLS), "selective laser melting" (SLM), and "selective laser sintering" (SLS). The name direct metal laser sintering is used by the company EOS, which was the first company able to process metal materials. At the beginning of the development of technology, the process was just able to perform sintering. With respect to the laser sintering, the laser melting can achieve a fully dense component (99.9%) with mechanical properties similar to those of bulk material [24]. It can be used to produce parts in superalloys, such as Inconel or Hastelloy (nickel superalloys), with mechanical properties and microstructures comparable or superior to casting or forging processes [60]. In the last years, thanks to the development of better lasers (higher laser power and smaller spot size), the laser melting processes' mechanical properties and microstructural characteristics are better than the ones of laser sintering. Moreover, with the complete melting of the powder, there is the possibility to process materials unusable with the laser sintering. The pure materials, such as titanium, aluminum, and copper, cannot be used to produce good pieces

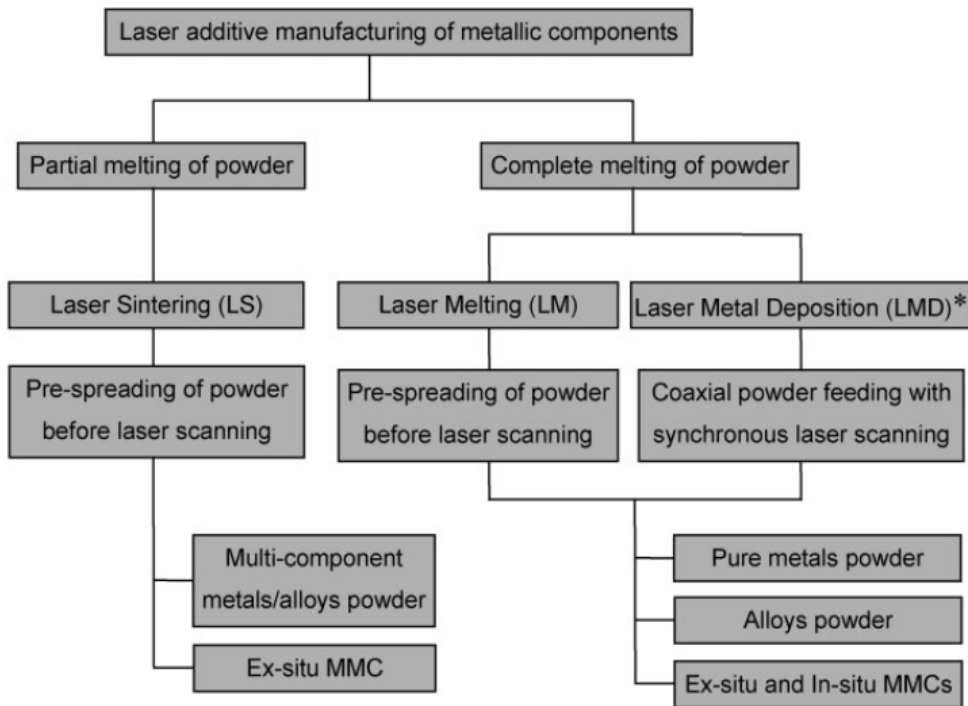


Figure 1.10: Classification laser processes [24]

in LS due to their high viscosity and the consequent balling phenomena (spheroidisation of the liquid melt pool due to melting instabilities/partial non-homogeneous melting) [52].

The schematic view of the process is represented in figure 1.11. For the L-PBF process, the heat source is a laser; there are different kinds of lasers, such as  $CO_2$ , fiber lasers, and disc lasers. Each laser is characterized by a wavelength that influences the creation of the melting pool. The fact that laser is guided by magnetically driven mirrors using galvanometers is one advantage of the SLM system. This method allows avoiding the movement of the laser head (that is needed in directed energy deposition machines), giving simplicity and precision to the process [41].

In laser melting processes, the high laser power combined with the thin layer of powder creates a melt pool that will quickly cool, causing a substantial shrinkage in the material and, consequently, the piece's stress [56]. This is responsible for distortions and possible delaminations of the layers; however, a good adhesion can counterbalance tensile forces with the previous layer or supports and optimize the process parameters. A representation of the laser melting the powder is reported in figure 1.12; it is interesting to notice that the thickness of the melted layer is smaller than the thickness of the powder layer. It is important to focus on the

fact that the melt pool's depth is bigger than the layer thickness, usually should be 3-4 times the thickness: to reach high density in the piece, it is required to penetrate in the previous layers. To reach high density, it is essential to fully melt the layer. The parameter that controls this factor is the hatching distance: the distance between the laser and adjacent vectors in a layer. The hatching distance regulates the overlap of melt pools: if two melt pools are too far, there can be un-melted powder between them, and it can cause the collapse of the piece or the generation of defects. In the figure 1.13, are represented the importance of melt pools control, to avoid un-melted powders.

One of the most significant limitations is related to this kind of machine's size: the maximum dimension for the pieces built by the machines commercially available size is currently limited to 400-500 mm. The other drawbacks for the SLM technologies are the presence of porosity, voids, and defects in the final piece, the slow deposition rate, the possible creation of distortion and cracking, and the cost of the powder material.

A good improvement has been reusing the not fused powder by mixing it with the virgin one. The mechanical properties of a piece produced with the mix of powders are slightly lower than those done with just virgin powder. The surface conditions of a piece produced by L-PBF are dependent on the parameters used, part orientation, and powder morphology. However, it may be used a post-process treatment to achieve specific dimensional tolerances. In order to increase surface quality, it is essential to minimize the use of support structure. For this reason, it is important to study the minimum angle for an overhang surface that can be printed without the need for supports.

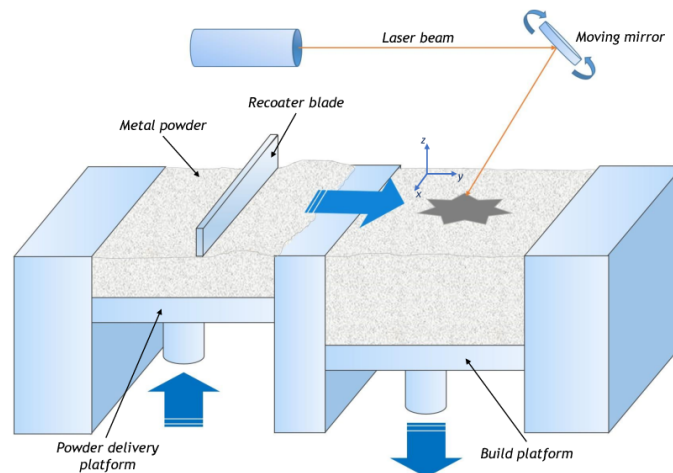


Figure 1.11: Schematic representation of the SLM process [22]

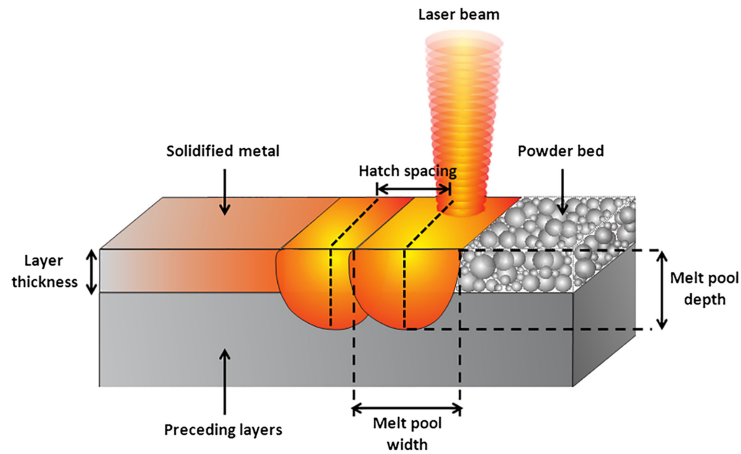


Figure 1.12: Representation of the laser creating the melt pool [41]

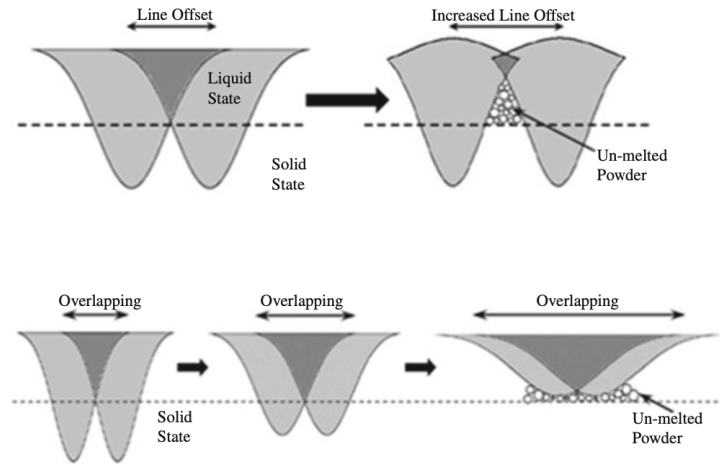


Figure 1.13: Representation of the laser creating the melt pool [41]

## Electron Beam Melting

The electron beam with respect to the laser has some advantages: a high energy density and beam power with a higher purity vacuum environment that allows the use of more reactive materials. ARCAM, a Sweden society, is the first producer that creates an EB-PBF machine. The electrons are emitted by a filament which is heated at temperatures higher than 2500°C, after the electrons are accelerated through the anode. Now the beam is controlled by the use of three lens before arriving in the vacuum chamber in which melt the powder. The first one is the astigmatism lens, to shape the electron beam in circular or oval shape. The focus lens is a magnetic field coil that focus the beam, after there is the deflection lens, another magnetic field that controls the deflection of the beam. Finally the electron

beam enters in the vacuum chamber and impacts the powder, here the kinetic energy is transformed into heat. It is important that there are no moving parts: the beam deflection is regulated just by the deflection coil.

With EBM technology it is possible to achieve high power (4 kW) with a narrow beam, it means also a high build temperature. The pieces can be built in refractory materials thanks to the high purity vacuum, that allows also to build parts with less impurities, giving higher strength properties to the material [1]. Usually it is also used the electron beam for a preheating of the powders (700°C), this allows to decrease the stresses in the final piece caused by high differences of temperatures. The preheating feature allows also to decrease support structure needs: the lightly sintered powder acts as support and it is easier to be removed at the end than a support structure. Thanks to the small focus beam spot size (100  $\mu m$ ) it is possible to achieve high quality of details. The chamber dimension has typical dimension of 350 x 380 mm, so the part size is also here a limitation. Another drawback of EBM systems is the slow cooling time, but also the high cost of the powders and the few materials options [41].

## 1.5.2 Directed Energy Deposition

The directed energy deposition technology is different from the powder bed processes: here the machine deposits the fused powder only where it is needed in a melt pool, created by the heat source, on the surface of the piece. Often this process is used for reparation of parts thanks to his adaptability: the machine is made of two parts, a heat source and a powder delivery nozzle. There are different types of DED machines (figure 1.14), the most common uses a laser heat source and a concentric powder nozzle around it (figure 1.14(b)). Another possibility is to have the heat source as an electron beam and use a wire feeder instead of powder (figure 1.14(a)). This kind of systems allows to release the powder in the melt pool and immediately melt it on specific points. The nozzle that controls the deposition process can be performed by multi-axis machines with a computer numerical control (CNC), in this way it is possible to reach any point with a good precision. However, since the nozzle has to be moved directly, with respect to L-PBF in which the laser is reflected by mirrors has more limitations about speeds.

A positive aspect of this kind of machines is that they have a larger working chamber and the micro-structural characteristics of the final pieces are similar to the ones of powder bed techniques, but with a lower resolution. Other advantages are the higher deposition rate (here there is not the time to wasted in SLM to spread powder since it is directly released in the melt pool by the nozzle); the possibility to have multiple powder feeders (use different materials) and the possibility to use this kind of machine not only to build pieces, but also for repairs and feature additions.

One drawback is the difficulty in the control of the nozzles: a 3-5 axis simultaneous motion requires more sophisticated software than the controls in L-PBF. The dimension of the melt pool is bigger than the PBF systems, this will lead to more stress and distortion in the piece and also to possible porosity, voids and defects. In general, DED processes are less accurate than PBF ones and for that there are less complex shapes. Also in the DED processes is used an inert atmosphere, the gas is directly provided by the nozzle.

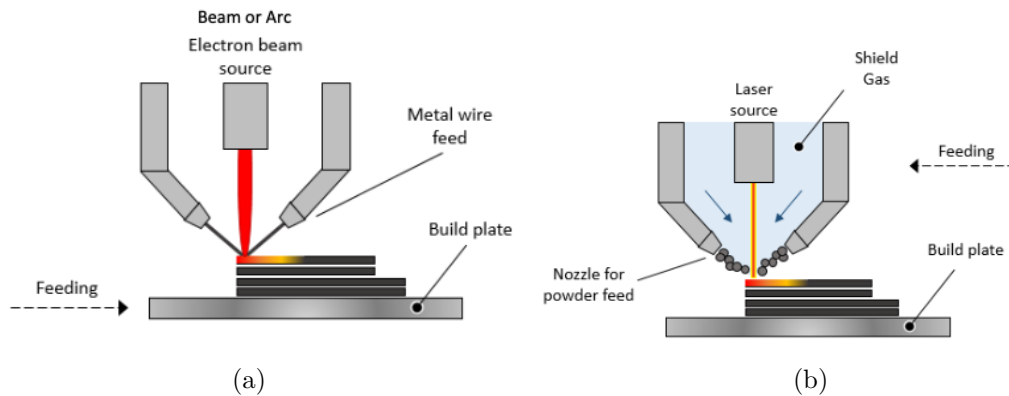


Figure 1.14: Directed Energy Deposition [1]: (a) Electron beam heat source with wire feeder; (b) Laser heat source with concentric nozzle to spread powder

## 1.6 Design for metal AM

In this section, some specific concepts are explained that will be used in the thesis. The analysis of the parameters for metal AM is not trivial: there are not optimized parameters. They depend on many factors: for example, it is not controllable precisely each particle of powder's dimension. Using the same machine and the same material with powders produced by different companies have different optimal parameters. Moreover, studying the melting pool's behavior is complicated; it has forces and thermal gradients that cannot be modeled by software more efficiently. For that, it is crucial to know at least the concepts that regulate the processes.

The two factors that affect more the resolution of the process are the laser profile and the powder characteristics. When the heat source impacts the powder bed, there is the creation of a melting pool: inside this one, there are several phenomena, such as Marangoni convection and evaporation (explained in depth later). Moreover, the boundaries between the melting pool and the powder can act as a potential permeation of the liquid phase into the powder; this effect is enhanced by the dynamic evolution of the melting pool. An advantage of the melt pool is that the flows inside it help breaking up the oxides layers on the surface, while a

disadvantage is the creation of vaporized metals: these cannot be controlled and can slightly change the process, to remove them gas flows are used.

It is also interesting how the heat source interacts with the powder. Both the laser and the electron beam are characterized by a Gaussian distribution with maximum intensity in the laser center and a radial decrease. The intensity can be evaluated as:

$$I(r, \omega) = I_0 \exp\left(-\frac{2r^2}{\omega^2}\right) \quad (1.1)$$

Where  $I$  = energy intensity,  $I_0$  = maximum intensity at the beam center,  $r$  = radial distance from the center of the beam and  $\omega$  = characteristics beam width, until the Gaussian distribution is of 1% of the peak intensity. When the energy impacts the powder, a part is absorbed. The remaining one is reflected; however, the reflection can escape from the bed or go between the particles and be completely absorbed. For this reason, the absorption rate of the powder is generally higher than the absorption of the solid material (that has higher reflection). However, it is also complicated to generalize a specific absorption value for a powder since its morphology is dependent on the producer.

Each powder has a Gaussian distribution regarding the dimension of the particles. It is essential because when the laser is applied to the powder bed, big particles' presence will cause defects in the final piece due to the porosity in the powder bed (relative density of the powder bed for larger particles is lower than the one for fine powder, figure 1.15) [66]. The influence of the powder bed is always related to the spreading system: it is possible to use rollers, comb blade, sweep blade, and moving hopper. The roller is characterized by a better powder bed density (good influence), but it also causes compressive and shear stresses that negatively affect the piece. While blades spreading systems, in general, generate fewer stresses in the powder bed, but has a lower bed density. However, the blade also has the side effect of filtering mechanisms for the bigger particles. The layer thickness influences the

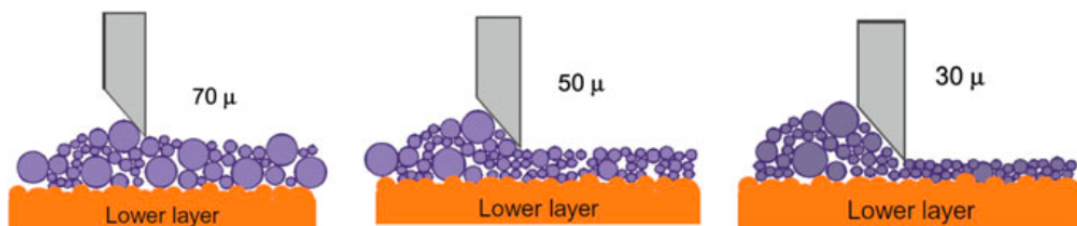


Figure 1.15: Powder spread using a blade for different layer thicknesses [66]

quality of the final piece. Its minimum value is equal to the diameter of the powder, and for that also, the dimension of the powder directly influences the quality: finer

particles have better packing densities and will achieve fewer defects in the part produced.

As we analyzed so far, the powder dimension has a Gaussian distribution, which obviously influences the melt pool stability. The software uses computational models to predict the thermo-mechanical neglect this factor and consider a spatially uniform bed. This kind of model can be used for the generic part but cannot simulate special features (e.g. thin walls). Also, the melt pool's capillary forces cannot be neglected, especially when the melt pool dimension is similar to the powder one, during the solidification of the track will cause the Plateau-Rayleigh instability (figure 1.16). This instability can affect the piece's roughness and can also

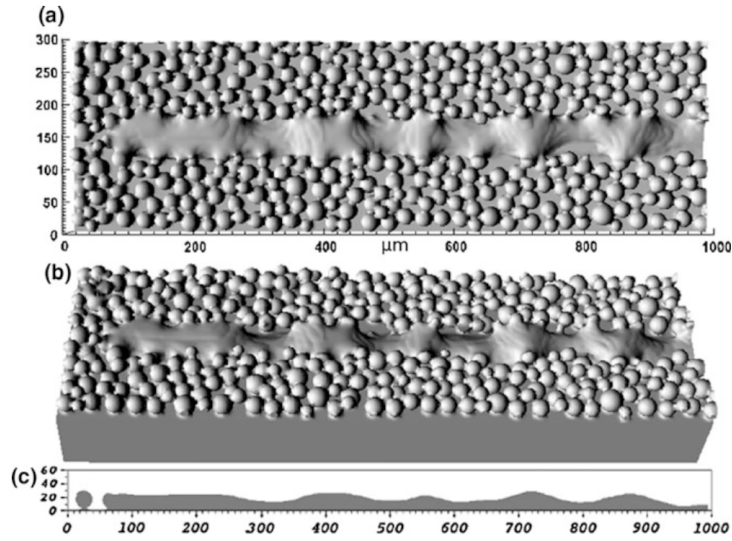


Figure 1.16: Effects of the Plateau-Rayleigh instability on a single track [33]

cause the balling effect: when the liquid of the melt pool segregates into spherical droplets. The influence of the parameters on this instability is not easy to be studied; however, can be linked to the energy density (equation (1.2)) in  $J/mm^3$ .

$$E = \frac{nP}{vtd} \quad (1.2)$$

Where  $E$  is the energy density,  $n$  is the repeated scanning,  $P$  is the heat source power,  $v$  is the scanning speed,  $t$  is the energy absorption thickness, and  $d$  is the energy absorption width. An excessive energy density can lead to a balling defect due to a liquid phase's long presence. However, it is necessary to analyze also the effect of the single parameters to comprehend the liquid-powder bed interaction: the balling phenomenon can be avoided by using slower speeds and higher powers (keeping constant the energy density).

In order to counter the effects of the Plateau-Rayleigh instability and the dis-homogeneity of the powder, it is suggested the use of thinner layer thickness and slower speed keeping constant energy [34]. The other effects that can be considered are the convection, the key-holes formation, and the evaporation in the melting pool.

The temperature distribution within the pool is not uniform due to the Gaussian distribution of the laser intensity and the heat source's motion. The gradient of temperature will cause flow in the melting pool called "Marangoni convection" [42]. It is possible to see from figure 1.17 that the temperature-surface tension gradients in the melting pool directly affect its shape and dimensions. The temperature will always be higher in the center of the melting pool due to the laser intensity distribution, so it is essential to focus on the materials' surface tension properties. If the surface tension is higher in the center (figure 1.17(b)), the Marangoni flow tends to create a deeper melt pool; while for a surface tension higher at the boundaries of the melt pool (figure 1.17(a)) there is a negative gradient and the Marangoni flow creates a wider and flatter pool. It can be interesting to know that the Marangoni convection can sometimes be used as a turbulence effect to break the oxides on the surface of reactive materials (e.g. aluminum, titanium).

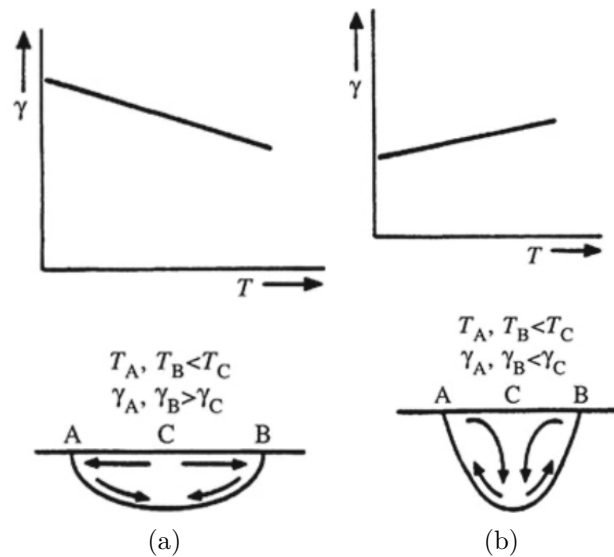


Figure 1.17: Marangoni convection in the melting pool, the flow motion depends on the temperature-surface tension gradient [42]: (a) Negative temperature-surface tension gradient; (b) Positive temperature-surface tension gradient

The keyhole effect and the evaporation are related [66]. It is easier to create vapor cavity defects in a deep melt pool because it is harder to go out from its end. Another aspect that should be considered is the use of atmospheric gas and its

properties. The type of the protection gas used affects piece density: argon has lower heat conduction than nitrogen, for that there is less heat loss during the production phase, and part density should be slightly higher.

The beam scanning strategy influences the piece's thermal history, thermal field distribution, and temperature gradients. Ideally speaking, the perfect scanning strategy should heat all the processed areas simultaneously. With an EBM process, thanks to the higher speed of the heat source, it is possible to use a "multi-spot" strategy, for which different points are heated up practically simultaneously. For a laser process, this concept cannot be applied: the scanning speed is slower than the EBM processes so that the temperature distribution will have larger thermal gradients. One way to affect the scanning strategy is changing the vector length: a shorter vector length will help in a shorter time until the re-heating of the same point (inline gradient of temperature). The use of shorter vectors length helps in reducing the residual thermal stress in the final piece. It is also possible to change

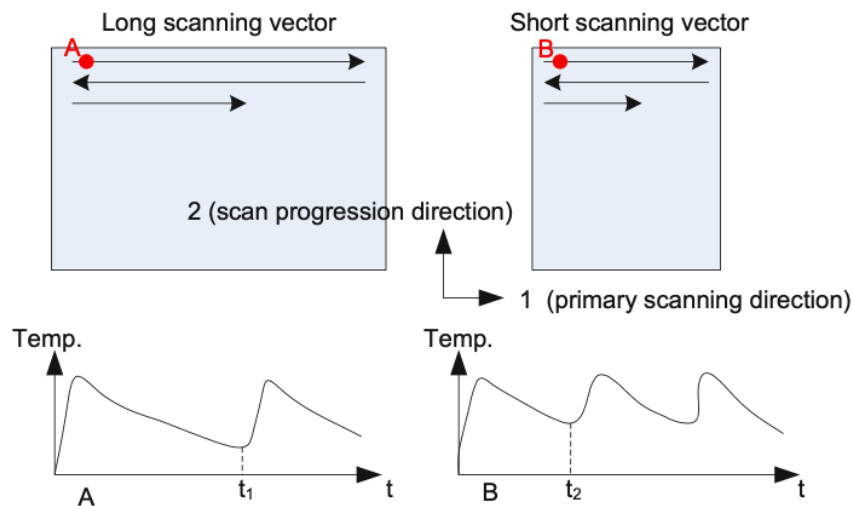


Figure 1.18: Thermal history of two different scanning strategies in which change the vector length [66]

the vector direction layer by layer. There are two ways 1.19: the first one is the "alternate scanning", for which the direction of all the layers is rotated by  $90^\circ$  each layer, and the second one is the "angular offset scanning", where the vectors are rotated by a fixed angle each layer. These two methods are used to decrease the anisotropy of the piece and the thermal distortion. It is reported that an alternate scanning strategy can reduce around 30 % of the thermal distortion with respect to a single direction scanning strategy [43]. By analyzing the residual stresses inside the single layer, it is possible to observe that the stress is created perpendicular to the primary scanning direction.

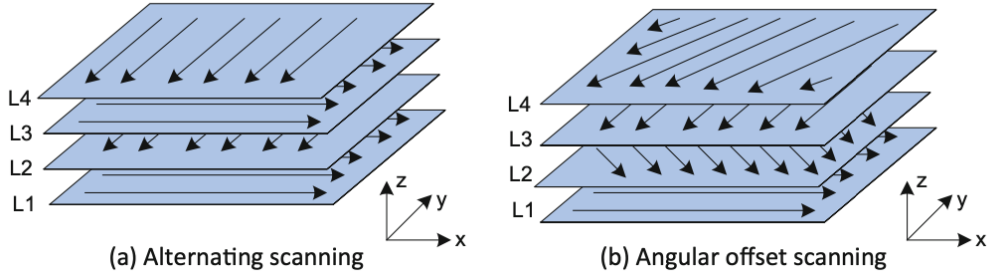


Figure 1.19: Relationship between thermal gradient and the scanning vector length [66]

Sometimes, for complex geometries or design constraints, there are limitations in the scanning vector's length, so it is also possible to change the scanning strategy by dividing the layer into sub-regions to decrease the overall vector lengths. Since the stresses are perpendicular to the primary scanning direction, having sub-regions with different scanning directions will reduce the stress in the layer. With this kind of scanning strategy, it is difficult to study the piece's temperature evolution, and there is also a more complicated process planning and control. Considering the control of thermal stress and the operation perspectives, it can be better to find a good compromise using a moderate sub-region dimension. On the other hand, it should also be considered the end-of-vector effect caused by the kinetic inertia of the hardware control that changes the thermal gradient.

Another aspect that must be kept in consideration is that the sample orientation during the fabrication influences the mechanical properties. In table 1.1 are reported some values of mechanical properties for SLM specimens in different materials.

Table 1.1: Benchmarks mechanical properties of AM metals specimens produced with SLM process

|          | E (GPa)           | Yield strength (MPa) | Ultimate strength (MPa) | Elongation (%) |
|----------|-------------------|----------------------|-------------------------|----------------|
| IN718    | 204 [61]          | 830 [4]              | 1120 [4]                | 25[4]          |
|          |                   | 898 [61]             | 1141[61]                | 22.6[61]       |
| IN625    | 204[44]           | 571[65]              | 915[65]                 | 49 [65]        |
|          |                   | 800[44]              | 1030[44]                | 10[44]         |
| 316L     | 183[19]           | 465[19]              | 555[19]                 | 13.5[19]       |
| AlSi10Mg | 73 [38]<br>68[29] | 243[38]              | 330[38]                 | 6.2[38]        |
|          |                   |                      | 391[29]                 | 5.2[29]        |
| Ti6Al4V  | 109.9[28]         | 736 [28]             | 1051[28]                | 11.9 [28]      |
|          | 109.2[57]         | 1110[57]             | 1267 [57]               | 7.3[57]        |
|          | 94[54]            | 1125[54]             | 1250 [54]               | 6[54]          |

### 1.6.1 Parameters

Several parameters can affect the L-PBF process; thus, this work will not consider all of them. Here the most relevant ones used during work for the downskin optimization are presented. The first parameter that is useful to control the melt pool's energy is the volume energy density (1.3). In equation (1.3)  $P$  is the laser power [W],  $v$  is the laser speed [mm/s],  $h_d$  is the hatching distance [mm] and  $t$  is the layer thickness [mm].

$$E_d = \frac{P}{v \cdot h_d \cdot t} \quad (1.3)$$

The layer thickness directly influences the quality of the piece (stair-stepping effect), for that it is usually chosen small. The smaller the value, the more the piece is precise; however, it will also affect the production time, since, for smaller layer thickness and a constant height of the piece, it will increase the number of layers.

The power and speed are usually related using a "process map" (figure 1.20) in which it is evident that for low speed and high power, there can be the balling defect or for low powers and high speeds, there is no connection. For that, it is better to stay in the central region and optimize parameters iterating. The hatching distance affects the porosity and the quality of the layer; if it is small, there is a bigger overlapping between the melt pools and a smaller probability to get pores. However, by using a small hatching distance, the time will increase too. These

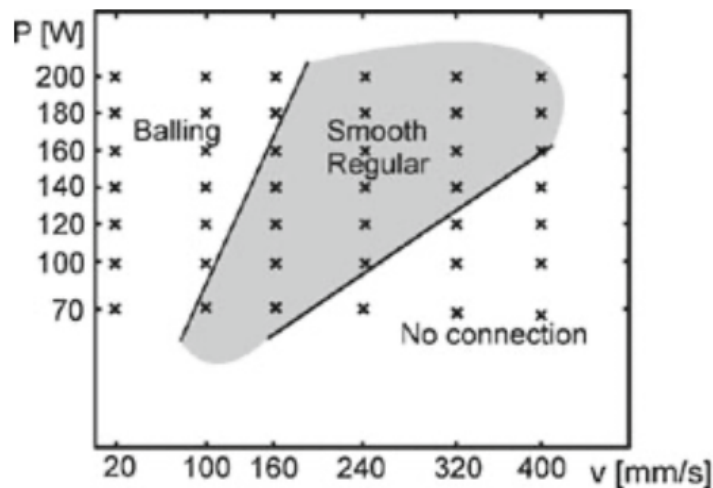


Figure 1.20: Typical process map for laser melting process. The material is a  $Fe - Ni - Cu - Fe_3P$  alloy [35]

kinds of maps are suitable for the core parameters and easy geometries; if we have to consider complex geometries, such as thin walls, we have to consider that the classic parameters do not allow a good production. For them, it is better to use

both combinations with the same power-to-speed ratio, but higher power and higher speed or lower power and lower speed (resulting in finer resolution) [64].

Another example can be for the overhanging surfaces: it is preferred to keep constant energy density, decrease the power and speed, or decrease the volume energy density to decrease the amount of heat that has to be dissipated. Another parameter that can be used is the linear energy density (1.4), which is the ratio between power and speed of the laser.

$$E_l = \frac{P}{v} \tag{1.4}$$



## Chapter 2

# Downskin limitations and potentials

This section will start the explanation of the internship and thesis work. Due to COVID19, the first months were spent working at home. Therefore, a in-depth bibliographic research has been done about downskin parameters. The results obtained are reported in the next section, "Downskin". During this period, the design of experiments made in Prima Industrie SpA were designed. It should also be specified that the following analysis about downskin parameters and problems is specific for the L-PBF process.

### 2.1 Downskin

Downskin is a term that indicates some layers (usually 1-4) above the supports or directly on the powder. Three layers are usually considered [30] and these should be processed with different parameters with respect to the layers of the "in-skin" or "core" parameters. Heat conduction varies depending on the relative density: the powder's heat conduction is one hundred times lower than the solidly supported zone [59]. The support, depending on the typology used, can dissipate more or less heat, but on the other hand, the more it dissipates heat (e.g. block support), the more it is difficult to be removed. In order to obtain good mechanical properties and surface finishing of the overhanging surfaces, it is better to use a solid/block support to dissipate more heat, but this will also lead to an increase in the cost in terms of material, printing time operation and post-processing operations. Apart from dissipating heat, there are other aims of support. These are meant to sustain the piece and counterbalance the tensile forces during the quick cooling of the melting

pools, causing a warpage (and eventually delamination) [55]. Often, the downward-facing surfaces can cause problems regarding shape and dimensional accuracy if they are not well supported.

This thesis aims to study the trade-off between the quality (good mechanical characteristics, dross formation, presence of warping) and the angle of the overhanging surface without supports. The inclined angle of an overhang surface is defined between the inclined surface and the horizontal plane. Some examples of overhanging surfaces are reported in figure 2.1.

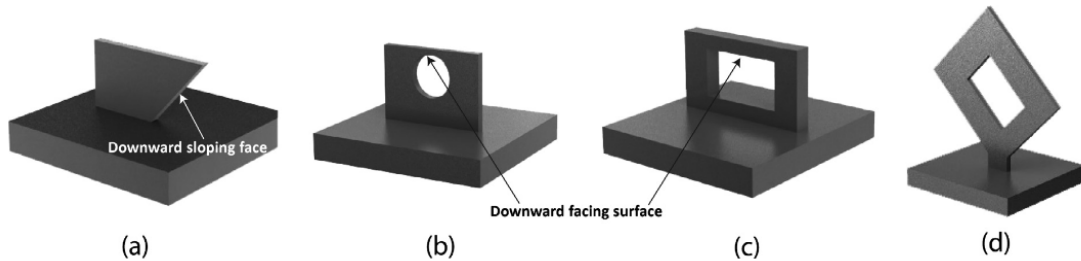


Figure 2.1: Example of overhanging surfaces [11]: (a) downward sloping face, (b) and (c) downward facing surfaces and (d) downward sloping faces

Depending on materials and parameters used during the printing operation, a critical angle is defined: it is the minimum angle that can avoid the structure's collapse without support. However, this value does not assure good surface and mechanical properties. It is essential to define the "reliable building angle" that is the minimum angle to achieve the production of surfaces without dross formation and detachments [58]. Considering an industrial point of view, the possibility to create overhanging surfaces without support by keeping a good quality (in terms of mechanical properties and surface finishing) is significant.

Several parameters influence the downskin quality [58]: inclined angle, residual stress accumulation, volume energy density, vector length on the overhanging surface fabrication, layer thickness (for the stair-stepping effect), scanning strategy, and the skin angle (figure 2.2). The main problems that occur when overhanging surfaces are printed without supports are warp [51], dross formation [30], and staircase effect [14].

When the laser impacts the powder, there is a melt pool, which dimensions are dependent on the volume energy density and the heat conduction of the previous layers. Since the powder's heat conduction is lower, for the same volume energy density, the melt pool in an overhanging surface without supports will be deeper and broader [11]. The melt pool can sink into the powder and cause dross formation on the downward-facing surface (figure 2.3); this leads directly to an increase in roughness and a bad dimensional accuracy.

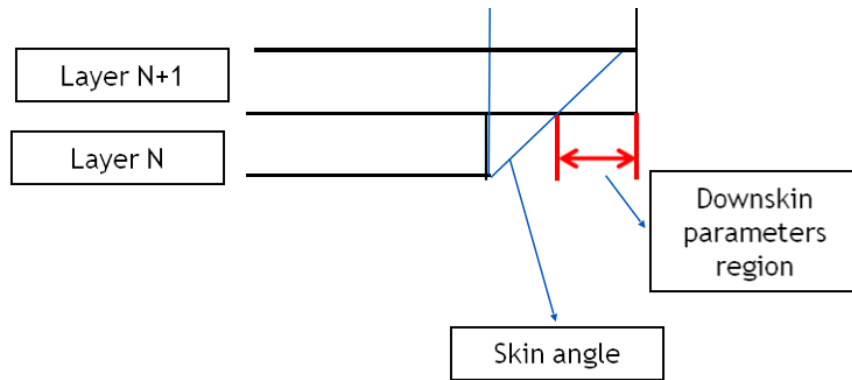


Figure 2.2: The skin angle is the angle that indicates the region in a layer for which are applied the downskin parameters

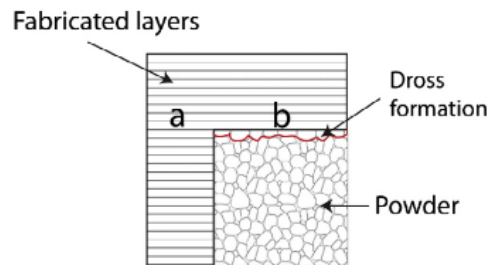


Figure 2.3: Dross formation in a downward facing surface [11]

Warping defect is caused by the rapid cooling of the melt pool: when the stress generated is higher than the material's strength, it causes a plastic deformation. Moreover, in overhanging surfaces without supports, the effect will be enhanced due to the lack of solid support that can counter the tensile stresses [58]. Another problem of the warp is that it can accumulate layer over layer. Due to the localized increase of height in the part of the layer unsupported (without the previous layer below) of the first layer with the warping, there will be less powder put by the recoater blade. Therefore, the heat conduction is lower, and the warp effect on the second layer becomes worse than the previous one. The part created will have lower mechanical resistance due to the defects by going on for several layers. If the height of the warping effect becomes higher than the layer thickness (figure 2.4), the recoater blade can hit the layer, causing a detachment. It is important to stop the printing operation to avoid the waste of time and possible damage on the blade.

The downskin, apart from the overhanging surfaces, it is also essential when it is needed to build a horizontal hole (figure 2.5). It is not the thesis's principal aim; however, using optimized parameters to make downward sloping faces without

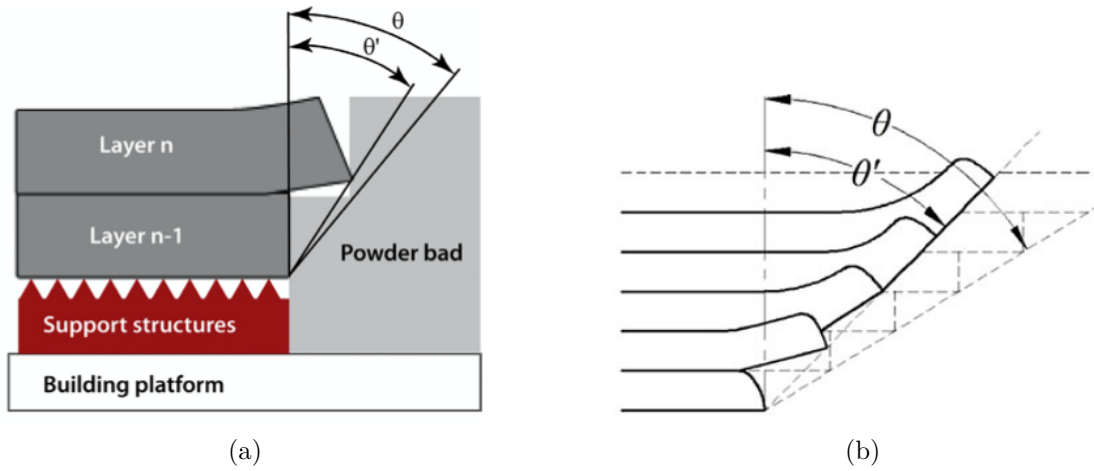


Figure 2.4: Warping effects:(a) in a downward sloping face [11];(b)Accumulation of warping effect[58]

support, it is possible to print horizontal holes without dross formation. This topic can be studied in another project: it is slightly different since the last layers of the upper half of the hole have smaller angles than those experimentally studied in the thesis.

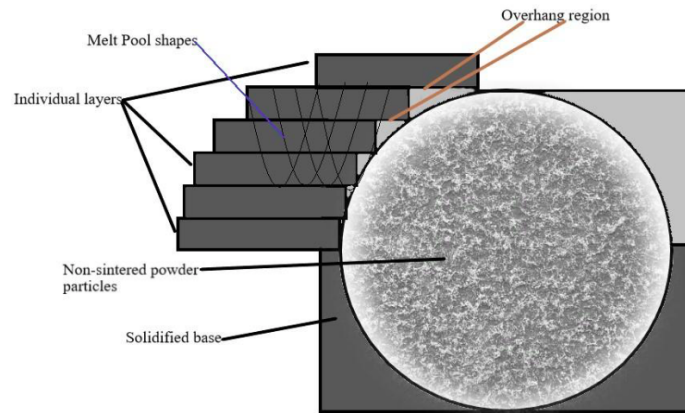


Figure 2.5: Overhanging surfaces in a horizontal hole [30]

## 2.2 State of the art on downskin parameters

Several parameters can affect the downskin quality; in literature, just some of them have been experimentally analyzed. Bassoli et al. [8] tried to figure out a general-

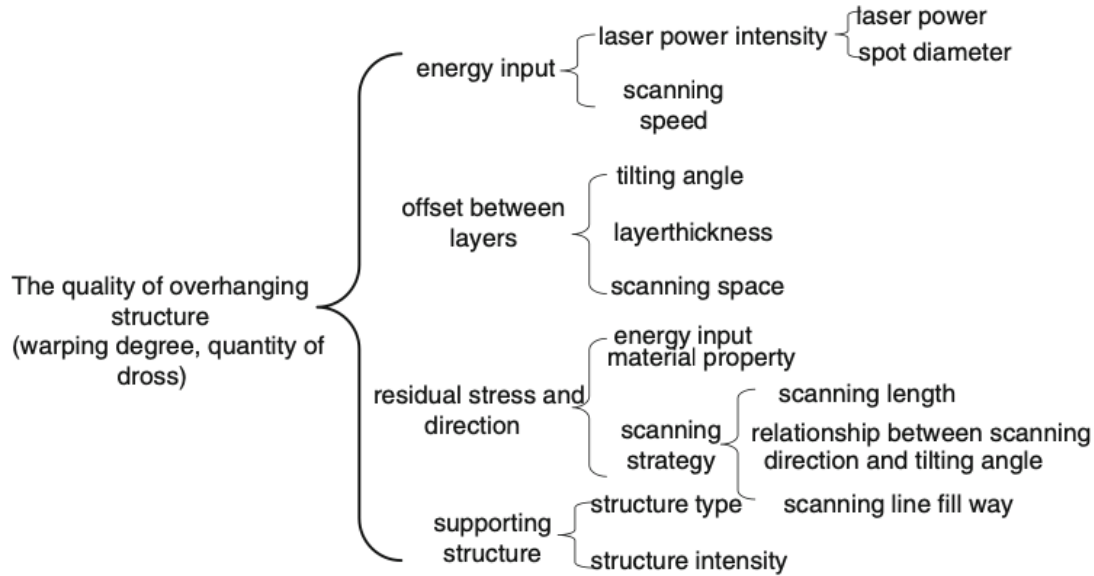


Figure 2.6: Parameters that affect quality of an overhanging surface by Wang [58]

ized holistic method to test parameters for all the steps in the fabrication of a piece with L-PBF. They consider as downskin surface just the horizontal layers above the support and not the ones of the oblique surface (figure 2.7). The proposed test is to try a  $3^3$  factorial design (changing power, speed, and hatching distance), starting from a value of volume energy density halved with respect to the core one and increasing/decreasing it by 20% ( $E_{d,downskin} = 50\%E_{d,core} \pm 20\%$ ). The key performance indicators (KPI) suggested are the absence of semidetached particles, cracks, and subsurface pores in the downskin surface. Since they print the oblique surface with core parameters, they are not interested in studying mechanical properties (influence of downskin layers with respect to all the layers of the piece is negligible).

Generally speaking, in order to use this method, the knowledge of the effects of each parameter in the equation of volume energy density would be requested. Indeed the starting point of decreasing the  $E_d$  can make the idea, but for a fixed  $E_d$  there are infinite sets of parameters and consequent different results.

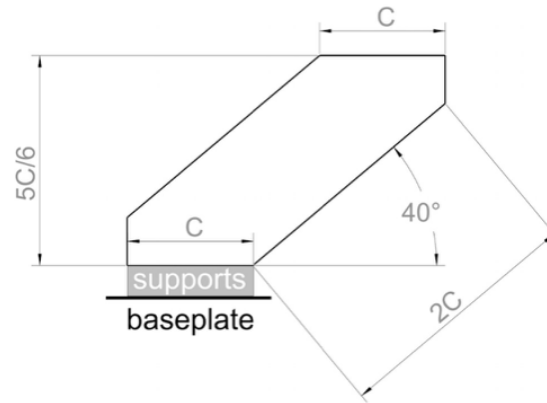


Figure 2.7: Specimen used in the generalized method [8]

### 2.2.1 Overhang angle

In this analysis, we will explore the effects of some parameters used in the downskin layers production. Downskin layers are considered, both the layers used to build a horizontal surface above the supports and the ones used to produce an oblique overhang surface. For the second case, the support structure is usually required for angles (the overhang angle is the one between the building plate and the downward-facing oblique surface) smaller than  $45^\circ$  [51]. This value is generic: each material has a specific minimum angle for which can be built without supports; indeed, other studies found values between  $20^\circ$  and  $45^\circ$  as critical angle [36].

Wang et al. [58] proposed a model to approximately evaluate the minimum building angle, depending on layer thickness and overhanging length "S" between two adjacent layers (figure 2.8). The equation used is:

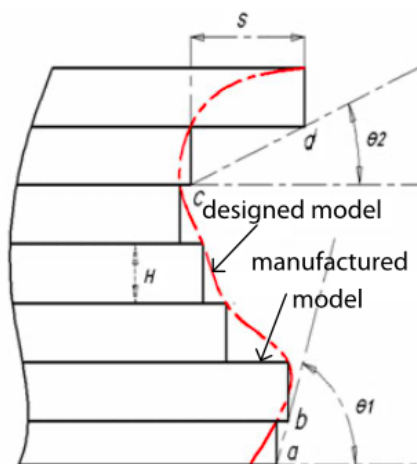


Figure 2.8: Slicing model of a typical curved surface [58]

$$S = H \cdot \text{ctg}\theta \quad (2.1)$$

Where  $H$  is the layer thickness,  $\theta$  is the inclined angle, and  $S$  is the overhanging length between two adjacent layers. For the same layer thickness, the smaller the angle, the smaller the tolerated overhanging length. The practical limit in operation is that the laser diameter in order to focus on the solid-supported zone must be smaller than overhanging length  $S$ . Imposing this value, it is possible to find the critical angle. Interestingly, the experimental results found in one of their experiments, in which they analyzed the influence of the speeds, are similar to the ones evaluated with this equation. The same equation (2.1) is also used effectively by Sarkar et al. [46] in two experiments: they also obtained an unsupported specimen with an angle slightly smaller than the critical one evaluated by the calculation.

It is important to notice that the equation's minimum critical angle does not analyze any feature of mechanical properties. Wang [58] specifies that by printing with minimum angle calculated by the equation, the resulting downskin surface has large dross formation and warping. Other studies, like the one of Covarrubias et al. [14] evidence that, by comparing two overhang oblique specimens built with an angle of  $60^\circ$  and of  $75^\circ$ , the one with the smaller angle has more visible partially melted particles, causing an increase in roughness. The effect of the parameters on the overhang angle should be analyzed in order to obtain not only an unsupported oblique surface without dross formation and warping but also with good mechanical characteristics to fulfill a production point of view.

The following studies will analyze different parameters to improve the quality of the downskin layers. However, some of them are only qualitatively analyzed, linking the effect of a parameter with the dross formation and warping without considering the specimens' mechanical properties. The downskin layers in a horizontal surface above the support structure are not a problem since they are just a few layers (1-4), and the vast majority of the piece is built with core parameters. While for the oblique overhanging surfaces, all the oblique parts of the piece should be constructed with downskin parameters (if it is built without supports), it is necessary to know the mechanical characteristics.

### 2.2.2 Power, speed and vector length

Wang et al.[58], in their research, analyzed the influence of speed and power in downward oblique surfaces. Their experiment uses a self-developed Dimetal-280 (a pre-commercial SLM workstation) with a maximum laser power of 200 W for a continuous wavelength of 1,090 nm Ytterbium fiber laser. The building envelope was a 280x280x240 mm, the scanning system used was a Dual Axis Mirror Positioning System and a Galvanometer optical scanner. The focused beam spot size of about 70  $\mu\text{m}$ . The inert atmosphere used is of argon or nitrogen with no more than 0.15%  $O_2$ . The powder used was a gas-atomized 316L stainless steel,

with a chemical composition (mass fraction, in percent): C (0.03), Cr (17.5), Ni (12.06), Mo (2.06), Si (0.86), Mn (0.3), O (0.09), and Fe (balance). The powder was spherical, and the size distribution (mass fraction, in percent) were lower than 15 (50 %), between 15-30 (40 %), and higher than 30  $\mu m$  (10 %), with a mean diameter of 17.11  $\mu m$ , and apparent density of 4.04  $g/cm^3$ .

Wang et al. initially studied the speed influence; the experiment consisted of setting all the parameters constant apart from speed and the overhanging surface angle. The constant parameters for the first experiment were laser power of 150 W, scanning space of 80  $\mu m$ , layer thickness of 35  $\mu m$ , number of layers of 100 (layer size 10x5 mm), and scanning strategy of inter-layer stagger followed by raster scanning, "refill scanning strategy" [15]. The speed varied from 200 mm/s to 1200 mm/s, while the angles are decreased from 50° to 25°. In their second experiment, Wang et al. repeated the same procedure changing the laser power with 120 W and 180 W values. By doing these two experiments, they can plot the influence of power, speed, and angles for the overhanging surface (figure 2.9), particularly for dross formation and warping effect.

The first experiment (figure 2.9 (b)) proves the importance of inclined angle and scanning speed for the fabrication quality. When the speed is  $v=200$  mm/s, the minimum building angle is slightly larger than 40°, while for a higher speed of  $v=600$  mm/s, the minimum building angle changes and became above 30°. By increasing the velocity at 800 mm/s, the minimum building angle changes into a minimum value of 25°. These results are consistent with the concept that both dross formation and warping effects are caused by a higher energy amount that cannot entirely be dissipated just from the powder. The drawback is that for higher speeds, so for lower volume energy density, it is penalized the part density (due to the layers' lower remelting). During the experiments, some specimens were stopped due to the accumulation of the warping effect. The minimum angle obtained is consistent with the results of equation (2.1).

The second experiment had the intention to demonstrate the effect of the laser power: by using a higher laser power and keeping constant the other parameters, the overhanging surface has a more massive warping effect. For a power of 180 W, with a speed of 200 mm/s, the minimum building angle is 45° (higher than the one for  $P=150$  W); for speeds higher than 800 mm/s, the minimum angle is stable at 30°. While using a lower power of 120 W, the minimum building angle decreases:  $v=200$  mm/s, angle of 35°, and for speeds greater than 600 mm/s, the angle is around 25° (figure 2.9).

Wang et al. also tried to analyze the scanning vector length effect: they tried to print two symmetric parts of a piece with different vector lengths of 20 mm and 80 mm. The results are visible in figure 2.10. The parameters used for this experiment are  $P=150$  W,  $v=200$  mm/s, layer thickness=35  $\mu m$ , scanning space=80  $\mu m$ . The

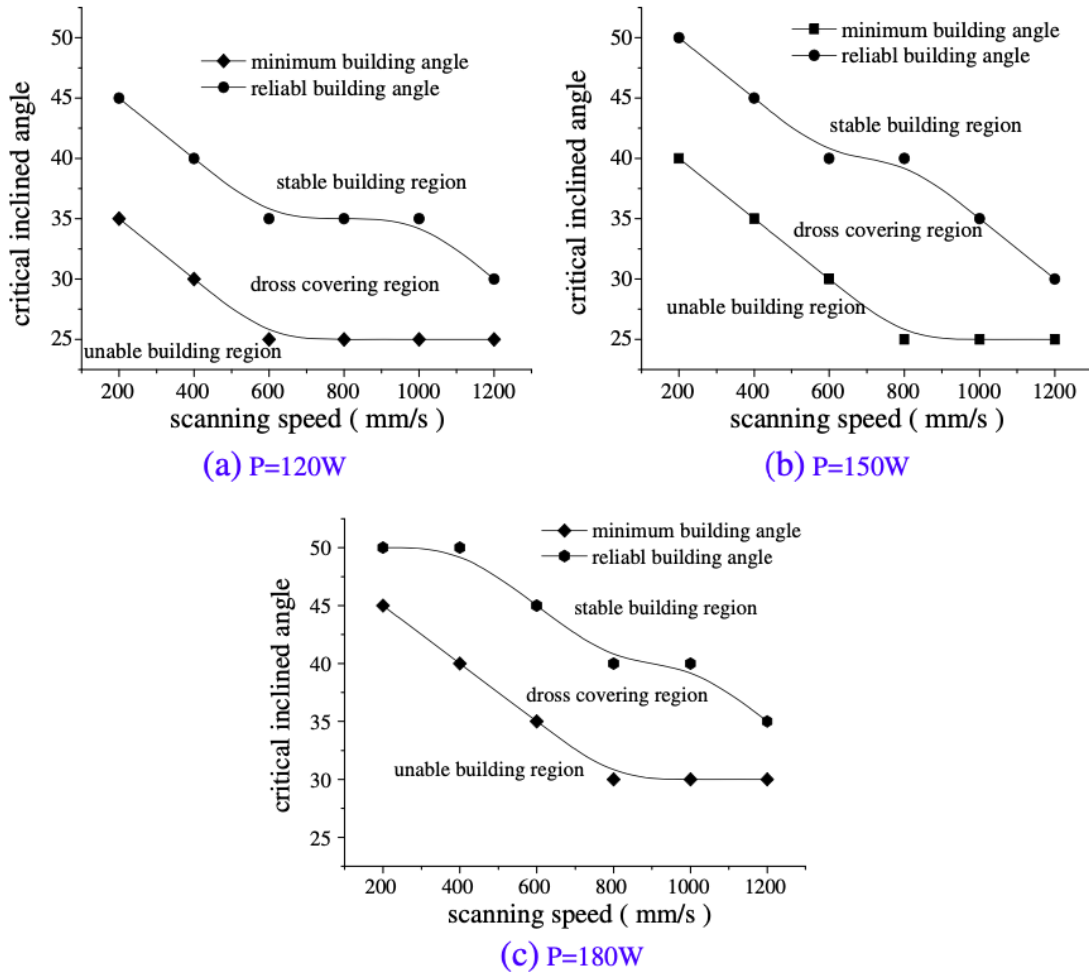


Figure 2.9: Relationship between critical inclined angle and scanning speed at different laser power (scanning space  $80 \mu\text{m}$  and layer thickness  $35 \mu\text{m}$ ). a) P=120 W, b) P=150 W, c) P=180 W [58]

results found are that the warping formation is enhanced by longer vectors, in which there is more accumulation of internal stresses. The direction of the scan is parallel to the long side of the cross-section. This conclusion is consistent with the results of Matsumoto's analysis [39]: he used a FEM system to study, during the melting and solidification of the melt pool, elastic deformation, and thermal conduction. Matsumoto also concluded that the warping is directly proportional to the vector length.

It is essential to underline that there are no tests for the mechanical properties of the specimens in this publication. The minimum building angle is the smallest angle that can support an oblique overhang surface without support. In contrast,

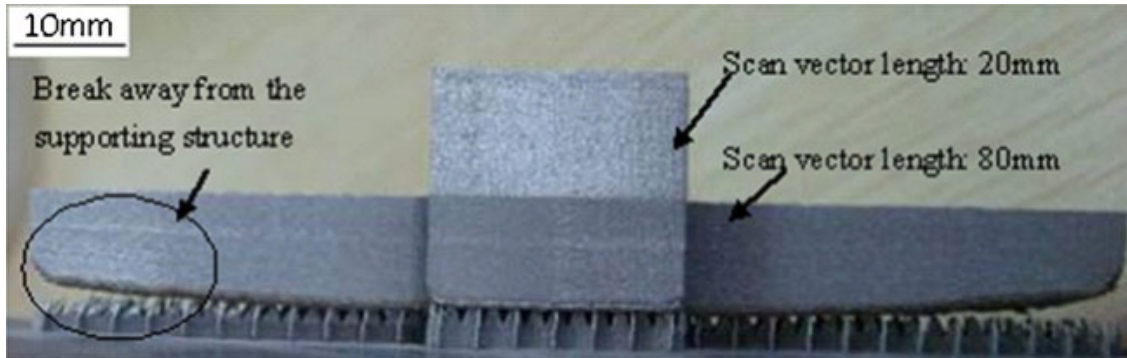


Figure 2.10: Fabricating effect comparison for supported surfaces [58]

the reliable angle here is defined as the minimum angle that allows to build the structure without the support, dross formation, and warping effect. Considering an industrial point of view a reliable angle is not enough because specific mechanical characteristics and a maximum porosity are allowed in the piece. However, it is clear the effect of these parameters on an overhang surface. The same qualitative results, in terms of power and speed influence, are found by Calignano et al.[13].

### 2.2.3 Hatching distance

Calignano et al. studied the influence of process parameters for Hastelloy X [13], a nickel superalloy produced by laser powder bed fusion. The powder used is a gas-atomized Hastelloy X provided by EOS GmbH, with particle sizes ranging from 23 to 63  $\mu\text{m}$  and percentage weight composition: 22Cr-18Fe-9Mo-1.5Co-0.6W-0.1C-1Si-1Mn-0.5Al- 0.15Ti-bal. The machine used was an EOSINT M270 Dual-mode system equipped with a Yb-fiber laser. The maximum laser power of 200 W and a beam spot size of 100  $\mu\text{m}$ . The building platform is heated at 80°C to reduce thermal stresses. Calignano et al. produced cubic samples of 10mm x 10mm x 10mm under Ar atmosphere ( $O_2 < 0.10\%$ ). The samples are created using the same parameters for down-skin, in-skin (or core), and up-skin. The parameters changed between samples are laser power (P), scanning speed (v), and hatching distance ( $h_d$ ). Some parameters are kept constant: stripe width (5mm), the overlap of stripes (0.12mm), the layer thickness (20 $\mu\text{m}$ ), and the contour parameters (P=150 W and v=1250 mm/s). The scanning direction is rotated of 67° for each layer to increase the piece's final density and isotropic properties. Firstly, they analyzed the specimens and found the optimized set of parameters. The second step was to change parameters to reduce the detachment of the downskin layers from the supports.

They highlighted the problem of optimization for the first layers above the support structure. In the downskin layers, there is a difference in terms of energy released

(due to the parameters' variation from support to part production). This difference causes variations in the melting pool, thus a risk of deformations and detachments from the support structures (figure 2.11). Indeed, heat sink role of supports from the melting pool is important to decrease thermal stresses and counterbalance the recoating blade's force, which can create a dynamic pressure against the leading edge of the layer. The values used for the tests regarding the downskin values are

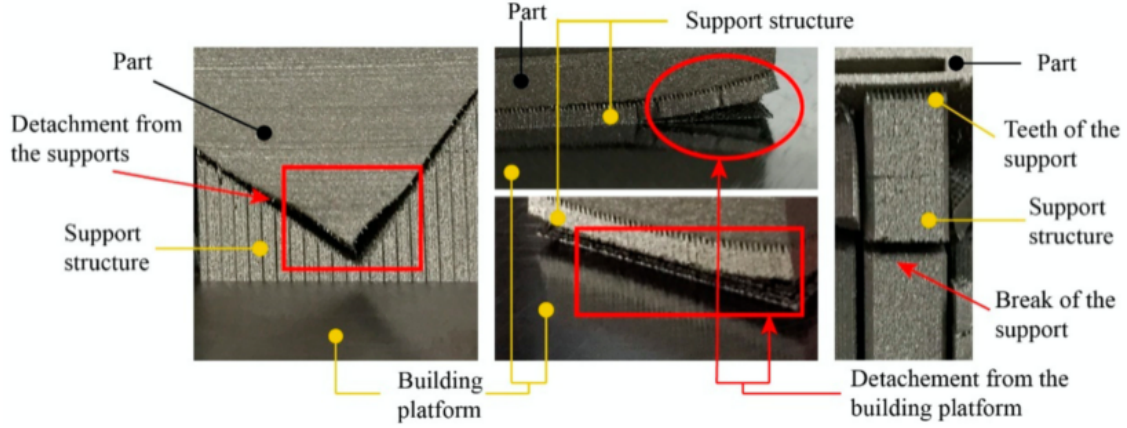


Figure 2.11: Detachment between support and part (left), detachments of the support from the building platform (center), breaking of the support (right) in manufacturing for Inconel 718 [13]

reported in table 2.1

Table 2.1: Process parameters, volume energy density and linear energy density for downskin and support

|                         | Sample | P (W) | v (mm/s) | $h_d$ (mm) | $E_d$ (J/mm <sup>3</sup> ) | $E_l$ (J/mm) |
|-------------------------|--------|-------|----------|------------|----------------------------|--------------|
| Down-skin<br>(2 layers) | 1      | 195   | 1000     | 0.05       | 195.00                     | 0.195        |
|                         | 2      | 170   | 1000     | 0.05       | 170.00                     | 0.170        |
|                         | 3      | 195   | 1000     | 0.08       | 121.88                     | 0.195        |
|                         | 4      | 195   | 870      | 0.08       | 140.09                     | 0.224        |
|                         | 5      | 170   | 870      | 0.08       | 122.13                     | 0.195        |
|                         | 6      | 170   | 1000     | 0.08       | 106.25                     | 0.170        |
|                         | 7      | 170   | 870      | 0.05       | 195.40                     | 0.195        |
|                         | 8      | 195   | 870      | 0.05       | 224.14                     | 0.224        |
| Supports                | -      | 80    | 400      | -          | -                          | 0.200        |

In the table the three parameters that are studied and the corresponding volume (1.3) and linear (1.4) energy density are reported. The support parameters are already optimized for Hastelloy X to avoid detachment between the preheated plate and support. Amongst all the specimens printed (figure 2.12 (a)), the best result

is the one obtained from sample 6; all the other specimens have balling problems with consequent delamination due to the blade impact. The support structure used is a block type, showed in figure 2.12 (b), made of thin walls and powder, thus the heat conduction is lower than the one of bulk material. For this reason, to avoid cross formation in the downskin surface, it should be better to have less heat to be dissipated in the melt pools. It is interesting to notice that sample 6 is the one with the lowest volume energy density. This is consistent with the idea that it is better to decrease energy for downskin layers. However, it is more interesting to analyze the results obtained with respect to the linear energy density: both sample 2 and sample 6 have the lowest  $E_l$ , but the downskin quality is different (figure 2.12 (a)). Thus, it is evident the importance of the hatching distance concerning the quality of the downskin, a result that confirms other researches [9, 12]. The thickness layer has always been kept constant, and for that is not mentioned. The dependence of the volume energy density to the hatching distance is inversely proportional: the higher the  $h_d$ , the lower the  $E_d$  ((1.3)). The best result obtained has the highest value of hatching distance.

The mechanical properties of the core part are independent from the parameters of downskin (here used for two layers (table 2.1)), so the choice of the parameters for the support and downskin layers is mainly important to avoid large internal stresses and delaminations. Indeed, the specimens printed with core parameters of  $P = 195W$ ,  $v = 1000mm/s$ ,  $h_d = 0.05mm$  and  $t = 20\mu m$  (layer thickness), have a high density (99.88%) and are built without cracks.

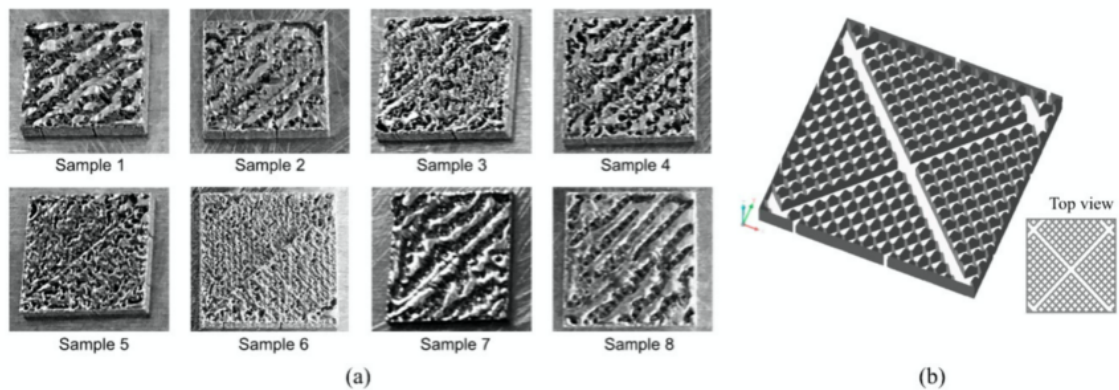


Figure 2.12: (a) Interface between support structure and downskin layers; (b) support structure of block type [13]

## 2.2.4 Scanning strategy and aspect ratio

Sarkar et al. [46] studied the quality of overhang oblique surfaces without supports. They compared the effects, with respect to the angle, of the scanning strategy and the "aspect ratio" (figure 2.13a) by keeping constant laser power and speed. After they analyzed the results using a scanning electron microscopy (SEM) to investigate the presence of dross formation and warping. The machine used was an EOSINT M270 SLM, with a 200 W CW Yb-fiber laser. Material used is EOS Stainless Steel PH1, composition w %: 0.07 C, 1.0 Mn, 1.0 Si, 14-15.5 Cr, 3.5-5.5 Ni, 2.5-4-5 Cu, 0.15-0.45 Nb and 0.5 Mo. The fixed process parameters are  $v=800$  mm/s,  $P=150$  W, beam diameter=  $80 \mu\text{m}$ ,  $t=20 \mu\text{m}$ . Sarkar et al. evaluated the

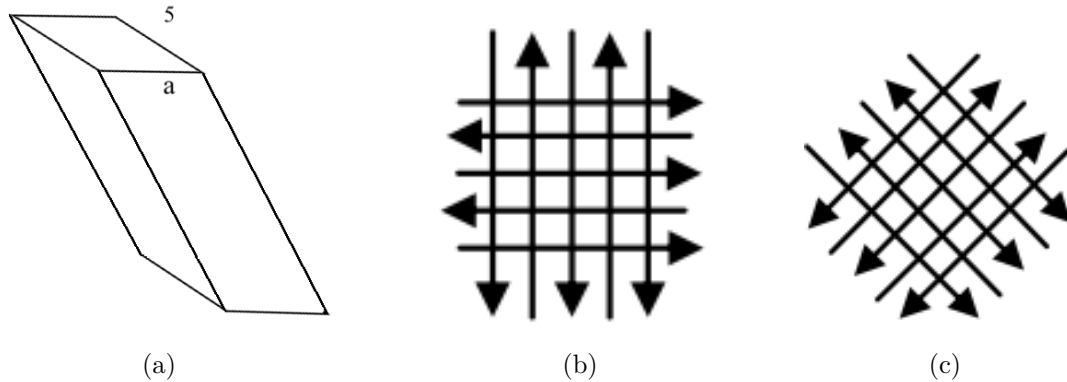


Figure 2.13: Experiment: (a) Specimen used, the aspect ratio is  $a:5$ , with  $a= 5, 3.5, 2.5$ ; (b) Linear scan strategy; (c) Alternate scan strategy

minimum critical angle by using the same equation (2.1) of Wang [58]: for the parameters used ( $t=20\mu\text{m}$  and laser beam radius=  $40\mu\text{m}$ ), the critical angle is  $\theta = 26.565^\circ$ . At first, they studied the angle influence qualitatively: by keeping constant the parameters and decreasing the angle between the oblique surface and building plate from  $50^\circ$  to  $25^\circ$ , there is an increase of warping and dross formation. This result is consistent with the others analyzed so far [11, 13, 58]: when the angle decreases, there is a consequent decrease of the overhang length; if it is smaller than the beam diameter, there will be a consequent dross formation. Moreover, the overhang surface is unsupported: since the powder has heat conduction coefficient lower than the bulk material, the melt pool's dimensions are more significant, and there is a consequent formation of dross.

It is interesting to see the influence of the aspect ratio. The values of the parameter "a" used are 2.5 (ratio 1:2), 3.5 (ratio 3.5:5), and 5 (ratio 1:1). It is possible to see in figure 2.14 the results obtained. Here they used a fixed angle of  $25^\circ$ . Increasing the ratio, there will be a worsening in warping and dross formation. This effect is caused by the larger contact area between the lower overhang oblique surface and

unmelted powder. Practically, a larger contact area will cause a decrease in heat conduction and, for that, a warp.

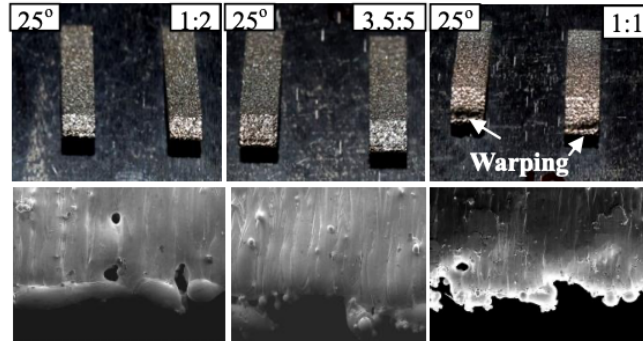
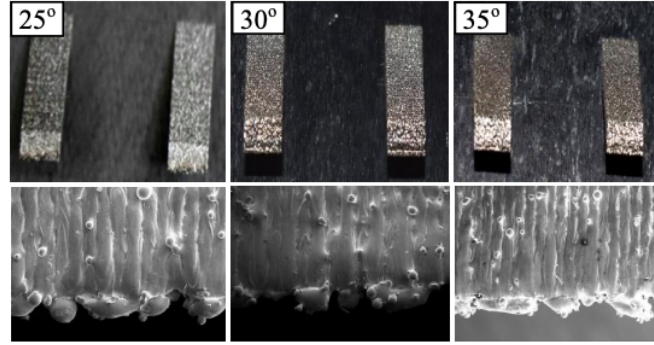


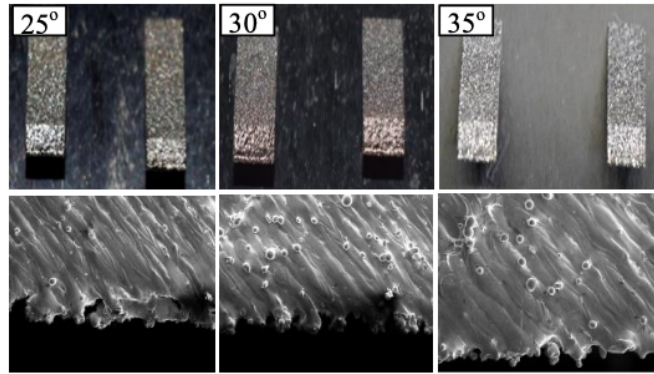
Figure 2.14: Specimens obtained with different aspect ratios(above) and SEM images(below)

After they analyzed the effect of the scanning strategy, using fixed parameters, they produced three specimens with the angles of  $25^\circ$ ,  $30^\circ$ , and  $35^\circ$  using a linear scanning strategy (figure 2.15(a)) and an alternate scanning strategy (figure 2.15(b)). By using a linear scanning strategy, there is the same scanning direction for every layer. This factor will increase density energy: the overhanging edges get repetitively heated up in the same regions. By changing the scanning strategy into an alternate one, the result is a decrease in energy density. The results agree with the theoretical explanation: qualitatively, using a lower energy density both the degree of warping and the dross formation are decreased. The minimum angle obtained in this experiment was found to be  $25.343^\circ$ , lower than the theoretical minimum critical angle obtained by the equation (2.1) of  $26.565^\circ$ .

What is lacking in these experiments is a quantitative analysis of the specimens: it is possible to print with an angle of  $25.343^\circ$ , but we do not know anything about the pieces' mechanical properties. It is interesting to know the qualitative effects of these two parameters, especially since mechanical properties are dependent on materials, powders, and machine characteristics used.



(a)



(b)

Figure 2.15: Experiment: (a) Linear scanning strategy; (b) Alternate scanning strategy

### 2.2.5 Number of layers and pre-sintering

Khan et al. [30] studied the influence of the number of layers printed with downskin parameters above a horizontal hole (figure 2.5). The upper half of the horizontal hole can be seen as an inclined overhang with continuous decrements of the angle; for this reason, it fits in this analysis of downskin process parameters. The study uses an SLM EOSINT M 290 machine and a  $AlSi_{10}Mg$  powder. The fixed parameters are the layer thickness ( $30\mu m$ ), spot size diameter ( $100\mu m$ ), and the scanning strategy, alternate at  $67^\circ$ . The experiment was based on printing several cubes (dimension  $5 \times 5 \times 5 mm^3$ ) with different processing parameters (varying laser power, speed, hatching distance, and finally, the number of downskin layers) for core layers (tab 2.2). For the downskin and upskin layers, the parameters used are the ones provided by EOS and have been kept constant:  $P_{downskin} = 360W$ ,  $v_{downskin} = 1000mm/s$ ,  $P_{upskin} = 340W$ ,  $V_{upskin} = 1150mm/s$ . A small hole of diameter  $0.5mm$  is placed in the center of the cube. It is also analyzed the influence of a pre-sintering strategy on the quality of the hole.

Table 2.2: Parameters used in the first experiment [30]

| S. No | Skin Power | Scan Rate | Hatching | Pre-Sinter P | Pre-Sinter v | Pre-Sinter h |
|-------|------------|-----------|----------|--------------|--------------|--------------|
| 1     | 370        | 1300      | 190      |              |              |              |
| 2     | 370        | 1300      | 190      | 180          | 900          | 130          |
| 3     | 340        | 1150      | 210      |              |              |              |
| 4     | 340        | 1150      | 210      | 180          | 900          | 130          |
| 5     | 360        | 1000      | 210      |              |              |              |
| 6     | 360        | 1000      | 210      | 180          | 900          | 130          |
| 7     | 300        | 1000      | 190      |              |              |              |
| 8     | 370        | 1600      | 190      |              |              |              |
| 9     | 370        | 2000      | 210      |              |              |              |
| 10    | 340        | 2000      | 210      |              |              |              |

The results obtained for the horizontal hole show dross formation for the upper half: the high volume energy density combined with low heat conduction, due to the powder below the downskin layers, cause a broad and deep melt pool. Also, the pre-sintering application does not show lower dross formation. In figure 2.16 ANSYS analysis are reported for the depth of the melt pool in the first layer: both the sets of parameters used formed a melt pool more profound than the layer thickness, that will also melt the powder below the layer. This uncontrolled melting is the cause of dross formation.

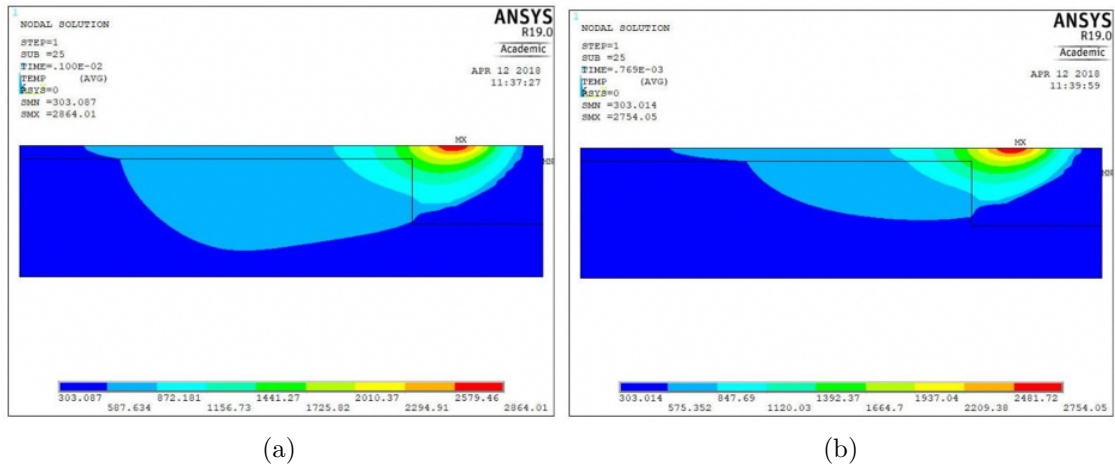


Figure 2.16: Temperature distribution and melt pools [30]: (a) Downskin parameters P=360 W, v=1000 mm/s; (b) Core parameters P=370 W, v=1300 mm/s

Khan et al. also simulated the melt pool's depth using different parameters and comparing the differences between the powder and solidly supported melt pools.

The result in figure 2.17 shows that the solid-supported layers have melt pools with depth lower than the powder supported ones. The horizontal hole quality of some

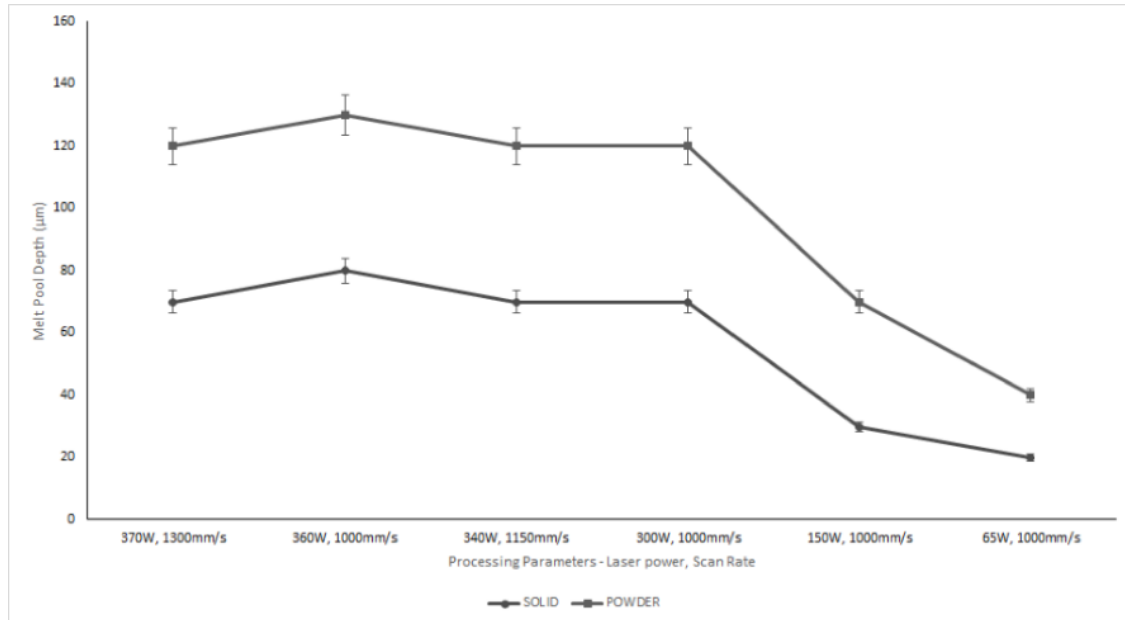


Figure 2.17: Melt pool depth for different parameters. The upper line represents the values obtained for the powder supported layers, while the bottom line identifies the solid supported layers [30]

specimens is analyzed with an SEM and is reported in figure 2.18; all the holes are characterized by massive dross formation. It is possible to conclude that the pre-sintering does not affect the quality of the hole, and also that it is not possible to avoid dross formation with these parameters.

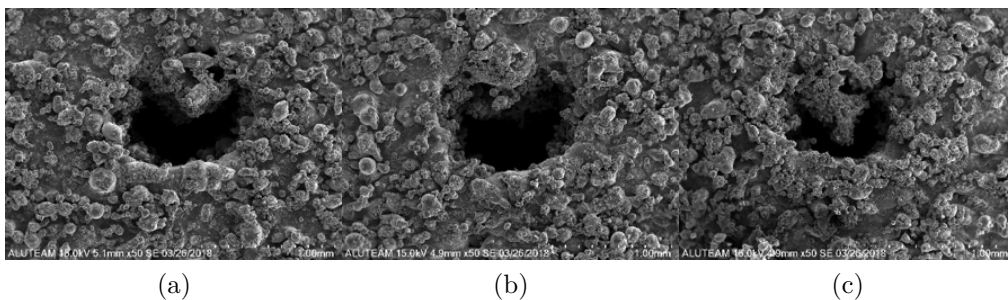


Figure 2.18: SEM images for some specimens in table 2.2: (a) specimen 1 ; (b) specimen 3;(c) specimen 6

The second experiment aims to study the influence of downskin parameters, which are a fundamental constraint for the quality of overhanging surfaces [50]. Usually

three downskin layers are processed, but here it is studied to change this number of layers into 4,5 and 6. Increasing the distance between the powder below the downskin and the first core layer (characterized by higher volume energy density and a deeper melt pool) should be possible to decrease or avoid the dross formation. If the melt pool's depth with core parameters is smaller than the height of all the layers printed with downskin parameters, the dross formation should be avoided. The parameters used are reported in table 2.3.

Table 2.3: Parameters used in the second experiment [30]

| S. No | Laser Power | Scan Rate | Layers |
|-------|-------------|-----------|--------|
| 1     | 65          | 1000      | 3      |
| 2     | 65          | 1000      | 4      |
| 3     | 65          | 1000      | 5      |
| 4     | 65          | 1000      | 6      |
| 5     | 150         | 1000      | 3      |
| 6     | 150         | 1000      | 4      |
| 7     | 150         | 1000      | 5      |

The results obtained by changing these parameters are always better in term of dross formation than the previous ones (figure 2.19).

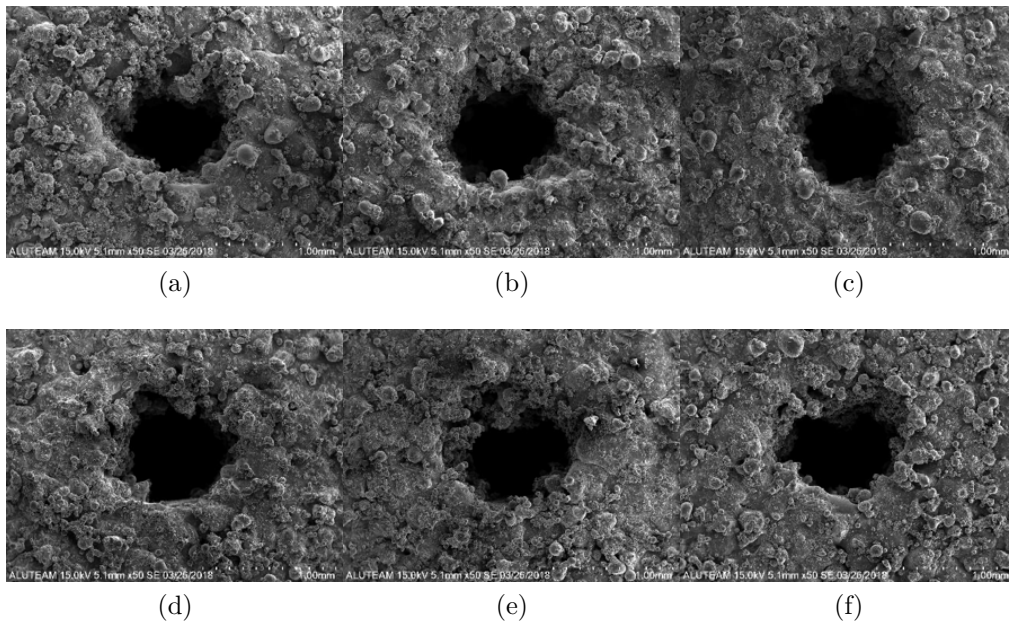


Figure 2.19: SEM images for some specimens in table 2.3: (a) specimen 1; (b) specimen 2; (c) specimen 3;(d) specimen 4; (e) specimen 5;(f) specimen 6

Among all the second experiment specimens, the best ones are the numbers 2,3 and 4 that show a small dross formation. These specimens are the ones with lower laser powers and several processed layers with downskin parameters higher than 3. Khan et al. also provided the ANSYS analysis for these two powers used: depths of the melt pools are reported in figure 2.20.

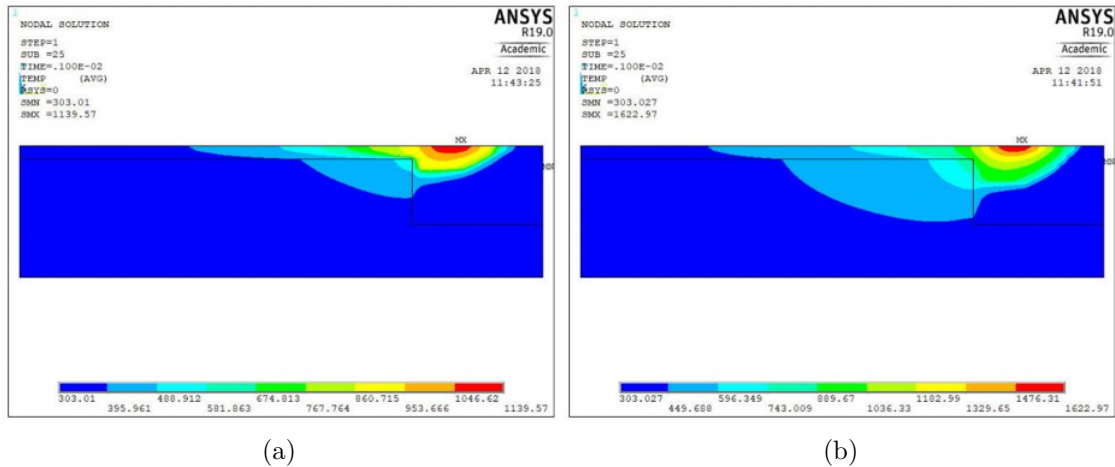


Figure 2.20: Temperature distribution at: (a) P=65 W and v=1000m/s; (b) P=150 W and v=1000mm/s

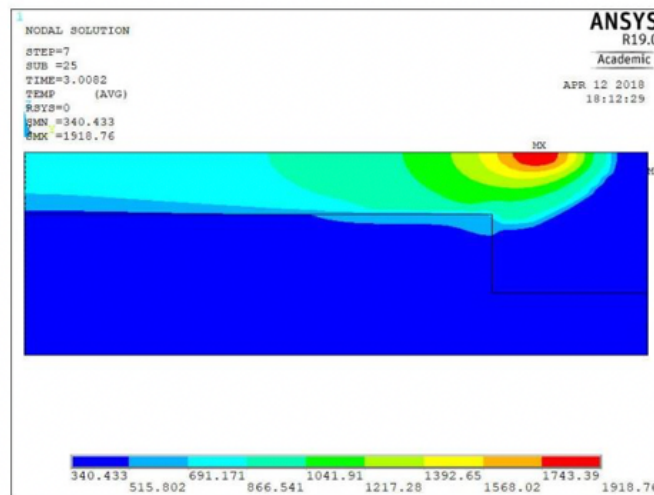


Figure 2.21: Temperature distribution for the 4th layer printed with core parameters (360 W, 1000 mm/s) after 3 parameters done using downskin parameters (65 W, 1000 mm/s).

The melt pools' depth is lower with respect to the ones for the first experiment in the first downskin layer. For the layers above the first one, the heat prefers to

escape to the previously solidified layer (higher heat conduction [16]) than going to the less conductive region of the powder [31].

Finally, Khan et al. used the numerical analysis to study the effect of the first layer printed in core parameters: it is important to study this layer's depth, which must not pass through all the downskin layers or will cause dross. The numerical analysis is made in the situation for which the first layer with core parameters is printed after three downskin layers (figure 2.21). It is possible to observe that the pool's depth is larger than three layers, causing dross formation. This evidence is consistent with the SEM images analyzed previously in which, by increasing the number of layers processed with downskin parameters from 3 to 4, the dross formation is decreased. However, from figure 2.19, it is also possible to see that when the number of layers done with downskin parameters (65W) increases, the region printed with downskin parameters has a larger number of pores due to insufficient liquid penetration.

# Chapter 3

## Material and machine

### 3.1 Machine

Prima Industrie SpA has two different L-PBF machines: the Print Sharp 250 and the Print Genius. The main difference is that the Print Genius has two lasers to print pieces, increasing production speed simultaneously. The machine used for the experiments is the Print Sharp 250, figure 3.1a.



Figure 3.1: Print Sharp 250 pictures: (a) External picture; (b) Inside view.

The main components of the machine are:

1. Electrics Components:
  - Program Logic Control (PLC)
  - Machine interface

- Switching Cabinets

## 2. Optics components:

- Laser: it is located on the right side of the machine, here it is generated the laser used in the process;
- Collimator: the laser beam is transferred from the generation point to the collimator in order to narrow beam particles;
- Beam Expander: the laser, after the collimator, goes into the beam expander. Three different lenses make it: the entry lens for a focused position, the entry lens for the defocus position, and the exit lens.
- Scanner: it is the final mirror that direct the laser in the right direction to produce the piece;
- F-Theta lens: After the scanner, the laser pass through the F-theta lens, here it is focused on the right point to be melted.

## 3. Mechanics components:

- Blade: it is used to spread the powder on the platform. Depending on the application, a soft recoater, made in silicon, does not detach/delaminate the part if there are collisions. This type of blade is easily deformed. The other possibility is to use a hard recoater made of steel. This one can be used in the production of easy pieces that do not create any problem in the fabrication;
- Building axis;
- Dispenser: it is the unit in which there is the powder for the production;
- Collector: it is used to collect the powder used in the process. After the powder is filtered and mixed with virgin powder to be used in another process;

## 4. External units:

- Chiller: it is used to chill the water arriving from a circuit heated by the laser and the scanner. There are two different circuits, where the water is at slightly different temperatures, around 25°. It is used distilled water without additives.
- Gas recirculating unit: It is needed in order to separate the gas and the dust. The gas goes into a filter, and the dust is collected in the carbon dust collector (downward the external unit on the left of the machine). While the clean gas is used again in the printing process.

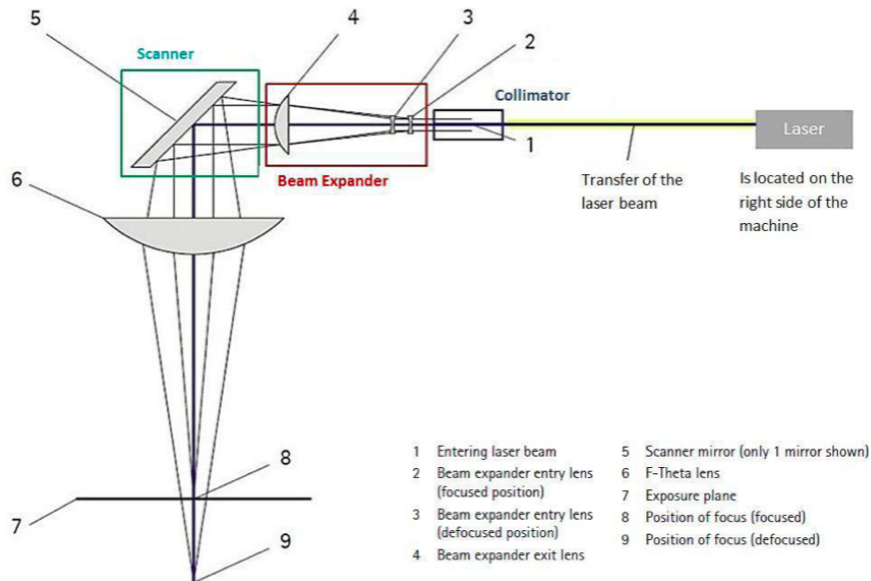


Figure 3.2: Description of the optical systems used in the Print Sharp 250

## 3.2 Superalloys and Inconel 718

Superalloys are alloys made of Nickel, Nickel-Iron, or Cobalt with a high quantity of alloying elements to increase mechanical resistance at high temperatures (up to 1000°C-1100°C) [5]. Among all of them, the Nickel superalloys (e.g. Inconel 625, 718, and Rene 41) are the ones with higher characteristics: thermo-mechanic fatigue between 540°C and 1000°C [7], good corrosion resistance at high (up to 1000°C) temperatures, damage tolerance, and tensile properties. For all these reasons, the superalloys are used in engines, gas turbines (high thermo-mechanical stresses), and where is needed a good corrosion resistance [44]. Nickel superalloys, in particular, are used in specific fields: aerospace [47], chemical [62], nuclear reactor [40], petrochemical industries, medical applications and marine [45].

Due to the increased characteristics of superalloys, it can be difficult to cast or forge them [37] but it is not problematic to melt their powders using an L-PBF machine. The super-alloys matrix is austenitic " $\gamma$ ", with an FCC (face-centered cubic) structure at every temperature. This cell typical of ductile materials, and it can be hardened for solid solution or precipitation.

Inconel 718 is a nickel superalloy; precipitation strengthened thanks to the precipitation of the phase  $\gamma'$ . It has good workability, high mechanical characteristics, and good fatigue resistance. In Inconel 718, there are alloying elements providing solid solution strengthening or precipitation strengthening, increasing the material's high-temperature strength, such as Titanium, Aluminum, and Niobium. Due

to the high presence of alloying elements and other phases (e.g.  $\gamma', \gamma''$ ), the Ni-based superalloys are susceptible to crack generation [67].

There are several phases, and not all of them have positive effects on the structure [10]:

- $\gamma'$  : it is a solid solution of chemical composition  $Ni_3Ti$ ,  $Ni_3Al$  (or intermetallic mixed  $Ni_3(Al, Ti)$ ) coherent with the matrix and stable at high temperature, it leads to higher mechanical characteristics of the alloy. It can be found under different shapes: can be spherical, globular, cuboidal, or block. The increase in mechanical resistance has the knockback of a decrease in workability; for this reason, the volume percentage of  $\gamma'$  is lower than 40% in Inconel 718 [7];
- $\eta$ : it is a phase, with chemical composition  $Ni_3Ti$  and HCP (Hexagonal Closed Packed) structure, that reduces mechanical characteristics. It derives from  $\gamma'$  substitution for long times, and its formation is enhanced by a high quantity of Ti and  $\gamma'$  [10];
- $\gamma''$  :it is a metastable compound of  $Ni_3Nb$ , with a tetragonal crystal system (body-centered). It is the main strengthening precipitation in Inconel 718, and it precipitates in the shape of nanometer size disks. It is formed at temperatures between 650 °C and 870 °C. Since it is a metastable phase, for long heat treatments will occur a transformation into  $\delta$  phase [18];
- $\delta$  : the chemical composition is  $Ni_3Nb$  with an orthorhombic structure. It precipitates due to thermal exposition around 815 °C and 900 °C or for longer times also at lower temperatures [10].

Other alloying elements present in the Inconel 718:

- Mo, Co, W, V, Cr are elements that strengthen the alloy for a solid solution;
- Al, Cr, La, Y, Ce can enhance corrosion resistance and oxidation at high temperatures;
- Cr, Ta, Mo, Hf, W, Ti, Nb are metallic elements at a high melting point that can form carbides. In IN718 most commons carbides are MC,  $M_6C$  and  $M_{23}C_6$ , these can reinforce the grain boundaries and stop dislocations, but on the other hand, they decrease ductility of the material (increase brittleness) and also use Cr or Mo (which percentages are always low in Inconel 718, usually below 0.1% [49], leading to a decrease in corrosion resistance.

There are also phases that it is better to avoid because of decrease resistance and ductility of the alloy. These are phases with a TCP (Topological Closed Packed) structure, and there are mainly three of them (for superalloys in general):

- $\mu$  : it is a phase with a rhombohedral structure and chemical composition

$(Fe, Co)_2(Mo, W)_6$  , this phase is present in alloys with a high quantity of tungsten or molybdenum;

- Laves: this one is the most important among the three for Inconel 718. The chemical composition is  $(Fe, Mn, Cr, Si)_2(Mo, Ti, Nb)$  with a hexagonal structure. It has irregular morphologies such as globular or disks at the grain boundaries. The main effect of this phase is the brittleness of the material;
- $\sigma$  : tetragonal structure phase that can appear in several chemical compositions ( $FeCr, FeCrMo, CrFeMoNi, CrCo, CrNiMo$ ). This phase has an irregular shape [10].

In additive manufacturing, the "as-built" microstructure of Nickel superalloys has elongated grains in the z-direction. Usually, due to the melt pool's rapid cooling, the structure is metastable, and it needs post-heat treatment to obtain better results. A heat treatment process is HIP (Hot Isostatic Pressure), to reduce porosity, and favour material's recrystallization or some aging processes.

The possible defects for superalloys are residual porosity due to keyhole, balling, and cracking. The keyhole defect appears when the volume energy density is too high, more specifically for high powers and low speeds. In these conditions, the melt pool will become bigger and with a "keyhole" shape: gasses risk to get trapped during the solidification, causing a residual porosity in the piece. The balling defect will appear in the opposite conditions, so a low volume energy density (low powers and high speeds). The laser has not the possibility to melt all the particles. It creates a ball-shaped agglomeration that causes the next layer an impediment to a fresh powder's uniform deposition, leading to an increase in porosity or even delamination (if the bonding between layers is weak and there are thermal stresses) [25].

There are several ways to create cracks [10]:

- strain-age hardening: cracks due to the high presence of alloying elements (Ti and Al) that can generate discontinuities or porosity if the material is subjected to heat treatments;
- micro-cracks: interdendritic zones may be liquid during solidification, causing a collapse of the dendritic zone;
- liquation cracking: here, there is the nucleation of the cracks at the grain boundaries. The eutectic phase  $\gamma'$  and carbides with a low melting point in the boundaries are present. So, there are thin liquid layers that, during the deposition process, are subjected to strong stresses and can generate cracks
- formation of precipitates along grain boundaries plus the high dislocation density can bring to cracks nucleation.

It is possible to reduce these defects by acting on the alloy composition and the process parameters, such as volume energy density and scanning strategy.

### 3.2.1 Inconel 718

Here the composition of the powder used for the printed specimen is reported. It is an essential factor for the mechanical characteristics and the repeatability of the experiments. The powder used by Prima Industrie SpA is made by the company Oerlikon using a gas atomized process [23].

Table 3.1: Powder composition: nominal weight percentage of the elements present in the powder [23]

| Nominal Weight % | Ni      | Cr | Fe | Nb+Ta | Mo | Al  | Ti | Others |
|------------------|---------|----|----|-------|----|-----|----|--------|
| MetcoAdd<br>718C | Balance | 18 | 18 | 5     | 3  | 0,6 | 1  | <0,5   |

Table 3.2: Powder dimensions and characteristics [23]

|                  | Nominal<br>Range [ $\mu m$ ] | D90<br>[ $\mu m$ ] | D50<br>[ $\mu m$ ] | D10<br>[ $\mu m$ ] | Hall<br>Flow [s/50 g] | Apparent<br>Density [ $g/cm^3$ ] | Morphology |
|------------------|------------------------------|--------------------|--------------------|--------------------|-----------------------|----------------------------------|------------|
| Metcoadd<br>718C | -45 +15                      | 46                 | 30                 | 18                 | <18                   | 4 to 5                           | Spheroidal |

To make a comparison with the results of the next experiments, in figure 3.3 are represented the mechanical characteristics and the roughness of "as built" pieces in Inconel 718 by General Electric (GE) Additive [2].

**PHYSICAL DATA AT ROOM TEMPERATURE**

|          | Surface Roughness - Overhang<br>( $\mu\text{m}$ ) |     |     | Surface Roughness<br>( $\mu\text{m}$ ) |    |
|----------|---|-----|-----|--|----|
|          | 45°   | 60° | 75° | H                                      | V  |
|          | Upskin  | 14  | 12  | 11                                     | 15 |
| Downskin | 19  | 14  | 12  | 8                                      |    |

| Thermal State | Porosity<br>(% Density) |      | Hardness<br>(HV10) |     | Poisson's Ratio |    |
|---------------|-------------------------|------|--------------------|-----|-----------------|----|
|               | H                       | V    | H                  | V   | H               | V  |
|               | As-Built                | 99.9 | 99.9               | 280 | --              | -- |
| SOLN+AGE      | 99.9                    | 99.9 | --                 | --  | --              | -- |

**TENSILE DATA**

Tensile testing done in accordance with ASTM E8 and ASTM E21

Temperature: RT

| Thermal State | Modulus of Elasticity<br>(GPa) |     | 0.2% YS<br>(MPa) |      | UTS<br>(MPa) |      | Elongation<br>(%) |      | Reduction of Area<br>(%) |    |
|---------------|--------------------------------|-----|------------------|------|--------------|------|-------------------|------|--------------------------|----|
|               | H                              | V   | H                | V    | H            | V    | H                 | V    | H                        | V  |
|               | As-Built                       | 193 | 153              | 735  | 605          | 1045 | 969               | 29.7 | 34.3                     | -- |
| SOLN+AGE      | 191                            | 174 | 1110             | 1045 | 1420         | 1350 | 16.5              | 17.0 | --                       | -- |

Figure 3.3: Mechanical characteristics and downskin roughness for a piece built by General Electric Additive Manufacturing [2]

Analyzing the literature, Fox et al. reported the downskin roughness values at different angles, found using several values of power (ranging from 40W to 200W) and speed (ranging from 350 to 3000 mm/s) [17]. The material used was EOS StainlessSteel GP1. Their results are reported in figure 3.4. The minimum roughness obtained is above  $27 \mu\text{m}$  for angles lower than  $40^\circ$ .

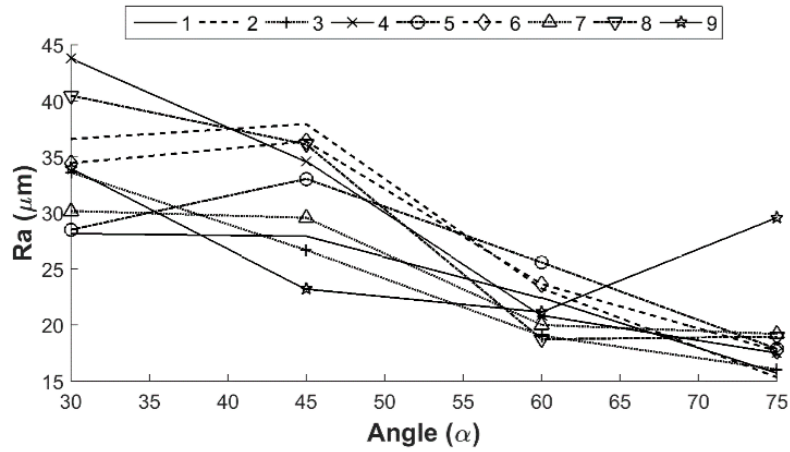


Figure 3.4: Downskin roughness values for different angles at several levels of power and speed [17]

# Chapter 4

## Experimental Procedure

In this chapter the methods of the thesis are explained. The design of experiments (DoEs) developed to optimize the downskin parameters for Inconel 718 are analyzed.

### 4.1 DoE 1-Roughness evaluation

The first design of the experiment aims to try all the possible combinations of parameters (power, speed, and hatch distance) to study the behavior of the dross formation and the specimen's feasibility.

First of all, it is necessary to decide a shape for the specimen to test the parameters. Combining the dimension of the specimen previously used by Prima Additive and the shape used in a paper [8], it is obtained the one in figure 4.1.

The specimens are drawn using SolidWorks (figure 4.1(a)). Changing the angle was impossible to keep all the measurements constant. It was decided to keep the specimen's height fixed, consequently increasing the length with the decrease of the overhang surface angle.

It was then necessary to perform the piece's slicing and write on the specimen the angle used. It is done using the software Materialise Magics. It also converts the STL file into a CLI file that is divided into layers. During the slicing operation, it is necessary to decide the layer thickness. In this thesis, it is used equal to  $40\mu\text{m}$ .

The third step is to pass the CLI file into the EPHatch software. In this one, the parameters are set for both the core and the downskin regions. There are several parameters, apart from the power, speed, and hatching distance. The others kept in consideration are the number of the downskin layers (number of layers above a downskin region) by keeping in consideration the paper [30], using four layers.

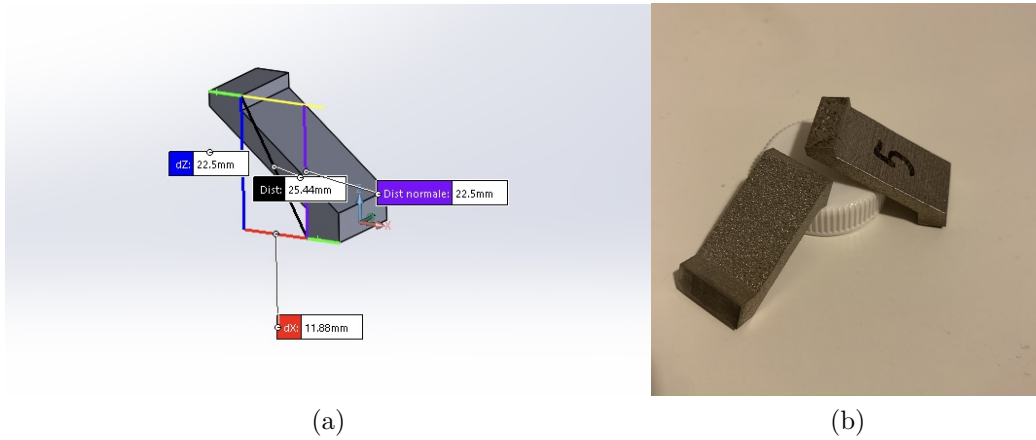


Figure 4.1: Representations of the specimens used for the experiments: (a) drawn specimen in SolidWorks; (b) real printed specimen

The offset region, the area in which the laser will scan two times with both the parameters (downskin and core), is set to 0.06 mm. The last one is the skin angle, modified to  $1^\circ$  (it is impossible to put  $0^\circ$ ): when the angle is near  $0^\circ$ , it means that all the region of the layer that is printed above the powder has downskin parameters (figure 4.2(b)). This choice should maximize the effect of the downskin parameters.

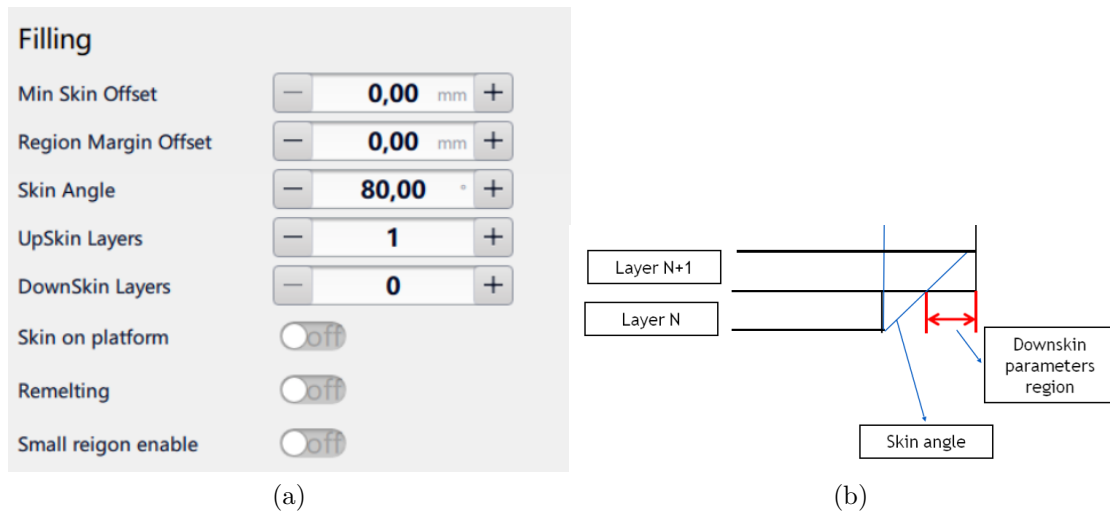


Figure 4.2: EPHatch software interface and example: (a) EPHatch software interface with standard parameters; (b) graphic representation of the change in the skin angle.

The starting parameters are the downskin ones used by Prima Industrie SpA. Modifying them, it has been developed a factorial  $3^3$  experiment. These values have been

chosen by checking the order of magnitude of papers [27] and [58]. Both power and speed have been decreased by 10% and 15% to check the improvement of reduced energy density. It has been decided to test two values for the hatch distance, one higher and one lower than the one used by Prima Industrie SpA. The experiment consists of printing specimens at three different angles, each with all the possible parameter combinations of the factorial  $3^3$ . These are reported in table 4.1. For that, in this experiment, there will be 27 sets of parameters with three possible angles, for a total of 81 specimens. The angles considered for this DoE are  $30^\circ$ ,  $35^\circ$ , and  $40^\circ$ . In table 4.1 are written the 27 sets of parameters; later in the text, each specimen will be recalled with the number representing it and the angle used.

Table 4.1: DoE 1: Parameters used to print specimens. The 27 sets of parameters are used for each angle ( $30^\circ$ ,  $35^\circ$ , and  $40^\circ$ ).

| <i>Specimen</i> | $P_{down}$ [W] | $v_{down}$ [mm/s] | $h_{d,down}$ [mm] | $VED$ [ $J/mm^3$ ] |
|-----------------|----------------|-------------------|-------------------|--------------------|
| 1               | 0,85P          | v                 | $0,73h_d$         | 16,05              |
| 2               | 0,85P          | v                 | $h_d$             | 11,67              |
| 3               | 0,85P          | v                 | $1,27h_d$         | 9,17               |
| 4               | 0,85P          | 1,1v              | $0,73h_d$         | 14,6               |
| 5               | 0,85P          | 1,1v              | $h_d$             | 10,61              |
| 6               | 0,85P          | 1,1v              | $1,27h_d$         | 8,43               |
| 7               | 0,85P          | 1,15v             | $0,73h_d$         | 13,96              |
| 8               | 0,85P          | 1,15v             | $h_d$             | 10,14              |
| 9               | 0,85P          | 1,15v             | $1,27h_d$         | 7,97               |
| 10              | 0,9P           | v                 | $0,73h_d$         | 17,00              |
| 11              | 0,9P           | v                 | $h_d$             | 12,36              |
| 12              | 0,9P           | v                 | $1,27h_d$         | 9,71               |
| 13              | 0,9P           | 1,1v              | $0,73h_d$         | 15,45              |
| 14              | 0,9P           | 1,1v              | $h_d$             | 11,24              |
| 15              | 0,9P           | 1,1v              | $1,27h_d$         | 8,83               |
| 16              | 0,9P           | 1,15v             | $0,73h_d$         | 14,78              |
| 17              | 0,9P           | 1,15v             | $h_d$             | 10,75              |
| 18              | 0,9P           | 1,15v             | $1,27h_d$         | 8,44               |
| 19              | P              | v                 | $0,73h_d$         | 18,90              |
| 20              | P              | v                 | $h_d$             | 13,73              |
| 21              | P              | v                 | $1,27h_d$         | 10,79              |
| 22              | P              | 1,1v              | $0,73h_d$         | 17,16              |
| 23              | P              | 1,1v              | $h_d$             | 12,48              |
| 24              | P              | 1,1v              | $1,27h_d$         | 9,81               |
| 25              | P              | 1,15v             | $0,73h_d$         | 16,42              |
| 26              | P              | 1,15v             | $h_d$             | 11,94              |
| 27              | P              | 1,15v             | $1,27h_d$         | 9,38               |

Finally, the specimens have been separated from the building plate with an electric discharge machine by a third part company. The key performance indicator used in the first DoE is the roughness value of the downskin surface. It has been evaluated using a roughness tester, represented in figure 4.3, in the plant of Prima Industrie.



Figure 4.3: Roughness tester used in Prima Industrie SpA

## 4.2 Repeatability test

After printing all these specimens, it is necessary to characterize them. It would be too time expensive to polish and analyze all these specimens. Therefore, an initial selection was made to eliminate broken specimens, and a second one exploring the roughness values. It has been chosen to continue the analysis avoiding the angle of  $30^\circ$  since no one showed promising results. In figure 4.4 are represented the print phase and the finished specimens removed from the machine: the ones inclined at  $30^\circ$  are broken. The excluding criteria used consists of selecting the specimens with a roughness value lower than  $21\mu\text{m}$  for both  $40^\circ$  and  $35^\circ$ . In the end, eight sets of parameters have been chosen to be printed other two times. The repeatability is accepted if the new values stay in a range of  $\pm 6\%$  with respect to the first one.

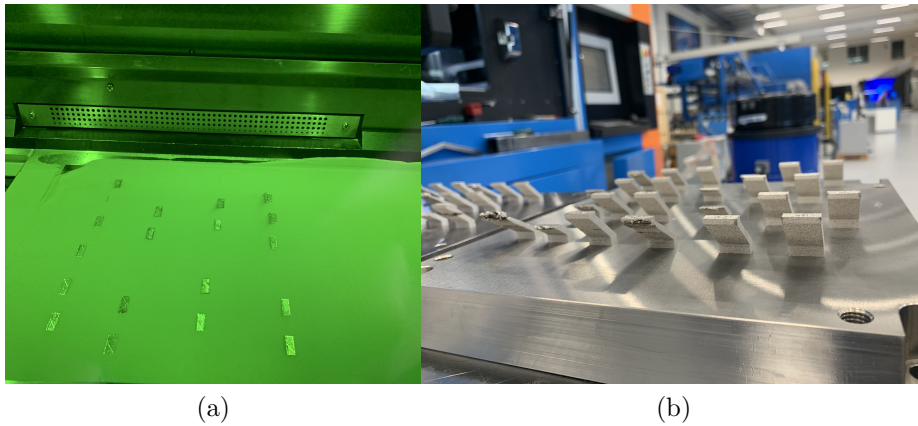


Figure 4.4: Operations during DoE 1: (a) print phase for the specimens; (b) printed specimens attached to the plate

### 4.3 DoE 2-Porosity analysis

For the specimens that fulfill the repeatability requirement, the porosity in the downskin region is analyzed. The porosity is measured using an optical microscope; however, it is necessary to cut and polish the specimens before. The porosity value is an average of six different measurements made in other points of the downskin region.

The first step is the cutting of the specimens. The cutting machine used in Prima Industrie SpA is represented in figure 4.5. It has been used with a diamond blade at 290 rpm to cut Inconel's specimens. During the operations, to avoid overheating, sparks' creation, and excessive wear of the edge, two wires shoot a water and lubricant mixture on the blade.



Figure 4.5: Cutting machine used in Prima Industrie SpA

The second step is the polishing. It is necessary because the cutting machine causes a surface full of scratches, impossible to be analyzed directly with the microscope. While to obtain an excellent porosity result, it is necessary a mirror-polished surface. To increase productivity during the polishing operation, since the specimens were small, they have been merged with transparent resin using a Remet mounting press (figure 4.6(a)).

To polish the specimens several abrasive discs with different roughness are used. Starting with the disc P400 with the highest roughness (grain size  $35\ \mu\text{m}$ ), going

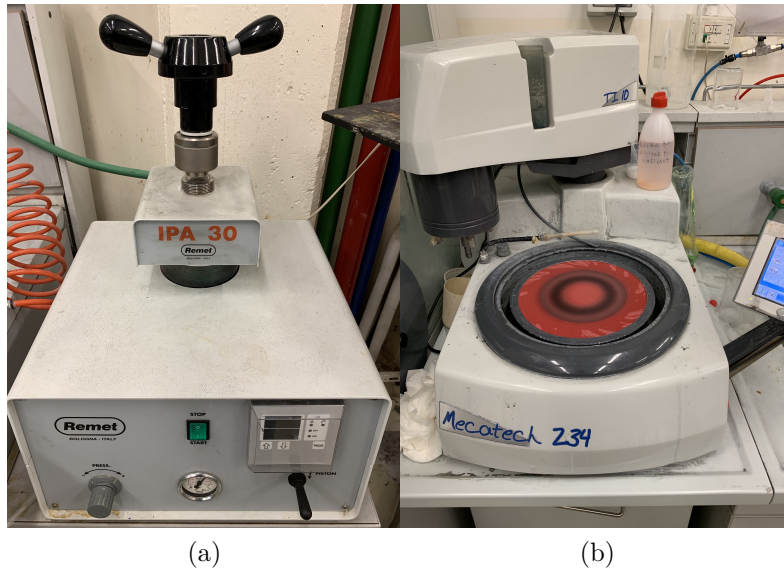


Figure 4.6: Machine used to polish specimens at Politecnico di Torino: (a) Remet mounting press to put together more specimens, in this way was easier to polish them all together and increase the productivity; (b) polishing machine to obtain mirror polished surfaces for the specimens.

through P600 ( $25,8 \mu\text{m}$ ), P800 ( $21,8 \mu\text{m}$ ), P1200 ( $15,3 \mu\text{m}$ ), P2400 ( $8,4 \mu\text{m}$ ), and 4000 ( $5 \mu\text{m}$ ). The polishing operation has been made with a rotating speed of 250 rpm and constant water flow as a lubricant. After the polishing operation with all these abrasive discs, to obtain the polished mirror surface two pans (one in figure 4.6(b)) are used, the first one with a diamond paste of  $3 \mu\text{m}$ , and the second one of  $1 \mu\text{m}$ . In the figures 4.7 the specimens in the resin before and after the polishing operation are represented.

After the polishing operation, it is possible to analyze the porosity of the specimens by using an optical microscope (figure 4.8(a)). The one used for this research is the "LEICA"; it has a manual movement on x-y and an objective with a possible calibration range from 50x to 1000x. To see the porosity, a 100x focus with a dark field was used. It is possible to move on to a specific region manually by the movement of the x-y axis. Adjusting the exposure of the microscope, it is visible just the porosity on the image. Finally, it was used software installed on the laboratory computer to analyze the porosity thanks to an advanced image processing capability (figure 4.8(b)).

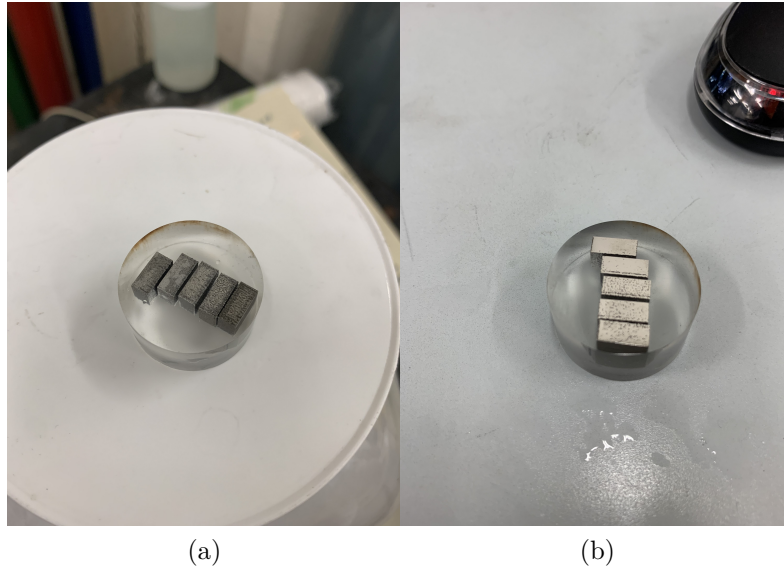


Figure 4.7: Specimens polished: (a) conditions of the specimens before the polishing operation; (b) mirror polished specimens, ready to be analyzed with the optical microscope

## 4.4 DoE 3-Mechanical characteristics

The third DoE aims to study the mechanical characteristics of the best specimens. Since the core parameters are not modified, it is a check, but a significant change in mechanical characteristics is not expected. The only limit that can be negatively affected is the fatigue limit. Still, it should be directly related to the porosity percentage present in the specimens, so if the porosity is not increased too much, it should not decrease. Tensile bars are drawn in Materialise Magics and printed to make the tensile test, measuring the yield and the ultimate tensile strength. The standardized shape is shown in figure 4.9, while its dimensions are reported in table 4.2.

Considering the repeatability test, three tensile bars are printed using the best set of parameters for the angle of  $35^\circ$  and  $40^\circ$ . These have been chosen considering the lowest values of roughness and porosity in the other DoEs. One problem is the bars' dimension, the scale effect is not considered yet, and the uniformed tensile bars dimensions are bigger than the specimens printed up to now. To make a comparison, it is also necessary to print the same tensile bars with the supports. In fact, since printing a tensile bar horizontally or vertically causes different mechanical properties, it would be impossible to compare a  $40^\circ$  or  $35^\circ$  with one printed at a different angulation. Summarizing, for the best set of parameter are printed 6 specimens without support (3 at  $35^\circ$  and 3 at  $40^\circ$ ) and 2 specimens (1 at  $35^\circ$  and 1 at  $40^\circ$ ) with support to compare the results.

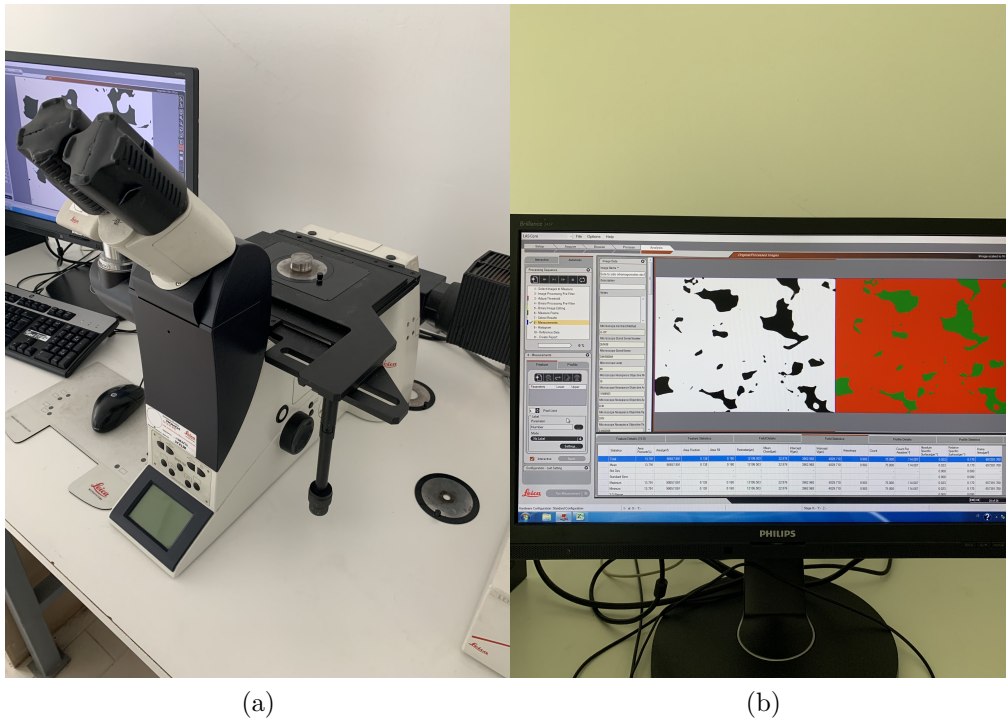


Figure 4.8: Analysis of the porosity: (a) optical microscope used in the laboratory; (b) software used for the analysis of the porosity.

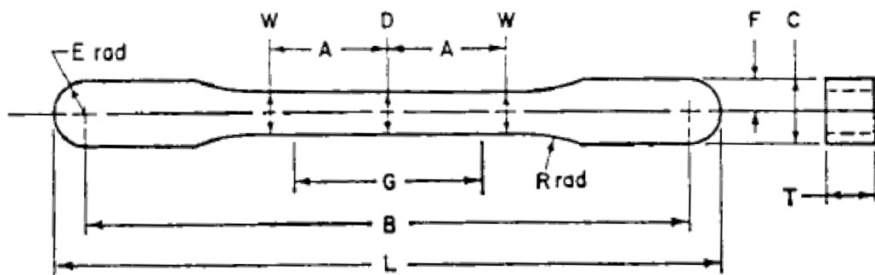


Figure 4.9: Standardized flat shape bar for the tensile stress test

Finally, the specimen are analyzed in the Alessandria detachment of Politecnico di Torino using a Zwisch-Roell BT1-FR100 machine, represented in figure 4.10.

Table 4.2: Standardized dimensions (ASTM E8) for the flat shaped bar represented in figure 4.9

| Dimensions [mm]                    |                  |
|------------------------------------|------------------|
| G-Gage length                      | $25.4 \pm 0.08$  |
| D-Width at center                  | $5.72 \pm 0.03$  |
| W-Width at end of reduced section  | $5.97 \pm 0.03$  |
| T-Compact to this thickness        | 3-56 to 6.35     |
| R-Radius of fillet                 | 25.4             |
| A-Half-length of reduced section   | 15.9             |
| B-Grip length                      | $80.95 \pm 0.03$ |
| L-Overall length                   | $89.64 \pm 0.03$ |
| C-Width of grip section            | $8.71 \pm 0.03$  |
| F-Half-width of grip section       | $4.34 \pm 0.03$  |
| E-End radius                       | $4.34 \pm 0.03$  |
| Pressing area = $645 \text{ mm}^2$ |                  |



Figure 4.10: Zwisch-Roell BT1-FR100 used in Alessandria detachment of Politecnico di Torino

# Chapter 5

## Results and discussion

### 5.1 DoE 1-Roughness evaluation

In table 5.1, the results of the first design of the experiment are reported. Each set of parameters of the  $3^3$  factorial experiment reports the volume energy density, the linear energy density, and the downskin roughness for all the angles. Some of the specimens failed during the printing operation due to delamination. These specimens are highlighted with the scripture "Broken". Other samples had a roughness too high to be measured with the roughness tester (higher than  $35\mu\text{m}$ ); these are reported with "High". The table's roughness values are the average of three different measurements in different locations of the overhang. All the measurements are made parallel to the long edge of the specimens. In green the eight best specimens with roughness values lower than  $21\mu\text{m}$  used in the second DoE are underlined.

In order to analyze the results of the first experiment, data are plotted in graphs. It is interesting to check the influence of the volumetric energy density (VED) and the linear energy density (LED). Since the layer thickness is constant at  $40\mu\text{m}$ , it would be useless to analyze the superficial energy density. The results are represented in figure 5.1 and 5.2.

It is possible to see from graph 5.1 that for both the specimens at  $40^\circ$  and  $35^\circ$ , there is a trend. The roughness increases with the increase of the downskin volume energy density. Generally speaking, this trend was expected. A higher VED increases the heat in the melt pool, and it is challenging to be dissipated without solid support that conducts heat. An increase of heat in the melt pool will cause a deeper penetration and the consequent creation of dross (roughness). However, it is possible to see that the best sets of parameters have different VED: it is possible to identify a generic trend, but each parameter affects the heat production differently. It is necessary to test with the factorial experiment several combinations of power,

Table 5.1: Downskin roughness of the specimens printed in the DoE 1

| Specimen | VED [ $J/mm^3$ ] | LED [ $J/mm^2$ ] | 40° [ $\mu m$ ] | 35° [ $\mu m$ ] | 30° [ $\mu m$ ] |
|----------|------------------|------------------|-----------------|-----------------|-----------------|
| 1        | 16,05            | 0,051            | 18,8            | 19,1            | Broken          |
| 2        | 11,67            | 0,051            | 19,5            | 20,3            | High            |
| 3        | 9,17             | 0,051            | 21,3            | 22,1            | High            |
| 4        | 14,6             | 0,047            | 19,9            | 19,3            | High            |
| 5        | 10,61            | 0,047            | 22,1            | 23,4            | High            |
| 6        | 8,43             | 0,047            | 16,4            | 17,5            | High            |
| 7        | 13,96            | 0,045            | 24,3            | 25,6            | Broken          |
| 8        | 10,14            | 0,045            | 22,5            | 24,4            | Broken          |
| 9        | 7,97             | 0,045            | 22,3            | 23,8            | Broken          |
| 10       | 17,00            | 0,054            | 26,3            | 26,9            | Broken          |
| 11       | 12,36            | 0,054            | 17,1            | 19              | Broken          |
| 12       | 9,71             | 0,054            | 19,3            | 19              | High            |
| 13       | 15,45            | 0,049            | 25,1            | Broken          | Broken          |
| 14       | 11,24            | 0,049            | 22,3            | 24,5            | High            |
| 15       | 8,83             | 0,049            | 18              | 20,3            | High            |
| 16       | 14,78            | 0,047            | 24,3            | 25,6            | Broken          |
| 17       | 10,75            | 0,047            | 21,4            | 22,8            | Broken          |
| 18       | 8,44             | 0,047            | 21,1            | 22,3            | Broken          |
| 19       | 18,90            | 0,060            | 25,3            | 27,3            | Broken          |
| 20       | 13,73            | 0,060            | 20              | 21              | High            |
| 21       | 10,79            | 0,060            | 21,6            | 22,8            | Broken          |
| 22       | 17,16            | 0,055            | 25,3            | 26,2            | Broken          |
| 23       | 12,48            | 0,055            | 21,3            | 23,2            | Broken          |
| 24       | 9,81             | 0,055            | 20,8            | 21,9            | Broken          |
| 25       | 16,42            | 0,053            | 26              | 26,9            | Broken          |
| 26       | 11,94            | 0,053            | 23,4            | 24,1            | Broken          |
| 27       | 9,38             | 0,053            | 21,2            | 22,4            | Broken          |

speed, and hatch distance to see which are the best sets of parameters to decrease the roughness on the downskin surface. A similar comment can be applied to the graph of the roughness with respect to the linear energy density (figure 5.2): it is possible to highlight a generic trend (average mean line) for which the roughness increases with the increase of LED. It is possible to notice that the two lines have different slopes: since the layer thickness is constant, the only modifier between VED (equation (1.3)) and LED (equation (1.4)) is the hatch distance. In this way, it is demonstrated that the hatch distance must be considered for the downskin parameters. The result obtained is following the one of Calignano et al. [13].

It is possible to compare the figures 5.3(a) and 5.3(b): these two both show the dependence of the roughness on the downskin surface in respect to the hatch distance value used. Thanks to the average line, it is possible to see that the slope is different; however, the trend is the same: for an increase of the hatch distance value, the roughness decreases. This trend can be explained because the volume

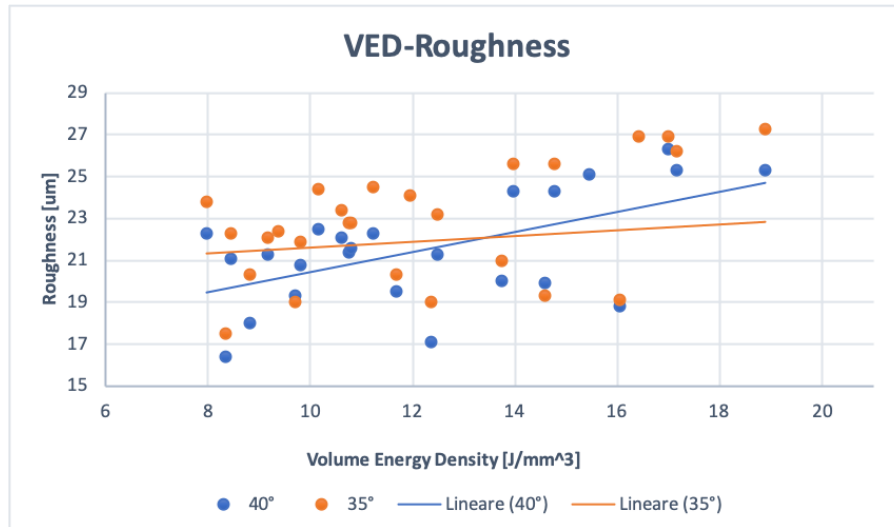


Figure 5.1: Dependence of roughness on the volumetric energy density for the specimens at 40°. The two lines represent the linear average of the measurements.

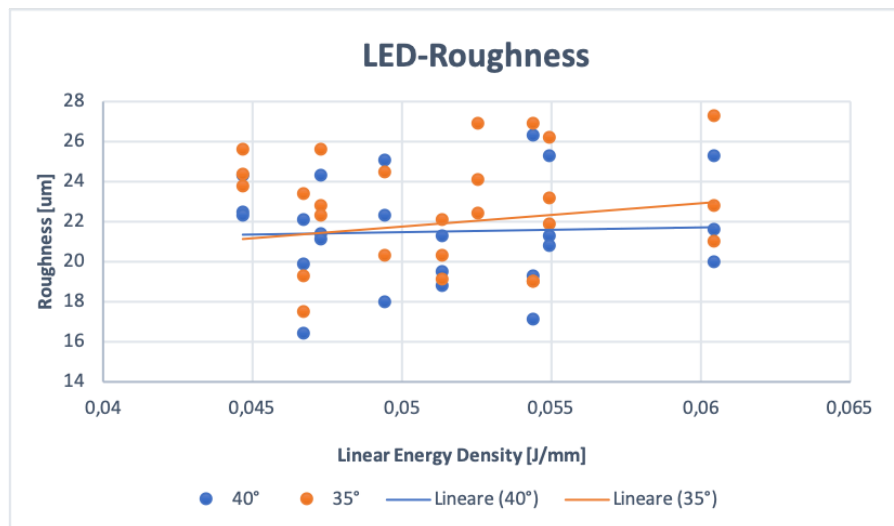


Figure 5.2: Dependence of roughness on the volumetric energy density for the specimens at 35°. The two lines represent the linear average of the measurements.

energy density decreases, and so there is less heat to be dissipated, causing less droplet formation. It is also possible to notice that the average value slope is steeper for the 40° specimens; however, it is important to focus on the roughness values. At 40° the roughness average varies between 23  $\mu\text{m}$  and 19  $\mu\text{m}$ , while for the 35° specimens is higher, oscillating near 22  $\mu\text{m}$  also for the higher hatch values. It was expected to find a higher roughness for specimens with a lower angle since it is more difficult to dissipate heat.

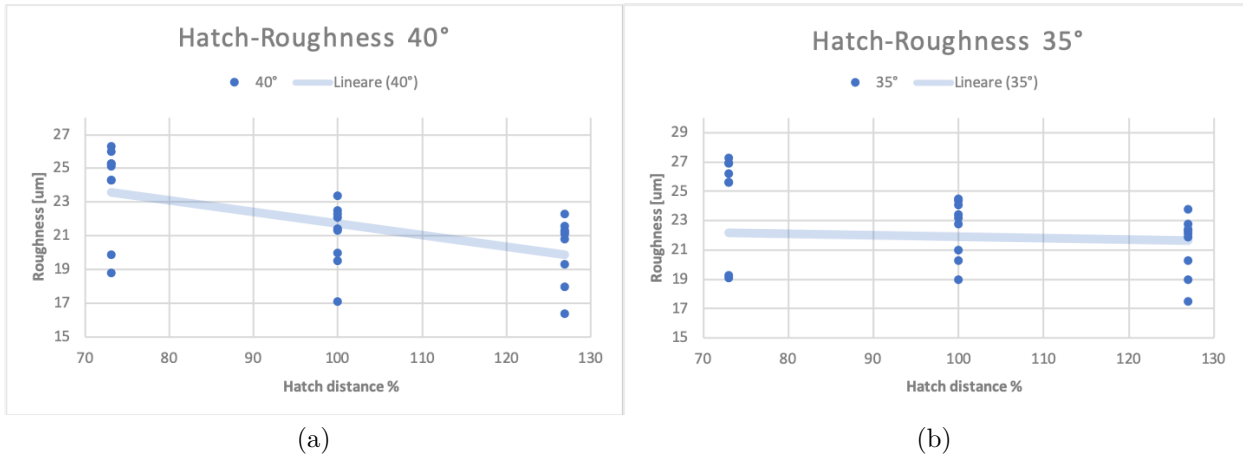


Figure 5.3: Dependence of the roughness with respect to the hatch distance used for the specimens inclined (a) at 40°; (b) at 35°

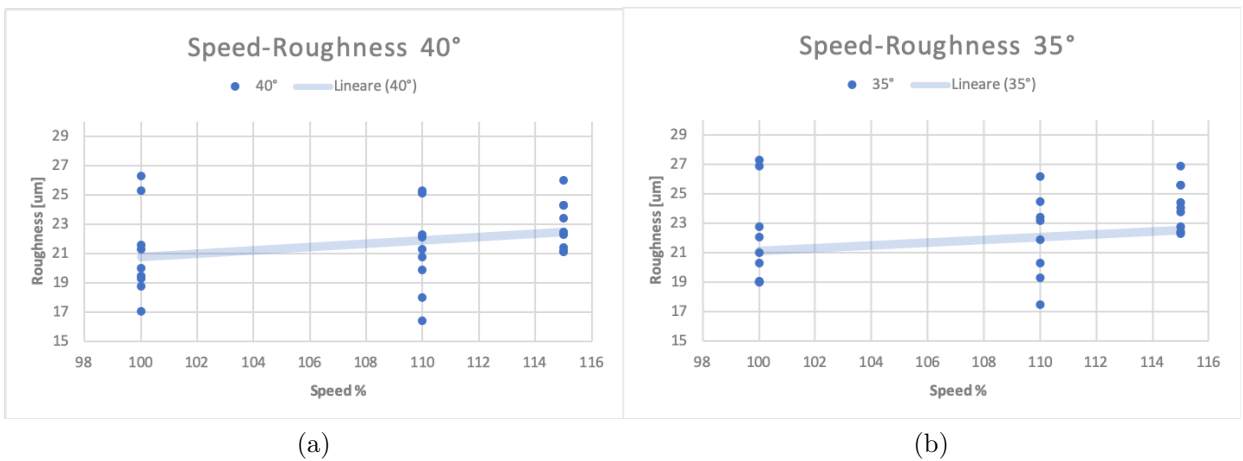


Figure 5.4: Dependence of the roughness with respect to the laser speed in the downskin region used for the specimens inclined (a) at 40°; (b) at 35°

Analyzing the figures 5.4(a) and 5.4(b), it is possible to see that are characterized by the same trend: the roughness increases with the increasing of the speed. Since the speed is at the denominator of the volume energy density equation (1.3), it is expected that the roughness decreases for higher speeds. It is also interesting that out of the eight best sets of parameters, five uses the lowest speed, three the average one, and no one has the highest speed. It is possible to conclude that there is probably a threshold for speed that causes a decrease in downskin surface quality. It is also possible to see that the specimens with 115% of the speed always have roughness above 21  $\mu\text{m}$ , while for the other two speeds values, there are roughness

also at lower levels.

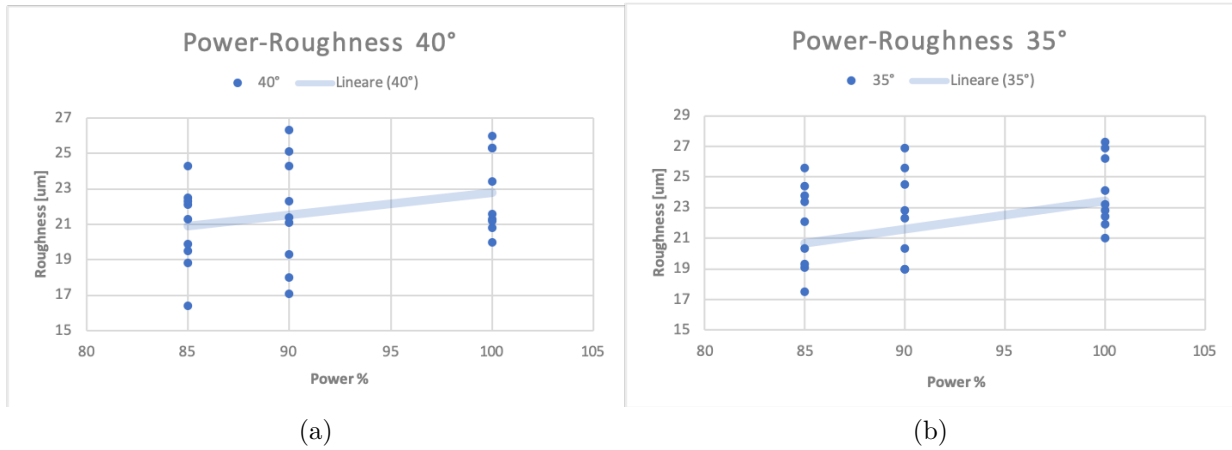


Figure 5.5: Dependence of the roughness with respect to the power speed in the downskin region used for the specimens inclined (a) at 40°; (b) at 35°

Comparing the figures 5.5(a) and 5.5(b), it is possible to see the trend line for which, with increased power, there is an increase of roughness in the downskin surface. It is coherent with the heat quantity: the power speed is at the numerator of the volumetric energy density, and its increase causes a rise of the energy inside the melt pool.

In conclusion, the first design of the experiment analyzed all the possible combinations of the parameters used. It is possible to define a trend for each parameter, and it is usually consistent with the fact that the roughness decrease for lower energy inside the melt pool. Also, for the graphs of the volumetric energy density and the linear energy density, there is a trend for which the roughness increases for lower values. However, each parameter affects the downskin roughness differently. It is necessary to try all the combinations experimentally and check the results. Indeed, the eight best sets of parameters are not the ones with the lowest energy density (volumetric or linear). It is now necessary to check if these results are repeatable or not to check the consistency of what has just been found.

## 5.2 Repeatability

In table 5.2 the results of the repeatability test are represented. Each specimen's roughness value is the average of three measurements in different points of the overhang surface. It is also represented the average value of roughness, evaluated using the values of the repeatability test. In green the three sets of parameters with the lowest roughness are highlighted.

Table 5.2: Repeatability test and average downskin roughness

| Specimen | 40°#1 | 40°#2 | 40°#3 | Average 40° | 35°#1 | 35°#2 | 35°#3 | Average 35° |
|----------|-------|-------|-------|-------------|-------|-------|-------|-------------|
| 1        | 18,8  | 18,3  | 18,7  | 18,7        | 19,1  | 18,4  | 18,8  | 18,8        |
| 2        | 19,5  | 19,6  | 19,1  | 19,4        | 20,3  | 21    | 20,9  | 20,7        |
| 4        | 19,9  | 20,2  | 20,3  | 20,1        | 19,3  | 19,2  | 19,5  | 19,3        |
| 6        | 16,4  | 17    | 16,2  | 16,5        | 17,5  | 16,8  | 17,1  | 17,8        |
| 11       | 17,1  | 16,6  | 16,6  | 16,8        | 19    | 18,5  | 18,9  | 18,8        |
| 12       | 19,3  | 18,5  | 18,5  | 18,8        | 19    | 18,5  | 18,5  | 18,7        |
| 15       | 18    | 17,5  | 18,2  | 17,9        | 20,3  | 20    | 19,9  | 20          |
| 20       | 20    | 19,3  | 19,8  | 19,7        | 21    | 21,7  | 20,8  | 21,2        |

In figure 5.6 is represented the variability obtained from the roughness measurements. The highest variability calculated is within two measurements in the set of parameters six at 35°: the percentage difference between 17.5 and 16.8 is 4.2%.

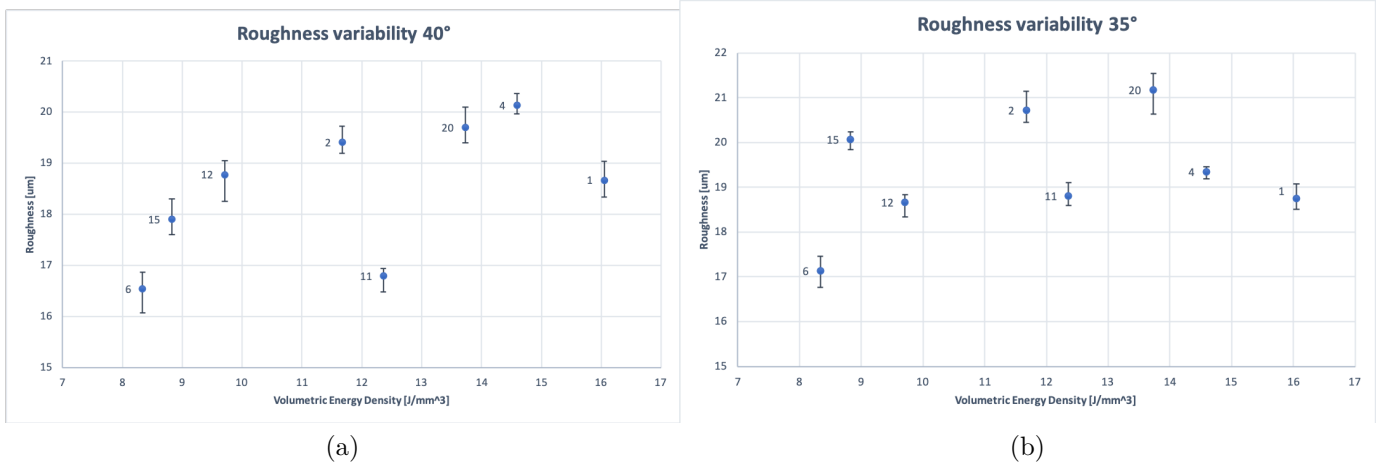


Figure 5.6: Roughness variability obtained in the repeatability test for specimens inclined at (a) 40°; (b) 35°

The results obtained are acceptable since the threshold decided for the experiment was 5%.

The 1-5% of variability can be caused by several factors (parameters, blade wear, variability in flux within the chamber), amongst all the powder quality. The powder

is sieved between two print phases; however, the quality could be slightly lower than the virgin powder.

### 5.3 DoE 2-Porosity

The second DoE consists of the porosity analysis of the best specimens. Results are reported in table 5.3. The porosity value is an average of six measurements made in the downskin region.

Table 5.3: Results from the porosity analysis of the specimens

| Specimen | Average Porosity | Max. Porosity | Min. Porosity | Max. Pore Diameter [ $\mu m$ ] | Average Density |
|----------|------------------|---------------|---------------|--------------------------------|-----------------|
| 1 (40°)  | 0,35             | 0,48          | 0,29          | 22,78                          | 99,65           |
| 2 (40°)  | 0,34             | 0,42          | 0,26          | 44,53                          | 99,66           |
| 4 (40°)  | 0,54             | 0,72          | 0,35          | 45,43                          | 99,46           |
| 6 (40°)  | 0,55             | 0,89          | 0,27          | 20,81                          | 99,45           |
| 11 (40°) | 0,56             | 0,66          | 0,40          | 19,95                          | 99,44           |
| 12 (40°) | 0,45             | 0,50          | 0,35          | 47,21                          | 99,55           |
| 15 (40°) | 0,37             | 0,45          | 0,29          | 13,31                          | 99,63           |
| 20 (40°) | 0,11             | 0,18          | 0,07          | 19,27                          | 99,88           |
| 1 (35°)  | 0,57             | 0,85          | 0,31          | 45,77                          | 99,43           |
| 2 (35°)  | 0,37             | 0,63          | 0,24          | 48,50                          | 99,63           |
| 4 (35°)  | 1,60             | 3,19          | 0,56          | 132,25                         | 98,39           |
| 6 (35°)  | 0,46             | 0,59          | 0,32          | 46,84                          | 99,54           |
| 11 (35°) | 0,43             | 0,54          | 0,31          | 13,71                          | 99,57           |
| 12 (35°) | 0,61             | 1,14          | 0,39          | 17,93                          | 99,39           |
| 15 (35°) | 0,29             | 0,49          | 0,10          | 45,61                          | 99,71           |
| 20 (35°) | 0,17             | 0,42          | 0,02          | 31,58                          | 99,83           |

The results obtained show an average density in the downskin region always higher than 99.39%. Therefore, it is possible to state that downskin parameters are not strongly affecting the porosity. In table 5.3 the minimum and maximum porosity within the six measurements are also reported. Apart from specimens four and twelve inclined at 35°, the variation is small, and also with the maximum porosity, the density is higher than 99%. In figures 5.7 the average porosity for the specimens inclined at 40° and 35° with their variability are represented.

Analyzing the graphs in figures 5.7, it is possible to say that there is not a defined trend of the porosity with respect to the volumetric energy density value. Therefore, it could be interesting to investigate the reasons for the defects. The pores in part can be caused by three different processes [21];[32]. There are three types of pores: lack of fusion, keyhole, and gas pores [48]. The ones caused by the lack of fusion are created when the volumetric energy density is low or if the speed is high. In this case, during the track's solidification, there are pores filled with unmelted powder.

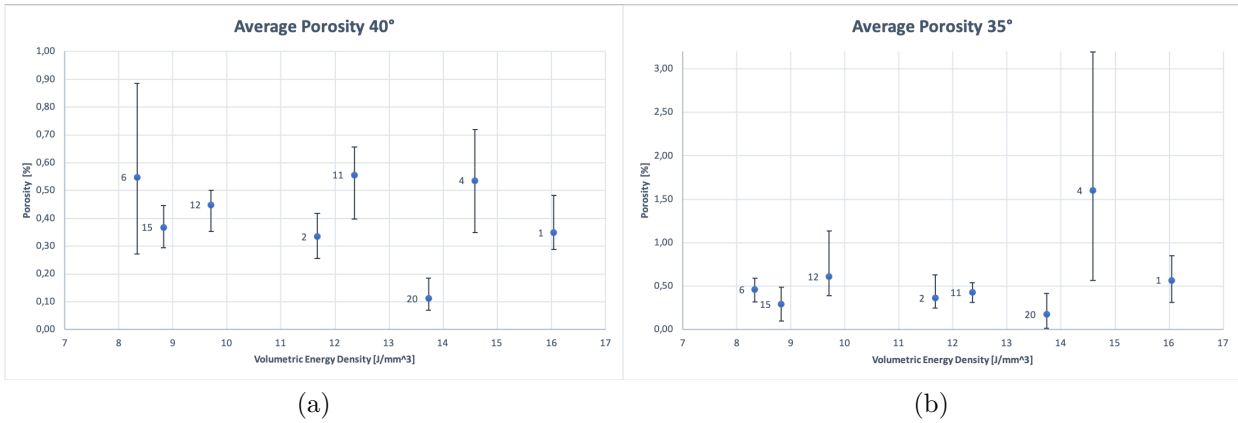


Figure 5.7: Dependence of the porosity with respect to the volumetric energy density used in the downskin region for the inclined specimens (a) at 40°; (b) at 35°

These pores are big and characterized by an irregular shape. The second category is pores formed by the keyhole effect; due to high energy, the melt pool is deep, and some vapor stays trapped in the final part of the hole during the solidification phase. These are relatively large pores with a circular shape on the x-y plane and are elongated on the z dimension. Finally, the gas pores are the most common in metal AM. Are small and circular pores caused by gas trapped during the solidification of the melt pool.

In figure 5.8 are represented the maximum dimension of the equivalent diameter for each specimen analyzed.

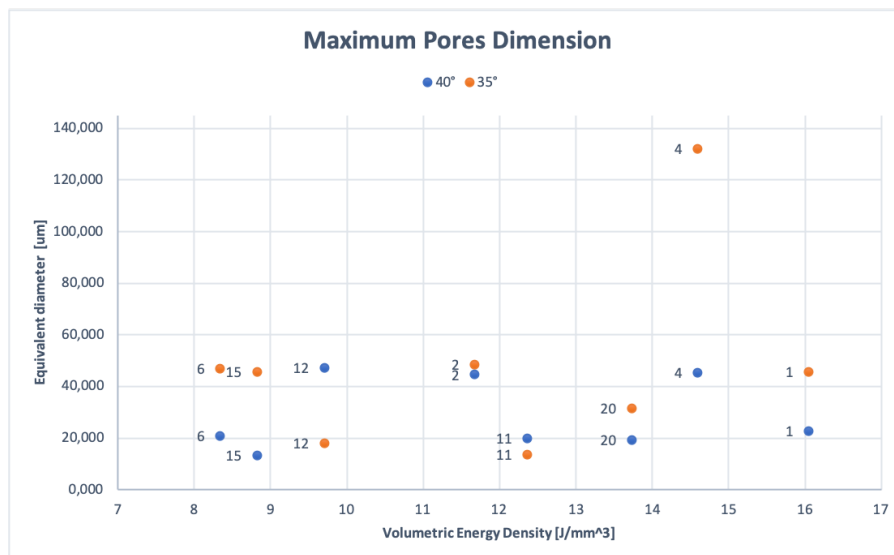


Figure 5.8: Maximum equivalent diameter for each specimen

It is possible to compare the dimension of pores and guess their possible cause. In figure 5.8, it is possible to see that the most significant pore is the one for specimen four inclined at  $35^\circ$ . In figure 5.9 are represented two optical microscope images for the specimens four and six inclined at  $35^\circ$ . In the image 5.9(a), there is a large and irregular shaped pore in the center; a lack of fusion should have caused it. In the second picture 5.9(b), the pores are smaller and with circular shapes, probably created by trapped gas. Considering that in the downskin parameters 70% lower than the core ones are used, it would be difficult to find keyhole pores.

In appendix B all the pictures taken with the optical microscope are represented. In all the figures, the vast majority of the defects are gas pores; sometimes, there are pores caused by lack of fusion. Apart from specimen four inclined at  $35^\circ$ , there are not others with two pictures of the same surface reporting lack of fusion pores. In conclusion, the second experiment found promising results: considering the lowered energy density used for the specimens, a drop in the density was expected. However, the average density of all the specimens (apart from one) is higher than 99.3%. It is a good result for mechanical applications, considering that the tests were done "as-built", with heat treatment, it is possible to reach higher densities. Considering these comments, it has been chosen to define the best three sets of parameters evaluating the roughness's results on the downskin surface uniquely.

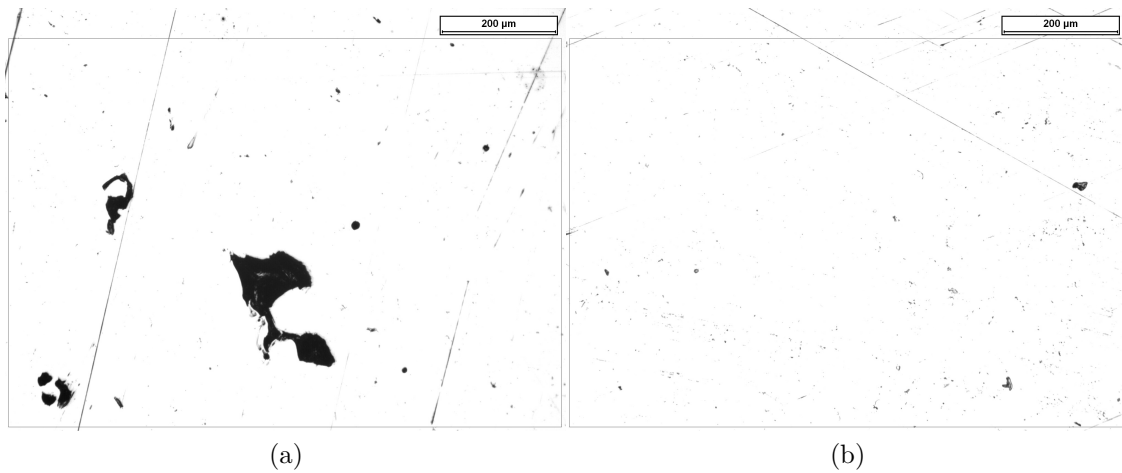


Figure 5.9: Optical microscope images, porosity analysis for the specimens (a) 4 inclined at  $35^\circ$ ; (b) 6 inclined at  $35^\circ$

## **5.4 DoE 3-Mechanical characteristics**

The specimens were printed and showed good results. All of them were not broken. The tensile test should have been performed. Unfortunately, due to a delay caused by COVID19, the specimens are on their way to be tested at the Alessandria department of Politecnico di Torino and the results are not available yet. Considering that the specimens do not show any defect, the porosity is low, and the area affected by the downskin parameter is small, it is not expected a change in the ultimate tensile stress. Once this supposition is validated, the set of parameter can be used to print pieces inclined at  $40^\circ$  or  $35^\circ$  without support.

# Chapter 6

## Conclusion

The results of the thesis highlight the best set of downskin parameter to print overhang surfaces. It is now possible to print these inclined up to 35°-40° without the use of the support structure, keeping low roughness and high density.

### 6.1 Results and highlights

The initial literature analysis found out all the problems related to the downskin. The parameters influencing the most the quality of overhang surfaces were understood: laser power, laser speed, hatch distance, number of layers processed with downskin parameters, and scanning pattern.

The first design of experiment was conducted as a 3<sup>3</sup> factorial test, using three different values of laser power, speed, and hatch distance. The number of layers processed was kept fix at four, while the pattern strategy used was the one optimized by Prima Industrie SpA. Analyzing the results, some trends were highlighted; as expected, the melt pool's quantity of energy directly affects the dross formation. However, since the three parameters affected the roughness differently, it had been necessary to try all the combinations. The roughness of the specimens oscillated within 17 and 29  $\mu m$  for the angles of 35° and 40°. It was impossible to print with an acceptable roughness value for lower angles (e.g. 30°). From the first experiment, the best eight sets of parameters were highlighted. The roughness on the downskin surface was always lower than 21  $\mu m$ .

Subsequently, a repeatability test was performed to check the results' consistency, printing the other two specimens for each best set of downskin parameter. All the results have a variation of a maximum of 5%. Considering the variability caused by several factors in metal Additive Manufacturing (e.g. parameters, blade wear, powder), it is an acceptable result.

The best specimens' porosity analysis consisted of six measurements using an optical microscope on the surface near the downskin surface. For all the specimens, the average density was higher than 99.39%, considered a good result. Therefore, the maximum pore dimension was analyzed to discover the causes. The vast majority of the specimens were found with gas pores (small and with a spherical shape), while in few specimens (e.g. specimen four at 35°) lack of fusion pores have been identified. However, since the average density was high, the parameters were not considered to be modified.

Finally, the tensile test should have been performed. Unfortunately, due to the problem caused by COVID19, the specimens are on their way to be tested at the Alessandria department of Politecnico di Torino, and the results are not available yet. Since the porosity is low and the area affected by the downskin parameter is small, it is not expected a change in the ultimate tensile stress. In conclusion, the set of parameter six was chosen as the best one. This result comes by the lowest roughness, a low error in the repeatability test, and a high density.

## 6.2 Application development

The new downskin parameters widen the range of application development. There are several parts in which the use of support can be complicated. The first possibility is when are required interior features in a piece. Sometimes, it could be necessary to print interior features specified by the customer's necessities in points from which it would be impossible to remove the support. When lightweight is a crucial factor, lattice structures are used. In these applications, it would be impossible to remove supports, but the shape of the lattice structure's cells characterize the mechanical properties. The possibility to print at 35°-40° without supports can revolution the cells. The third one is the support removal, it usually causes a decrease in mechanical properties in its area. For application with the necessity of critical characteristics in these regions, it should be better to print without support and post-process. Possible applications are rotors and turbines: the angle of the blade change with its evolution, it is defined by design and cannot be modified, and the quality of the surface is a critical parameter for its work performance.

It must also be specified the benefits gained by the optimization of the downskin parameters. Mainly the saving of material and time. The supports are made from the same material as the piece; avoiding printing them helps decrease the waste of material. Similarly, if the supports are no more needed, there is a good percentage of print time saved. However, time saved is also related to the time needed by supports' generation, removal time, and post-processing time (with a downskin roughness of 17  $\mu m$  it could be avoided, depending on the performance required). The decrease in time and material causes money savings.

## 6.3 Future works

There are few papers in the literature regarding downskin and overhang surfaces. Since it is a new application study, it is possible to carry on several kinds of research.

It could be possible to create a generalized method to optimize downskin parameters starting from this thesis. It must be generic since the parameters used are strictly dependent on the material. For example, the  $AlSi_{10}Mg$  is a reflective material, and it needs higher volumetric energy density, so a higher power and a slower speed.

The same parameters should also be tested for different layer thicknesses: the optimized one is valid for  $40\ \mu m$ ; however, it must be checked how it will perform at  $20\ \mu m$ . Hopefully, it would be possible to find an equation to link how the layer thickness variation influences the melt pool's required depth and the parameters of the volumetric energy density.

Due to the long time needed to repeat all the print processes, the scanning strategies were not considered in this thesis. However, to achieve a complete overview, it would be interesting to test different of them since they influence the surface's heat distribution.

Finally, from the company's point of view, the set of parameters found must also be tested with other producers' powders since it could introduce discrepancies.



# Bibliography

- [1] A. Saboori A. Salmi, P. Minetola. *Notes of the course: Additive Manufacturing Systems and materials - Additive Manufacturing processes for metals*. Politecnico di Torino, 2019/2020.
- [2] General Electric Additive. Characterization of nickel alloy 718. <https://www.ge.com/additive/powders-overview>. [online; accessed 6-October-2020].
- [3] Additively. overview over 3d printing technologies. <https://www.additively.com/en/learn-about/3d-printing-technologies>. [online; accessed 26-May-2020].
- [4] KN Amato, SM Gaytan, LE Murr, E Martinez, PW Shindo, J Hernandez, S Collins, and F Medina. Microstructures and mechanical behavior of inconel 718 fabricated by selective laser melting. *Acta Materialia*, 60(5):2229–2239, 2012.
- [5] Donald R Askeland, Pradeep Prabhakar Phulé, Wendelin J Wright, and DK Bhattacharya. *The science and engineering of materials*. Cengage learning, sixth edition, 2010.
- [6] ISO Astm. Astm52900-15 standard terminology for additive manufacturing—general principles—terminology. *ASTM International, West Conshohocken, PA*, 3(4):5, 2015.
- [7] Moataz M Attallah, Rachel Jennings, Xiqian Wang, and Luke N Carter. Additive manufacturing of ni-based superalloys: The outstanding issues. *MRS Bulletin*, 41(10):758–764, 2016.
- [8] Elena Bassoli, Antonella Sola, Mattia Celesti, Sandro Calcagnile, and Carlo Cavallini. Development of laser-based powder bed fusion process parameters and scanning strategy for new metal alloy grades: a holistic method formulation. *Materials*, 11(12):2356, 2018.
- [9] Umberto Scipioni Bertoli, Alexander J Wolfer, Manyalibo J Matthews, Jean-Pierre R Delplanque, and Julie M Schoenung. On the limitations of volumetric energy density as a design parameter for selective laser melting. *Materials & Design*, 113:331–340, 2017.
- [10] Sara Biamino and Saverio Tremamunno. Studio dei trattamenti termici sulla lega di inconel 625 prodotta per selective laser melting. 2018.

- [11] F Calignano. Design optimization of supports for overhanging structures in aluminum and titanium alloys by selective laser melting. *Materials & Design*, 64:203–213, 2014.
- [12] F Calignano, G Cattano, and D Manfredi. Manufacturing of thin wall structures in alsil0mg alloy by laser powder bed fusion through process parameters. *Journal of Materials Processing Technology*, 255:773–783, 2018.
- [13] Flaviana Calignano and Paolo Minetola. Influence of process parameters on the porosity, accuracy, roughness, and support structures of hastelloy x produced by laser powder bed fusion. *Materials*, 12:3178, 09 2019.
- [14] Ernesto E Covarrubias and Mohsen Eshraghi. Effect of build angle on surface properties of nickel superalloys processed by selective laser melting. *Jom*, 70(3):336–342, 2018.
- [15] Wang Di, Yang Yongqiang, Su Xubin, and Chen Yonghua. Study on energy input and its influences on single-track, multi-track, and multi-layer in slm. *The International Journal of Advanced Manufacturing Technology*, 58(9-12):1189–1199, 2012.
- [16] Mohammad H Farshidianfar, Amir Khajepour, and Adrian P Gerlich. Effect of real-time cooling rate on microstructure in laser additive manufacturing. *Journal of Materials Processing Technology*, 231:468–478, 2016.
- [17] Jason C Fox, Shawn P Moylan, and Brandon M Lane. Effect of process parameters on the surface roughness of overhanging structures in laser powder bed fusion additive manufacturing. *Procedia Cirp*, 45:131–134, 2016.
- [18] Thomas G Gallmeyer, Senthamaruvi Moorthy, Branden B Kappes, Michael J Mills, Behnam Amin-Ahmadi, and Aaron P Stebner. Knowledge of process-structure-property relationships to engineer better heat treatments for laser powder bed fusion additive manufactured inconel 718. *Additive Manufacturing*, 31:100977, 2020.
- [19] SM Gaytan, LE Murr, E Martinez, JL Martinez, BI Machado, DA Ramirez, F Medina, S Collins, and RB Wicker. Comparison of microstructures and mechanical properties for solid cobalt-base alloy components and biomedical implant prototypes fabricated by electron beam melting. In *Proceedings of Solid Freeform Fabrication (SFF) Symposium, Austin, TX, USA*, 2010.
- [20] Ian Gibson, David W Rosen, Brent Stucker, et al. *Additive manufacturing technologies*, volume 17. Springer, 2014.
- [21] Haijun Gong, Hengfeng Gu, Kai Zeng, JJS Dilip, Deepankar Pal, Brent Stucker, Daniel Christiansen, Jack Beuth, and John J Lewandowski. Melt pool characterization for selective laser melting of ti-6al-4v pre-alloyed powder. In *Solid freeform fabrication symposium*, pages 256–267, 2014.
- [22] Valeriya Griffiths, James P Scanlan, Murat H Eres, Antonio Martinez-Sykora, and Phani Chinchapatnam. Cost-driven build orientation and bin packing of parts in selective laser melting (slm). *European Journal of Operational Research*, 273(1):334–352, 2019.

- [23] Oerlikon Group. Am metal powder characterization. <https://www.oerlikon.com/am/en/offerings/metal-powders/>. [online; accessed 3-July-2020].
- [24] Dong Dong Gu, Wilhelm Meiners, Konrad Wissenbach, and Reinhart Poprawe. Laser additive manufacturing of metallic components: materials, processes and mechanisms. *International materials reviews*, 57(3):133–164, 2012.
- [25] Dongdong Gu and Yifu Shen. Balling phenomena in direct laser sintering of stainless steel powder: Metallurgical mechanisms and control methods. *Materials & Design*, 30(8):2903–2910, 2009.
- [26] ASTM International. F2792-12a-standard terminology for additive manufacturing technologies. *Rapid Manufacturing Association*, 12:10–12, 2013.
- [27] Luca Iuliano, Federica Bondioli, Abdollah Saboori, Paolo Calefati, and Guido Barale. Characterization of inconel 718 fabricated by selective laser melting (slm) to achieve more productive parameters. 2019.
- [28] Galina Kasperovich and Joachim Hausmann. Improvement of fatigue resistance and ductility of tial6v4 processed by selective laser melting. *Journal of Materials Processing Technology*, 220:202–214, 2015.
- [29] Karolien Kempen, Lore Thijs, Jan Van Humbeeck, and J-P Kruth. Mechanical properties of als10mg produced by selective laser melting. *Physics Procedia*, 39:439–446, 2012.
- [30] HM Khan, MH Dirikolu, and E Koç. Parameters optimization for horizontally built circular profiles: Numerical and experimental investigation. *Optik*, 174:521–529, 2018.
- [31] HM Khan, MH Dirikolu, E Koç, and ZC Oter. Numerical investigation of heat current study across different platforms in slm processed multi-layer als10mg. *Optik*, 170:82–89, 2018.
- [32] Wayne E King, Holly D Barth, Victor M Castillo, Gilbert F Gallegos, John W Gibbs, Douglas E Hahn, Chandrika Kamath, and Alexander M Rubenchik. Observation of keyhole-mode laser melting in laser powder-bed fusion additive manufacturing. *Journal of Materials Processing Technology*, 214(12):2915–2925, 2014.
- [33] Carolin Körner, Elham Attar, and Peter Heinl. Mesoscopic simulation of selective beam melting processes. *Journal of Materials Processing Technology*, 211(6):978–987, 2011.
- [34] Carolin Körner, Andreas Bauereiß, and Elham Attar. Fundamental consolidation mechanisms during selective beam melting of powders. *Modelling and Simulation in Materials Science and Engineering*, 21(8):085011, 2013.
- [35] Jean-Pierre Kruth, Ludo Froyen, Jonas Van Vaerenbergh, Peter Mercelis, Marleen Rombouts, and Bert Lauwers. Selective laser melting of iron-based powder. *Journal of materials processing technology*, 149(1-3):616–622, 2004.
- [36] Martin Leary, Luigi Merli, Federico Torti, Maciej Mazur, and Milan Brandt. Optimal topology for additive manufacture: A method for enabling additive

- manufacture of support-free optimal structures. *Materials & Design*, 63:678–690, 2014.
- [37] Harlal Singh Mali and Deepak Rajendra Unune. Machinability of nickel-based superalloys: An overview. 2017.
- [38] Diego Manfredi, Flaviana Calignano, Manickavasagam Krishnan, Riccardo Canali, Elisa Paola Ambrosio, and Eleonora Atzeni. From powders to dense metal parts: Characterization of a commercial alsiing alloy processed through direct metal laser sintering. *Materials*, 6(3):856–869, 2013.
- [39] M. Matsumoto, M. Shiomi, K. Osakada, and F. Abe. Finite element analysis of single layer forming on metallic powder bed in rapid prototyping by selective laser processing. *International Journal of Machine Tools and Manufacture*, 42:61–67, 01 2002.
- [40] T Matsuo, M Ueki, M Takeyama, and R Tanaka. Strengthening of nickel-base superalloys for nuclear heat exchanger application. *Journal of materials science*, 22(6):1901–1907, 1987.
- [41] John O Milewski. Additive manufacturing of metals. *From Fundamental Technology to Rocket Nozzles, Medical Implants, and Custom Jewelry*,, pages 130–157, 2017.
- [42] KC Mills, BJ Keene, RF Brooks, and A Shirali. Marangoni effects in welding. *Philosophical Transactions of the Royal Society of London. Series A: Mathematical, Physical and Engineering Sciences*, 356(1739):911–925, 1998.
- [43] F Neugebauer, N Keller, V Ploshikhin, F Feuerhahn, and H Köhler. Multi scale fem simulation for distortion calculation in additive manufacturing of hardening stainless steel. In *International Workshop on Thermal Forming and Welding Distortion, Bremen, Germany*, 2014.
- [44] Christ P Paul, P Ganesh, SK Mishra, P Bhargava, JA Negi, and AK Nath. Investigating laser rapid manufacturing for inconel-625 components. *Optics & Laser Technology*, 39(4):800–805, 2007.
- [45] M Nageswara Rao. Application of superalloys in petrochemical and marine sectors in india. *Transactions of the Indian Institute of Metals*, 61(2-3):87–91, 2008.
- [46] Sagar Sarkar, Ankit Porwal, Nuthalapati Yaswanth, and Ashish Kumar Nath. A study on effect of different process parameters on the quality of overhang surface produced by selective laser melting. In *ASME 2018 13th International Manufacturing Science and Engineering Conference*. American Society of Mechanical Engineers Digital Collection, 2018.
- [47] RJ Smith, GJ Lewi, and DH Yates. Development and application of nickel alloys in aerospace engineering. *Aircraft engineering and aerospace technology*, 2001.
- [48] Robert Snell, Sam Tammam-Williams, Lova Chechik, Alistair Lyle, Everth Hernández-Nava, Charlotte Boig, George Panoutsos, and Iain Todd. Methods

- for rapid pore classification in metal additive manufacturing. *JOM*, 72(1):101–109, 2020.
- [49] Jeffrey W Sowards and Jeremy Caron. Weldability of nickel-base alloys. *Comprehensive Material Processing Technology*, 6(Comprehensive Material Processing Technology), 2014.
- [50] Giorgio Strano, L Hao, RM Everson, and KE Evans. A new approach to the design and optimisation of support structures in additive manufacturing. *The International Journal of Advanced Manufacturing Technology*, 66(9-12):1247–1254, 2013.
- [51] Daniel Thomas. *The development of design rules for selective laser melting*. PhD thesis, University of Wales, 2009.
- [52] Nikolay K Tolochko, Sergei E Mozzharov, Igor A Yadroitsev, Tahar Laoui, Ludo Froyen, Victor I Titov, and Michail B Ignatiev. Balling processes during selective laser treatment of powders. *Rapid Prototyping Journal*, 2004.
- [53] Loughborough University. Additive manufacturing research group. <https://www.lboro.ac.uk/research/amrg/about/the7categoriesofadditivemanufacturing/directedenergydeposition/>. [online; accessed 26-May-2020].
- [54] Ben Vandenbroucke and Jean-Pierre Kruth. Selective laser melting of biocompatible metals for rapid manufacturing of medical parts. *Rapid Prototyping Journal*, 2007.
- [55] Benjamin Vayre, Frédéric Vignat, and François Villeneuve. Designing for additive manufacturing. *Procedia CIRP*, 3:632–637, 2012.
- [56] Frederik Verhaeghe, Tom Craeghs, Jeroen Heulens, and Lieven Pandelaers. A pragmatic model for selective laser melting with evaporation. *Acta Materialia*, 57(20):6006–6012, 2009.
- [57] Bey Vrancken, Lore Thijs, Jean-Pierre Kruth, and Jan Van Humbeeck. Heat treatment of ti6al4v produced by selective laser melting: Microstructure and mechanical properties. *Journal of Alloys and Compounds*, 541:177–185, 2012.
- [58] Di Wang, Yongqiang Yang, Ziheng Yi, and Xubin Su. Research on the fabricating quality optimization of the overhanging surface in slm process. *The International Journal of Advanced Manufacturing Technology*, 65(9-12):1471–1484, 2013.
- [59] Di Wang, Yongqiang Yang, Manhui Zhang, Jianbin Lu, Ruicheng Liu, and Dongming Xiao. Study on slm fabrication of precision metal parts with overhanging structures. In *2013 IEEE International Symposium on Assembly and Manufacturing (ISAM)*, pages 222–225. IEEE, 2013.
- [60] Fude Wang. Mechanical property study on rapid additive layer manufacture hastelloy® x alloy by selective laser melting technology. *The International Journal of Advanced Manufacturing Technology*, 58(5-8):545–551, 2012.
- [61] Zemin Wang, Kai Guan, Ming Gao, Xiangyou Li, Xiaofeng Chen, and Xiaoyan Zeng. The microstructure and mechanical properties of deposited-in718 by

- selective laser melting. *Journal of alloys and compounds*, 513:518–523, 2012.
- [62] JH Weber. Nickel-based superalloys: An overview. 2001.
- [63] Prima Industrie SpA website. Print sharp 250 specifications. <https://www.primaadditive.com/print-sharp-250/#1448982544031-64361658-438afc72-a00fae4f-fbacb154-8605>. [online; accessed 13-November-2020].
- [64] I Yadroitsev, Ph Bertrand, and I Smurov. Parametric analysis of the selective laser melting process. *Applied surface science*, 253(19):8064–8069, 2007.
- [65] I Yadroitsev, M Pavlov, Ph Bertrand, and I Smurov. Mechanical properties of samples fabricated by selective laser melting. *14èmes Assises Européennes du Prototypage & Fabrication Rapide*, 2009.
- [66] Li Yang, Keng Hsu, Brian Baughman, Donald Godfrey, Francisco Medina, Mamballykalathil Menon, and Soeren Wiener. *Additive manufacturing of metals: the technology, materials, design and production*. Springer, 2017.
- [67] Xiaoming Zhao, Xin Lin, Jing Chen, Lei Xue, and Weidong Huang. The effect of hot isostatic pressing on crack healing, microstructure, mechanical properties of rene88dt superalloy prepared by laser solid forming. *Materials Science and Engineering: A*, 504(1-2):129–134, 2009.

# Appendix A

## Print Sharp 250

In this appendix the characteristics of the Print Sharp 250, the machine used in Prima Industrie SpA for the thesis, are represented. It is the medium volume machine of Prima Additive, developed for industrial production. As reported in the website brochure [63]: "Print Sharp 250 is a competitive solution to guarantee reliability and quality of your printed components in your chosen materials. Equipped with easy to use control software, a fiber laser, a recirculating system, and a modular scanning system, the machine can meet the customer-specific needs". In table A.1 all the specifications for the machine (size, power, and laser), the process specifications (such as the dimension of the building volume, layer thickness, temperature of the heating platform), and the software used are reported.

Table A.1: Print Sharp 250 and process specifications [63]

| <b>Size &amp; Power</b>                   |   |
|---|---|
| Dimension (L x W x H)                     | 1300 (L) – 110 (W) – 1900 (H)                   |
| Weight                                    | 1400kg  |
| Power Supply                              | 380 V / 50 Hz / 8 kW                            |
| <b>Laser</b>                              |   |
| Type of Laser                             | Yb (Ytterbium) Fiber laser                      |
| Laser Power                               | 200 W / 500 W (Optional)                        |
| Laser Focus Diameter                      | 70 – 100 $\mu$ m                                |
| Beam Wavelength                           | 1060 – 1080 nm                                  |
| <b>Machine and process specifications</b> |   |
| Building Volume                           | 250 x 250 x 300                                 |
| Beam Deflection Speed                     | 8 m/s   |
| Positioning Speed                         | 10 m/s  |
| Build Rate                                | 12 – 30 ( <i>cm</i> ) <sup>3</sup> /h           |
| Layer Thickness                           | 0.02 mm – 0.1mm                                 |
| Layer Width                               | 0.1 mm (single line width)                      |
| Recoater Specifications                   | Travel: 380 mm / Speed: max 500 mm/s            |
| Building Platform Z-axis                  | Travel: 300mm / Speed: max 6 mm/s / Res:0.01 mm |
| Heating Platform                          | Up to 200°C                                     |
| Monitoring Of O <sub>2</sub> Level        | Below 100 ppm (0,01%)                           |
| Permissible Room Temperatures             | 15 – 30°C                                       |
| <b>Auxiliaries &amp; Software</b>         |   |
| Gas (Consumption & running/filling)       | 7 L/min (running)                               |
| System Fill Consumption                   | 50 L  |
| Cam Software                              | Materialise Magics                              |
| Control & Other Software                  | E-plus control software (EPC)                   |
| Industrial Interfaces                     | Ethernet  |

## Appendix B

# Porosity analysis images

This appendix shows all the images taken with the optical microscope. The analysis has been performed for sixteen specimens: the best eight sets of parameters at  $35^\circ$  and  $40^\circ$ . Due to a problem with the mounting press, the resin did not melt completely, and during the polishing operation, it caused some scratches. These are not influencing the porosity analysis by the software.

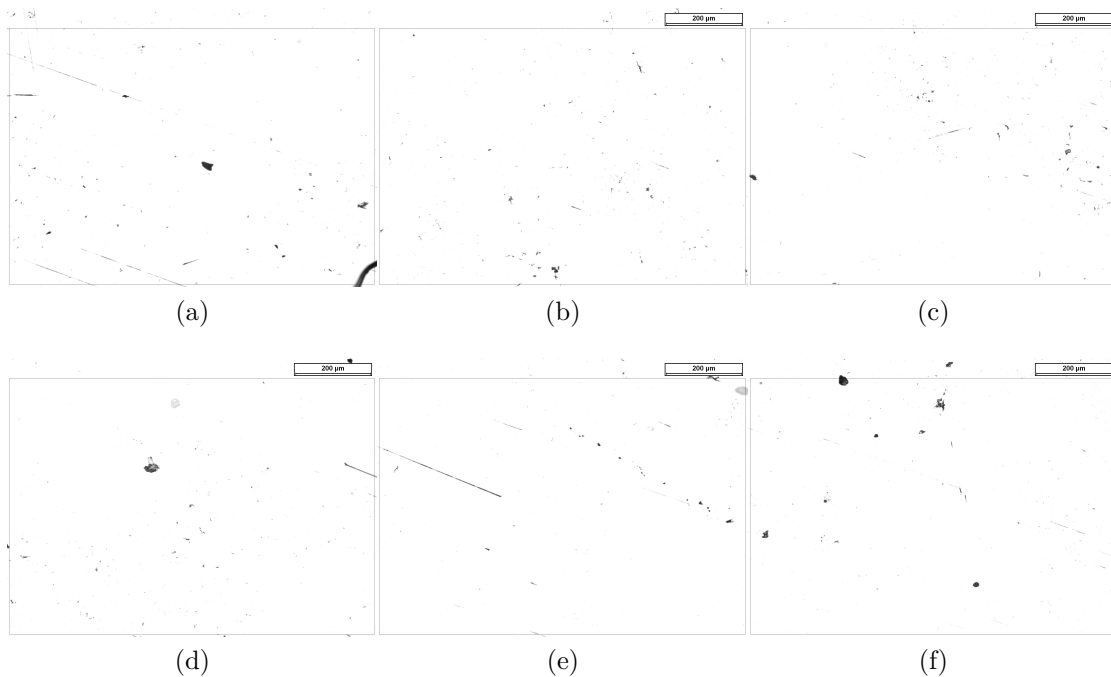


Figure B.1: Optical microscope analysis images for the specimen 1 inclined at  $40^\circ$  in six different points of the downskin region.

Porosity analysis images

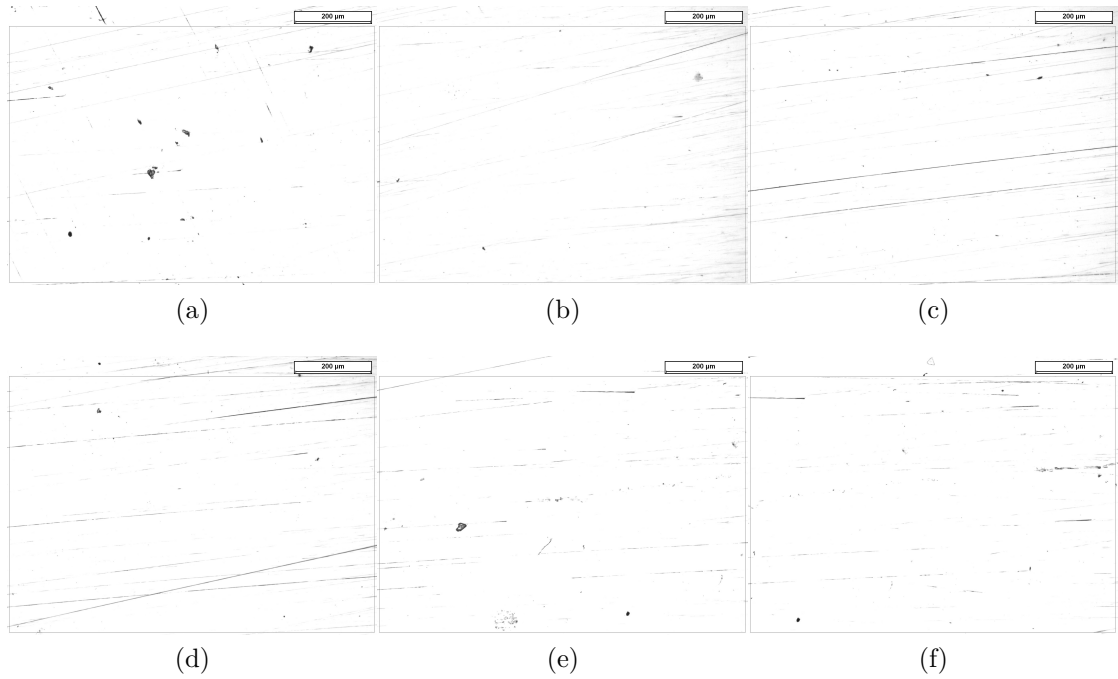


Figure B.2: Optical microscope analysis images for the specimen 2 inclined at  $40^\circ$  in six different points of the downskin region.

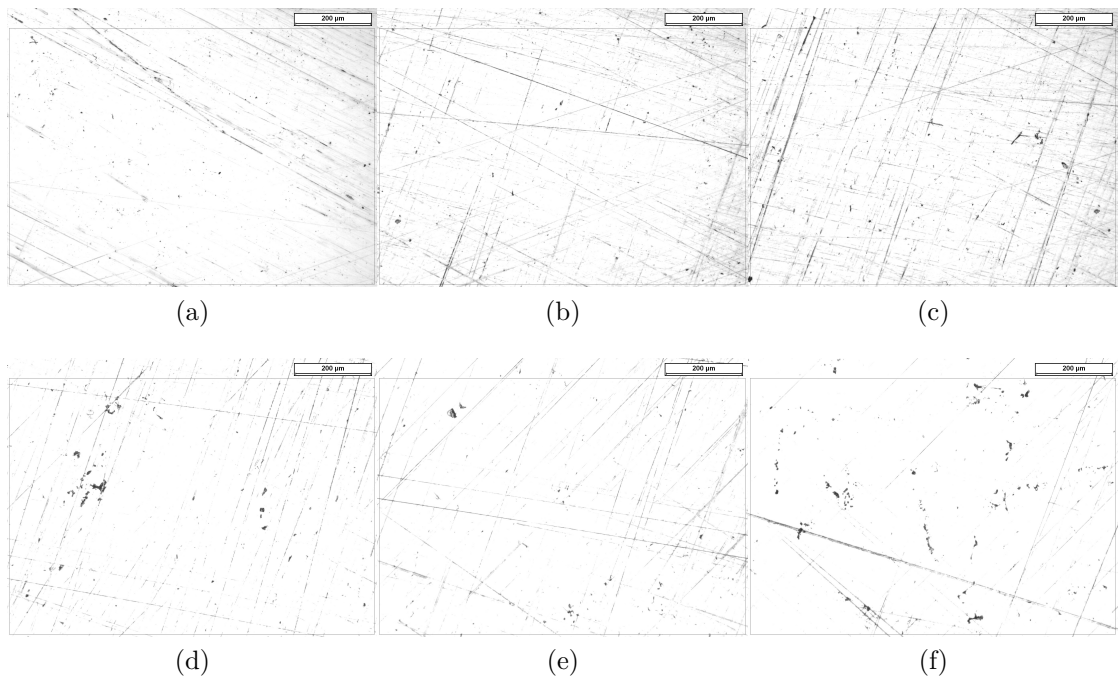


Figure B.3: Optical microscope analysis images for the specimen 4 inclined at  $40^\circ$  in six different points of the downskin region.

Porosity analysis images

---

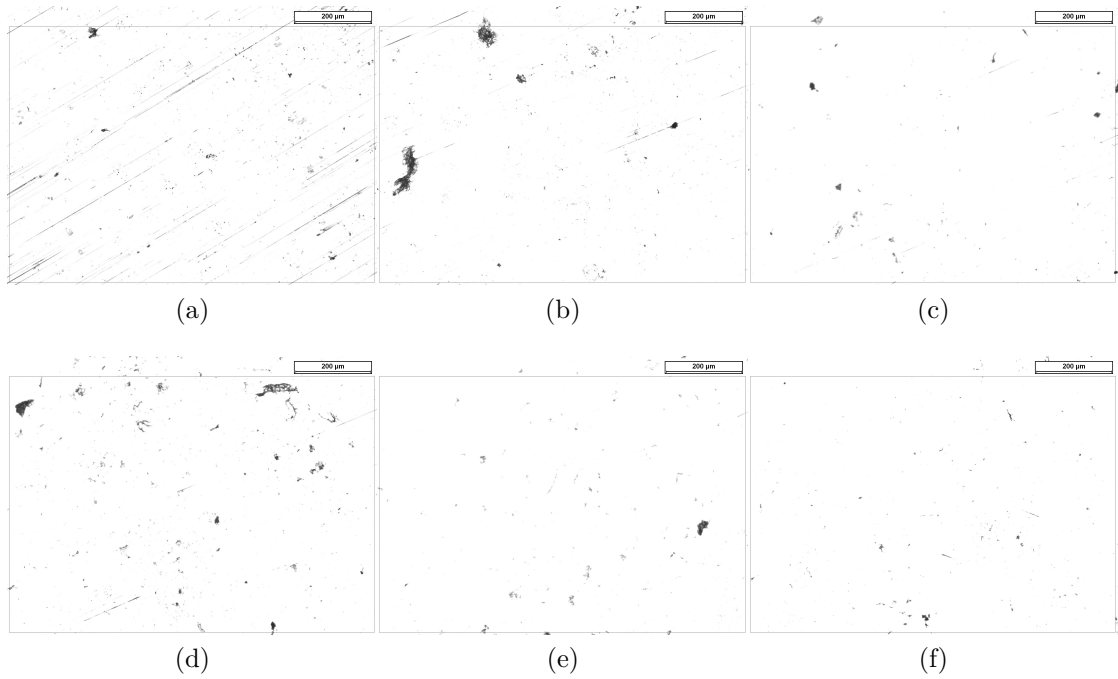


Figure B.4: Optical microscope analysis images for the specimen 6 inclined at  $40^\circ$  in six different points of the downskin region.

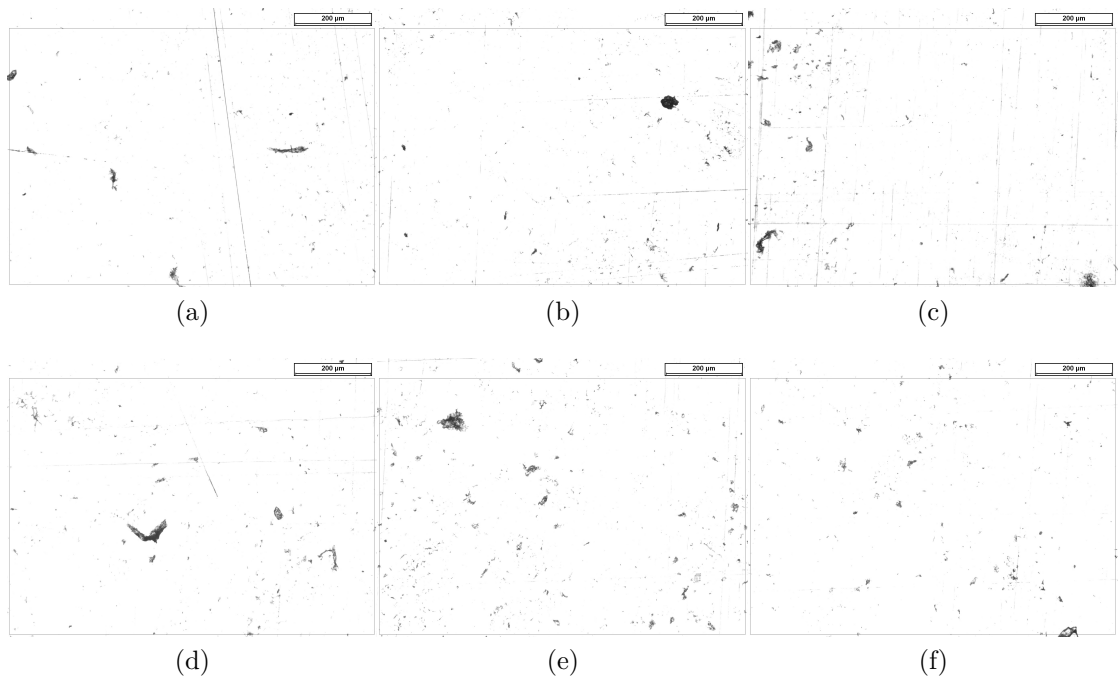


Figure B.5: Optical microscope analysis images for the specimen 11 inclined at  $40^\circ$  in six different points of the downskin region.

Porosity analysis images

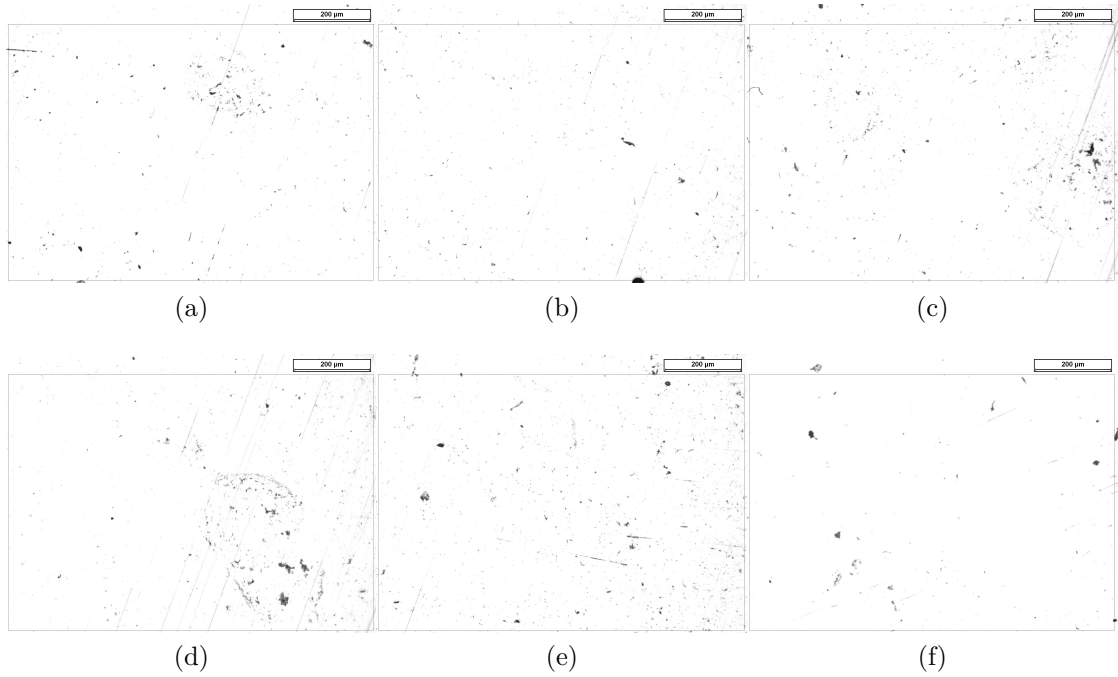


Figure B.6: Optical microscope analysis images for the specimen 12 inclined at  $40^\circ$  in six different points of the downskin region.

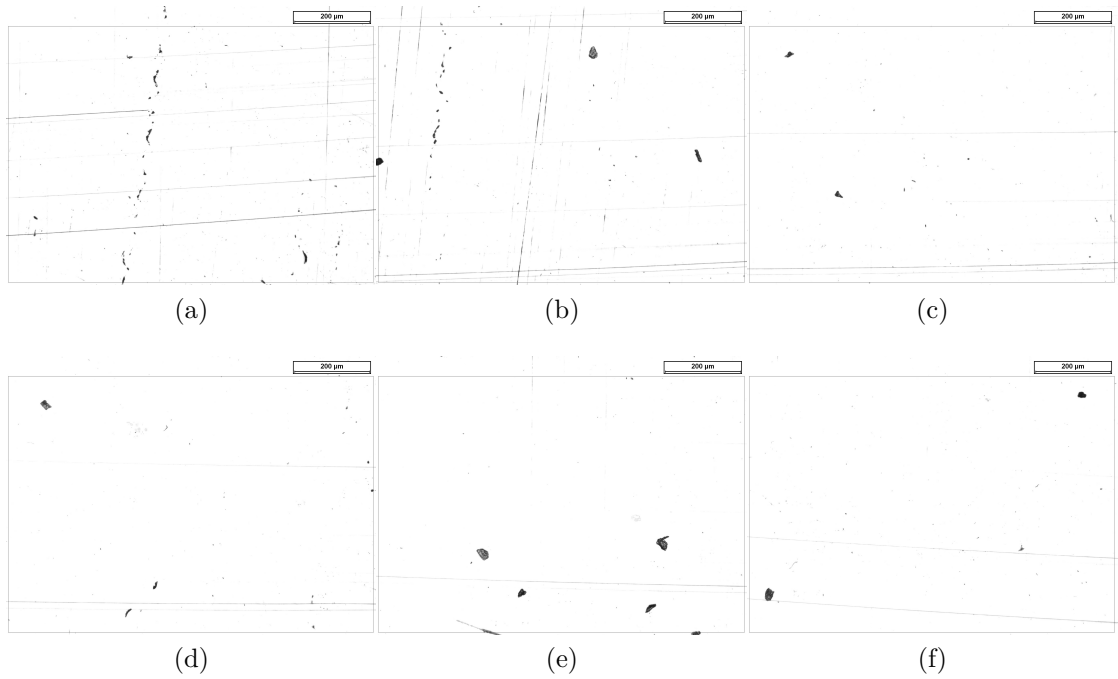


Figure B.7: Optical microscope analysis images for the specimen 15 inclined at  $40^\circ$  in six different points of the downskin region.

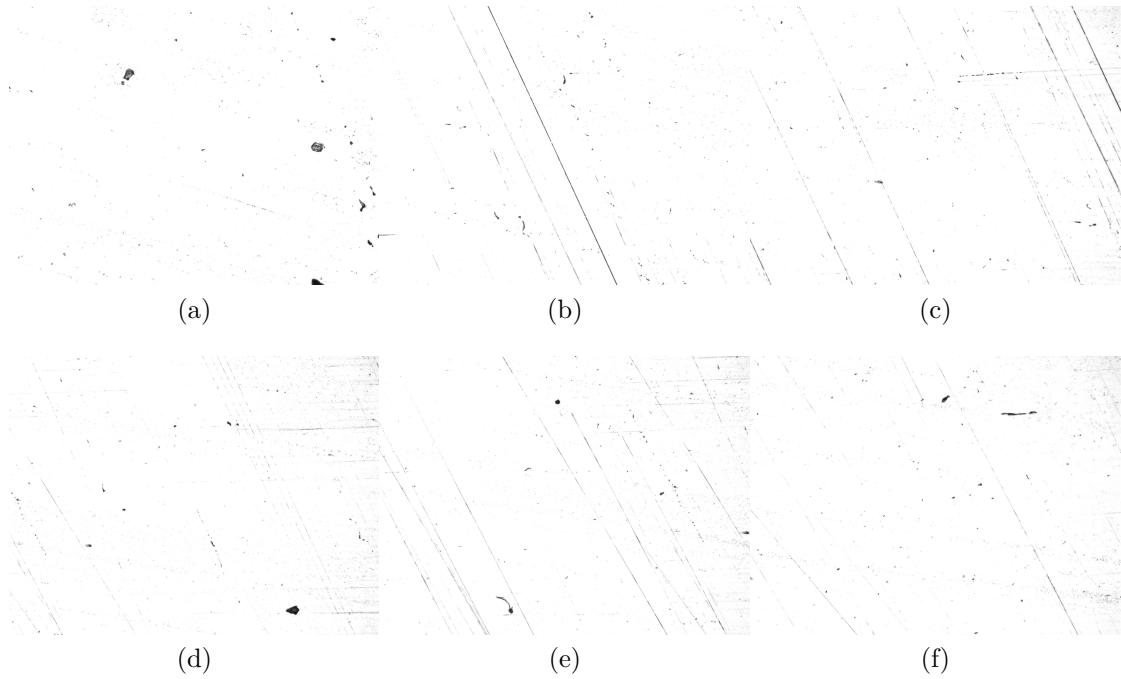


Figure B.8: Optical microscope analysis images for the specimen 20 inclined at  $40^\circ$  in six different points of the downskin region.

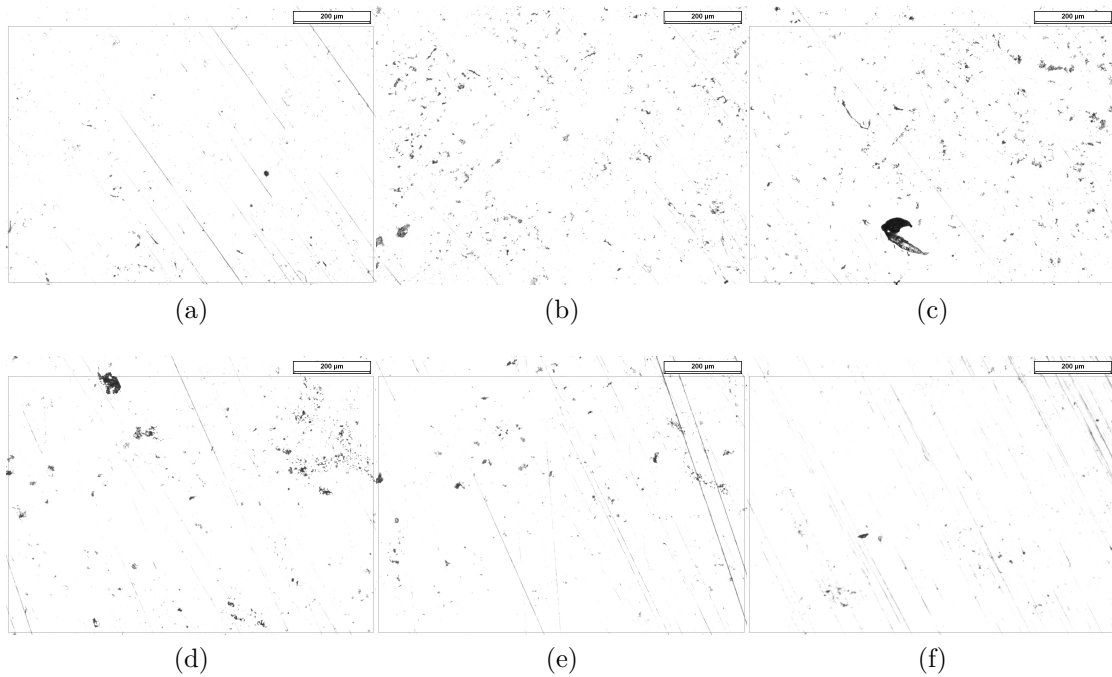


Figure B.9: Optical microscope analysis images for the specimen 1 inclined at  $35^\circ$  in six different points of the downskin region.

Porosity analysis images

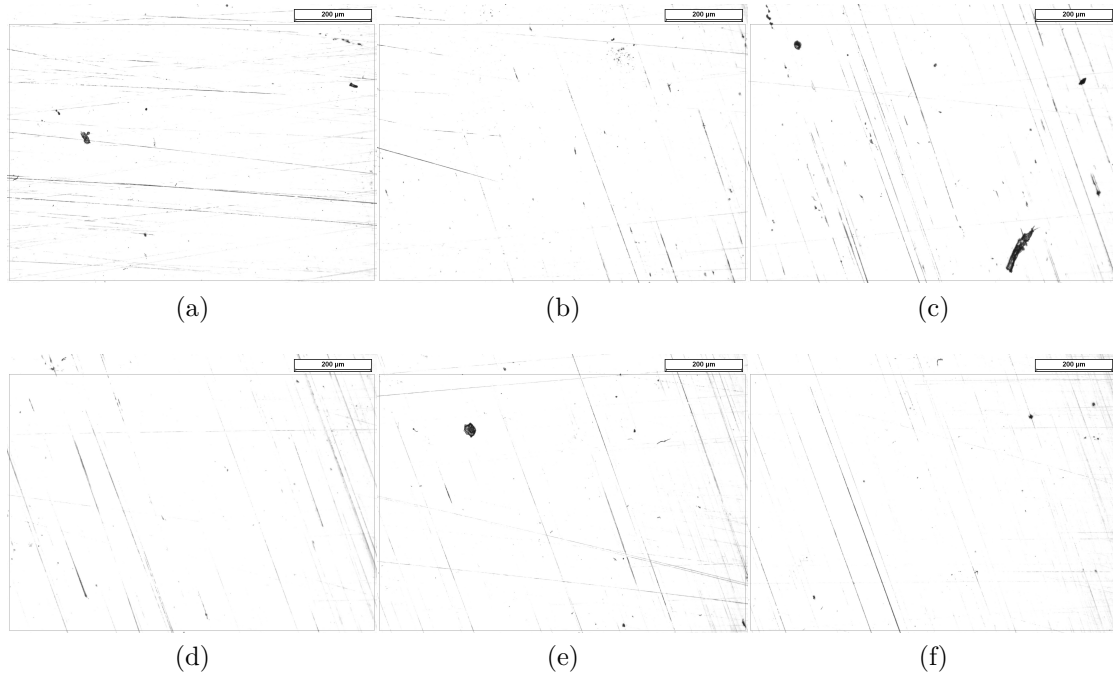


Figure B.10: Optical microscope analysis images for the specimen 2 inclined at  $35^\circ$  in six different points of the downskin region.

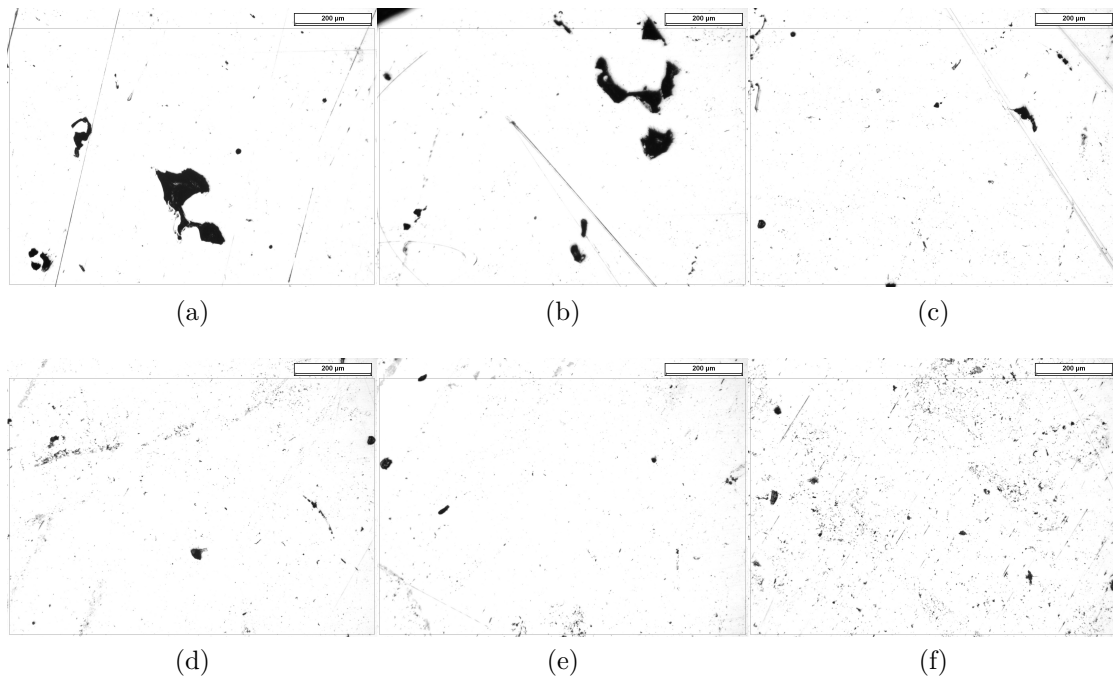


Figure B.11: Optical microscope analysis images for the specimen 4 inclined at  $35^\circ$  in six different points of the downskin region.

Porosity analysis images

---

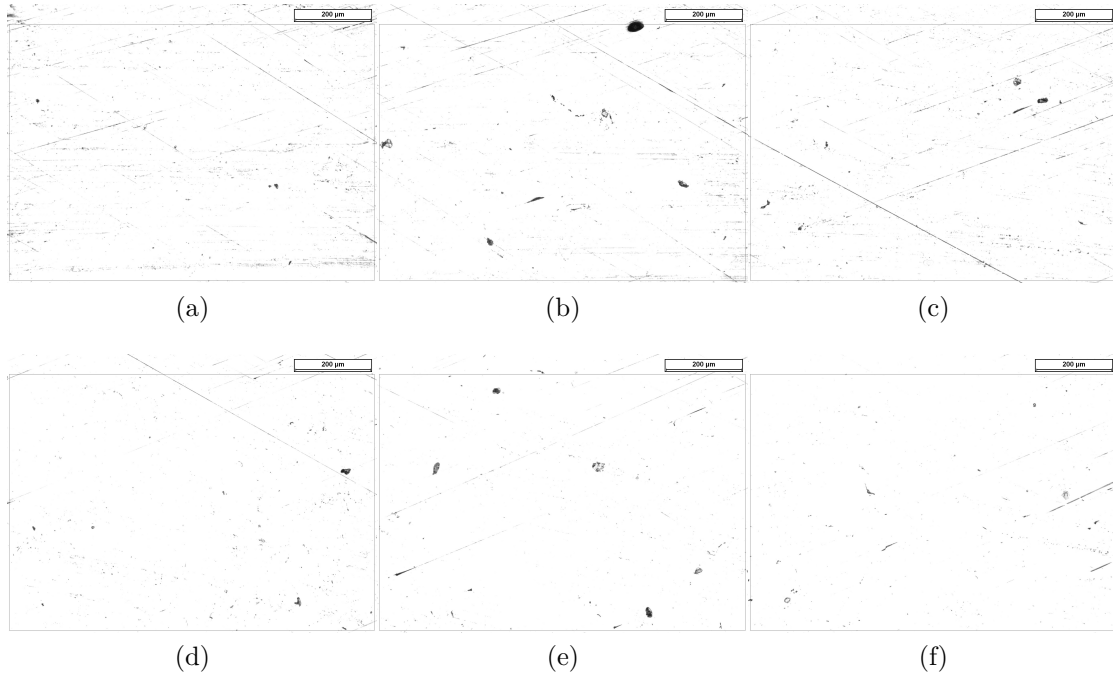


Figure B.12: Optical microscope analysis images for the specimen 6 inclined at  $35^\circ$  in six different points of the downskin region.

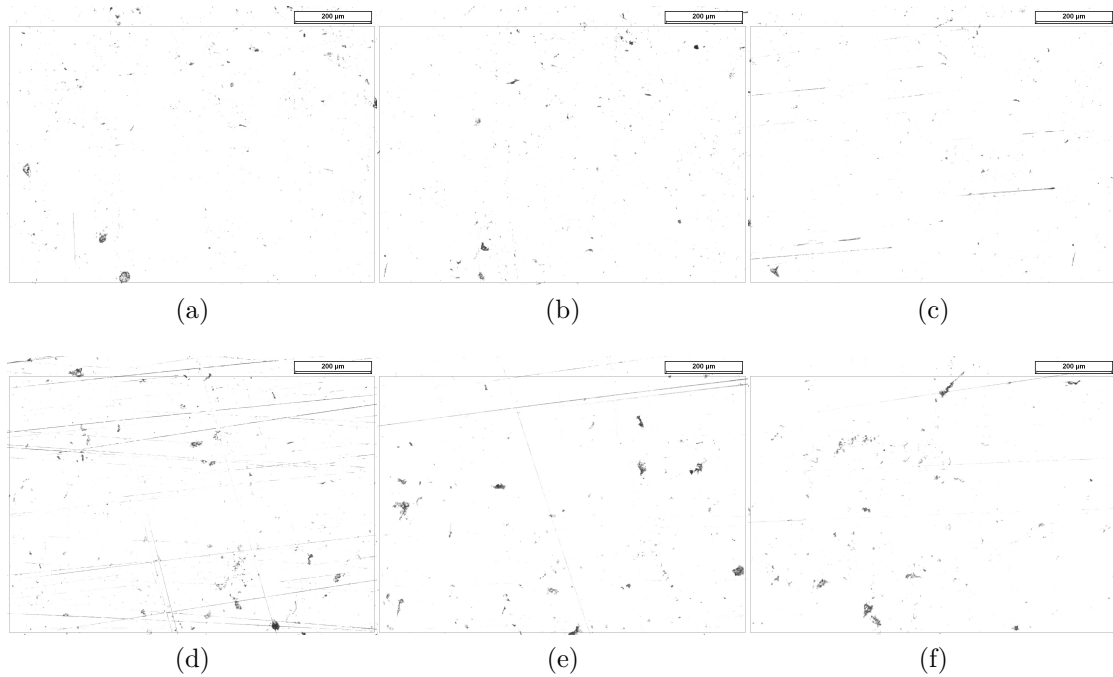


Figure B.13: Optical microscope analysis images for the specimen 11 inclined at  $35^\circ$  in six different points of the downskin region.

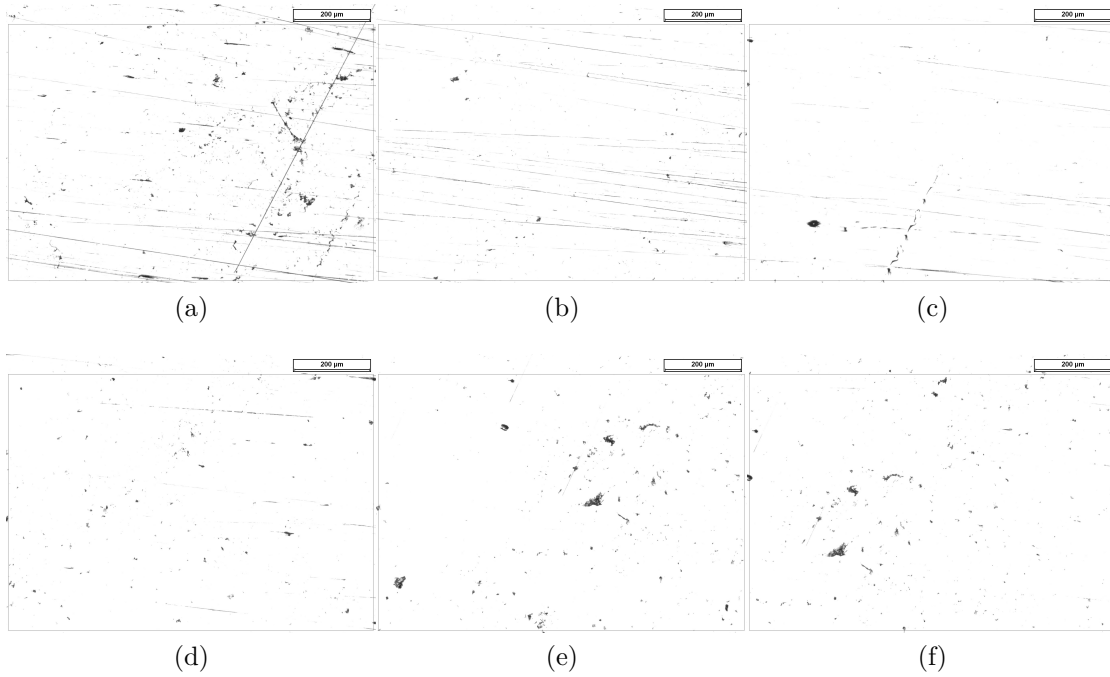


Figure B.14: Optical microscope analysis images for the specimen 12 inclined at  $35^\circ$  in six different points of the downskin region.

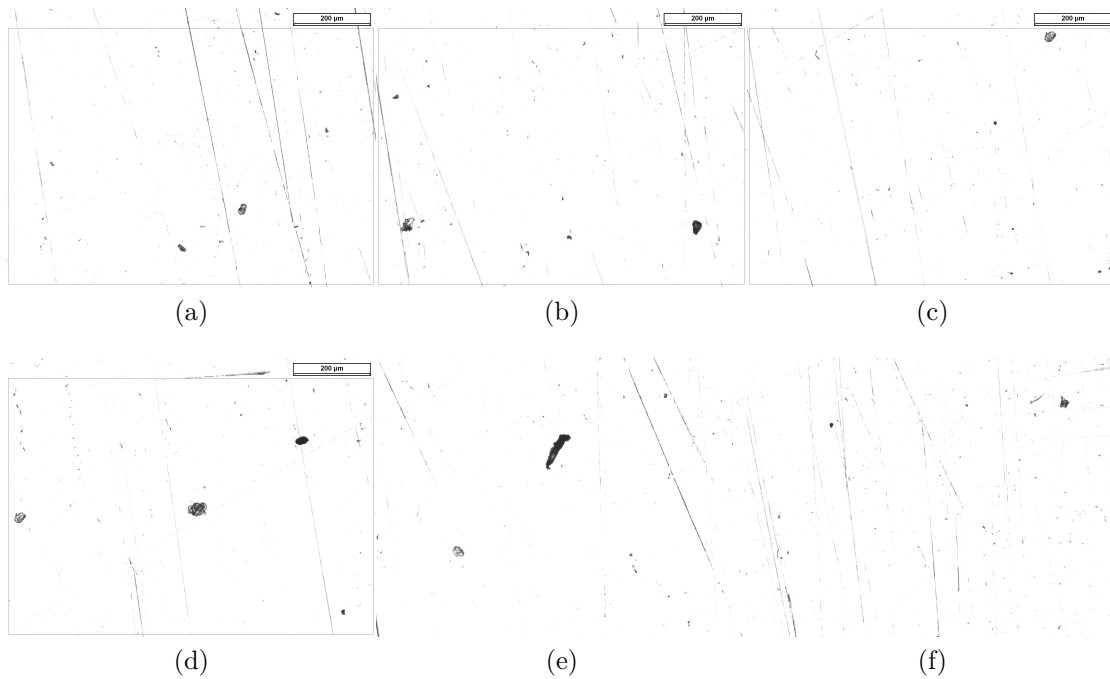


Figure B.15: Optical microscope analysis images for the specimen 15 inclined at  $35^\circ$  in six different points of the downskin region.

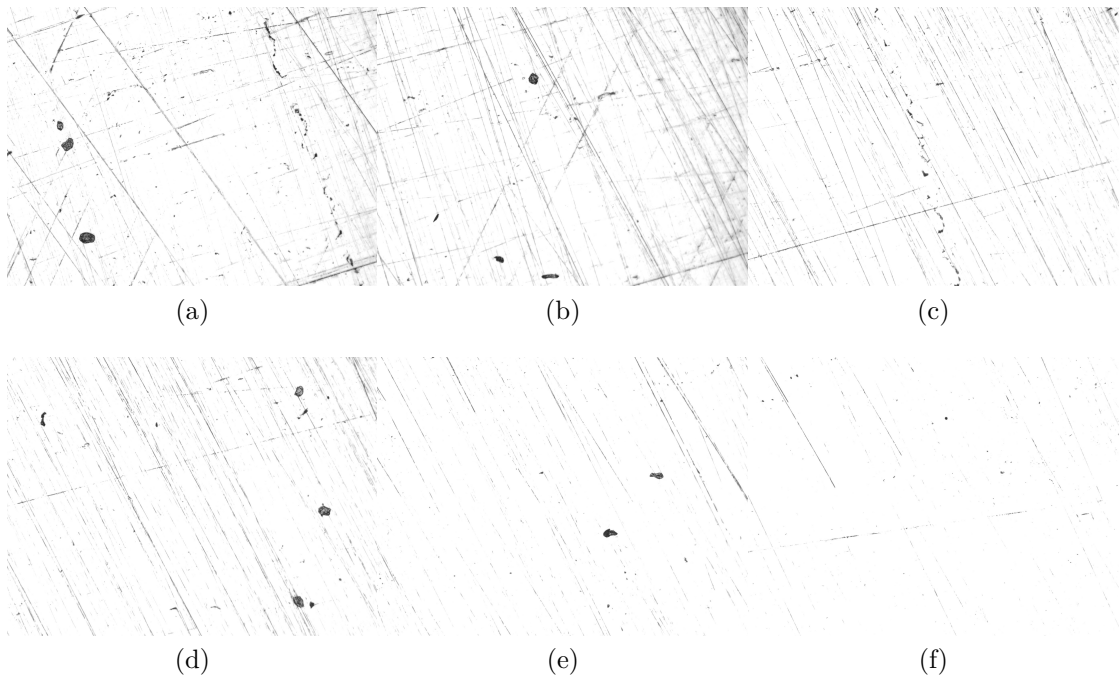


Figure B.16: Optical microscope analysis images for the specimen 20 inclined at  $35^\circ$  in six different points of the downskin region.